Adhesion in Packaging Materials

Pettersson, Simon

2019

Document Version:
Publisher's PDF, also known as Version of record

Department of Construction Sciences
Solid Mechanics

ISRN LUTFD2/TFHF-1061/2019-SE(1-100)

Adhesion in Packaging Materials

Licentiate Dissertation by

Simon Pettersson

Printed by Media-Tryck AB, Lund, Sweden
For information, address:
Division of Solid Mechanics, Lund University, Box 118, SE-221 00 Lund, Sweden
Webpage: www.solid.lth.se

Preface

This licentiate thesis is the result of my work as a PhD student at the division of Solid Mechanics from January 2017 to May 2019. The work has been funded by and carried out in collaboration with Tetra Pak. I would like to thank my main supervisor, Assoc. Prof. Håkan Hallberg for his enthusiasm and patient guidance throughout the project. I would also like to thank my co-supervisors, Assoc. Prof. Stephen Hall and Dr. Jonas Engqvist, for their help, as well as Prof. Mathias Wallin who sparked my interest in the area of solid mechanics in the first place. I would also like to thank my colleagues for interesting conversations and my friends for helping me unwind outside of work.

The people at Tetra Pak who have facilitated this project and made it possible, in particular my industry supervisor Nils Toft, deserve thanks.

Finally, I want to thank my family for their love and support.

Lund, May 2019

Simon Pettersson

Abstract

Modern packaging materials are composed of several material layers, each with a different function. A package needs to fulfill multiple criteria such as structural integrity and sealing to prevent leakage or degradation of the package content. For the layers to fulfill their respective roles in this regard, it is required that they adhere well to each other. However, during handling, manufacturing and transport processes can sometimes cause delamination between the layers. On the other hand, controlled delamination is a prerequisite for other aspects of package functionality, for example in various opening mechanisms. Regardless of whether the aim is to avoid or facilitate delamination, interlaminate adhesion and delamination properties must be a controllable and verifiable package property.

There are several methods to characterize adhesive strength in relation to delamination. One of the most common is the peel test, in which a layer is peeled off from a substrate and the force required to do this is measured. From the peel force, the energy associated with the adhesive fracture can be calculated. The deformation of the peel arm also contributes to the measured peel force, as considered in classical analytical models of peel testing, such as the Kendall and Kinloch models for linear elastic and elastic-plastic deformation of the peel arm, respectively.

In this work, a 90° peel test rig has been developed to permit performing *in-situ* peel testing with imaging by X-ray tomography. Using X-rays for *in-situ* peel testing is a novel concept, allowing more information to be obtained than with a traditional peel test, where only the macroscopic force and displacement are measured or *in-situ* peel tests where the imaging relies on traditional high-speed cameras or scanning electron microscopy. In addition to establishing the new *in-situ* peel testing methods, and developing the required experimental hardware, different failure mechanisms and inhomogeneous delamination patterns are identified from the X-ray images. The experimental results are further analyzed by confronting them with numerical simulations based on a cohesive zone approach as well as with classical models of peel testing. The potential to use Digital Volume Correlation to obtain the full-field deformation of the peel arm is also explored as a possible further elaboration of *in-situ* peel testing using X-ray tomography.

Contents

1 Background

Packaging materials is a billion-dollar industry. The safe transport of food and dairy products from production to shelf is dependent on reliable packages which keep their structural integrity in every part of the chain, from manufacturing to filling and transport. Packaging materials for the food and dairy industries are often composed of several layers, with different functions, forming a laminate material. For example, paperboard is typically used to provide stiffness, while aluminum foil acts as a light and oxygen barrier and a polymer, such as polyethylene, provides a barrier between the paperboard and the content. To provide maximum shelf life, it is crucial that the adhesion between the layers is sufficient, otherwise the product can be degraded, reducing its shelf life considerably. Other requirements are package opening mechanisms that maintain their sealing properties until the seal is intentionally broken.

The peel test is one of the most common ways to study adhesion and many different peel test variants have been developed over the years, some of which have been standardized in regulatory norms. Ideally, when peeling a film layer off a substrate, the work of separation is a measure of the adhesion energy [75]. However, due to deformation of the layer being peeled off, called the peel arm, the supplied energy is often orders of magnitude greater than the adhesion energy. The effect of elastic and plastic deformation during peeling has been studied extensively, for example in [29, 48, 49], deriving expressions for, e.g., the fracture energy and mode mixity. Cohesive zones are another popular way to model decohesion phenomena and some of the developments in cohesive zone modelling are summarized in this work. Additional insight into the decohesion mechanisms can be gained by combining the peel test with imaging methods such as scanning electron microscopy and X-ray tomography.

2 Theories of adhesion

There are a number of different theories on how adhesion is built up and degraded. The existence of an adhesive force holding bodies together was identified already by Aristotle. The adhesion phenomena was also considered by Isaac Newton. Although Newton could not perform any of the experiments known today, he grouped the theory of adhesion into two categories: *fundamental* and *practical* adhesion. Fundamental adhesion is concerned with the study of what makes two surfaces stick, while practical adhesion is concerned with the study of what is required to separate them. Hence, some of the theories of adhesion, like "the weak boundary layer theory", are more concerned with practical questions of where the decohesion will occur during failure, while others, like the "adsorption theory", attempt to explain how and why surfaces in contact bond in the first place, based on thermodynamic considerations. Both the weak boundary layer theory and the adsorption theory are thoroughly discussed in, e.g., [21] and [72]. Actual research into adhesion phenomena is considered to have started in the 1920s with McBain and Hopkins [55] and

some different theories on the subject during the middle of the 20th century. The view of the scientific community on adhesion theories seems to have shifted from a more exclusive view originally, to a more complementary view in recent years. In other words, the first proponents of the theories often had an antagonistic view of other theories and researchers were intent on finding a "master theory", explaining fully the phenomena of adhesion and decohesion. Today, different theories are more often seen as emphasizing different aspects of adhesion, rather than being mutually exclusive.

2.1 Mechanical interlocking

One of the first theories, trying to explain adhesion, is that of mechanical interlocking, first proposed by McBain and Hopkins in 1925 [55]. According to this theory, adhesion is formed due to surface roughness and cavities. With good wetting, an adhesive is able to fill the surface cavities creating an interlocking bond between the two surfaces. The mechanical interlocking theory is contradicted by the fact that smooth surfaces can also form adhesive bonds, but attempts have been made to reconcile these facts by considering adhesion to be governed by both mechanical interlocking and thermodynamic interfacial interactions [34]. Based on this, Wake [100] suggested that the strength G of the adhesive bond can be partitioned as

$$\begin{aligned} G = {} & \text{constant} \times (\text{mechanical interlocking component}) \\ & \times (\text{interfacial interaction component}) \end{aligned} \tag{1}$$

By this multiplicative split of the contributing factors, it should be possible to reach a high level of adhesion by improving both the surface morphology and the physical and chemical surface properties of the bonded surfaces and the adhesive. However, in most cases, mechanical interlocking can be thought to simply improve the adhesion by the fact that the interfacial area increases due to surface roughness. Some authors have also suggested that a rough surface increases bond strength not through interlocking, but by enabling higher viscoelastic and plastic dissipation [3, 40, 102].

2.2 Electronic theory

According to the electronic theory of adhesion, an electron transfer mechanism between substrate and adhesive, having different electronic band structures, can occur to equalize Fermi levels [72]. This could induce the formation of a double electrical layer at the interface. Deryaguin et al. proposed that the resulting electrostatic forces can give a significant contribution to the adhesion [23–25]. Hence, the junction between adhesive and substrate can be modeled as a capacitor. During interfacial failure of this system, separation of the two plates of the capacitor leads to an increasing potential difference until a discharge occurs. Therefore, it is considered that adhesion is a result of the attractive electrostatic forces across the electrical double layer. The energy of separation of the interface, G_e, is therefore related to the discharge potential V_e by:

$$G_e = \frac{h\varepsilon_d}{8\pi}\left(\frac{\partial V_e}{\partial h}\right)^2 \tag{2}$$

where h is the discharge distance and ε_d the dielectric constant. Moreover, according to such an approach, adhesion could vary with the pressure of the gas in which measurement is performed. However, there is no clear correlation between electronic interfacial parameters and the work of adhesion and the energy dissipated viscoelastically or plastically is not considered in this theory. In peeling experiments on vacuum-deposited metallic films on borosilicate substrates, von Harrach and Chapman found that the electrostatic adhesion energy amounted to a maximum of 20% of the van der Waals adhesion energy, which in turn was found to always be smaller than the total work of separation [98]. The electronic theory of adhesion has also received considerable criticism, for example by Huntsberger [43] and Gardon [33].

2.3 Weak boundary layer theory

The adhesion theory of weak boundary layers states that material near the interface will have different properties than the bulk materials due to the presence of the opposing surface. The zones for which this is true are in this view on adhesion denoted boundary layers. According to the weak boundary layer theory, only cohesive failure, occuring in the weakest of these boundary layers, should be possible and no purely interfacial failure will take place, motivated by a statistical reasoning. Much of the early work, in which the weak boundary layer theory is exploited, was done by Bikerman and colleagues in the 1950s and 1960s, who frequently observed cohesive failure close to the interface and who could show the existence of a weak boundary layer in certain cases, e.g. [12]. Bikerman's position was that weak boundary layers are widespread, that interfacial failure is impossible and that the practical strength of an adhesive bond depends on the rheology, not on interfacial forces [12]. This view is not supported in recent literature, but its effect in stimulating discusssion and research is recognized. It is acknowledged that at the time, the recognition of the importance of the rheology of bonds was an important contribution, while the neglection of interfacial forces was not justified. Another key concept is the locus of failure, stating that when weak boundary layers are important, failure typically occurs within this weak layer, close to, but not at, the interface between the adhesive and substrate. This layer can be very thin, giving the impression that the failure is adhesive when in fact it is cohesive. This insistence that interfacial can not occur has, according to recent reference literature, led to more detailed studies of the failure locus of the locus of failure, employing modern surface analysis, although it is still sometimes neglected. Such studies have, however, shown that pure interfacial failure is rare, but does occur [21]. A criticism of the theory is that cohesive failure close to the interface does not prove the presence of a weak boundary layer. It was shown already in 1972 that cohesive failure close to an interface is possible without introducing a weak boundary layer [36]. More recently, Chen *et al.* demonstratedy that the failure locus depends on the mode mixity of the loading and hence the crack does not propagate universally along the weakest boundary layer, as the weak boundary layer theory predicts [17].

2.4 Adsorption theory

The most widely used adhesion theory is the adsorption or thermodynamic theory, attributed to Sharpe and Schonhorn[80]. This theory is based on the idea that adhesion is due to interatomic and intermolecular forces at the interface. The magnitude of these forces can generally be related to thermodynamic quantities, such as the surface free energies of adhesive and adherend. Wetting criteria as well as surface and interface free energies can be defined, according to the adsorption theory. The reversible work of adhesion W can then be estimated. Next, the relation between measured adhesion strength G to the free energy of adhesion W can be modeled in various ways.

Most adhesive bonds are formed when a liquid adhesive comes into contact with a solid substrate. Therefore, the degree of wetting and other factors that can affect this solid-liquid interface are of importance. A significant body of theories on the thermodynamics of spreading and wetting has been developed, which can be used to relate surface energies and surface tensions to contact angles and to the extent of wetting. If the surface energy or the contact angle is known, the adhesion strength can be calculated and predicted [21].

The idea of adhesion between bodies being due to interatomic and intermolecular forces established at the interface is given. Experimental substantiation of this is given by Leadley and Watts, who used X-ray photoelectron spectroscopy to identify several distinct acid-base interactions at the interface between a polymer and a metal oxide [50].

One of the main models mapping the reversible work of adhesion to the measured adhesion strength is the rheological model, or the model of multiplying factors, proposed by Gent and Schultz [34]. This theory states that the measured peel strength is the product of the reversible work and a loss function $\Phi = \Phi(v, T)$ which depends on the peel rate v and the temperature T, providing

$$G = W\Phi(v, T) \tag{3}$$

The loss function corresponds to the energy dissipated viscoelastically or plastically. Usually, the loss function is much greater than the reversible work of adhesion.

2.5 Diffusion theory

The diffusion theory originated with S. S. Voyutskii and coworkers in the middle of the 20th century, as discussed by da Silva *et al.* in [21]. The original work was mainly on self-adhesion of elastomers and was later extended to polymer adhesion. Effects of parameters such as time, temperature, contact pressure and molecular weight were studied. It was argued that adhesion is associated with the interdiffusion of molecular polymer chains. Even though the work was concerned with polymer-polymer adhesion, Voyutskii argued its applicability also to polymer-metal adhesion .

A thermodynamic criterion for the compatibility of polymers is that the Gibbs free energy of mixing ΔG_m is negative. If this is the case, spontaneous mixing will occur. The change in Gibbs free energy is given by

$$\Delta G_m = \Delta H_m - T\Delta S_m \tag{4}$$

where ΔH_m is the change in enthalpy, T is the temperature and ΔS_m is the change in entropy. The second term is always negative since mixing will increase entropy. However, for polymers, the entropy change is small due to the long molecular chains with limited ability to change conformation, compared to small molecules. Polymers as similar as polypropylene and polyethylene are incompatible. It has been found that most polymers are incompatible, which points to the limited applicability of the theory, except for self-adhesion.

Thanks to molecular dynamics, detailed descriptions of polymer chain motion can be given, as shown by Wool [105, 106]. The relaxation behavior of polymers has thus been related to five mechanisms: short-range Fickian diffusion of single chain segments, Rouse relaxation between chain entanglements, Rouse relaxation of the entire chain, reptation motion and Fickian long-range diffusion. These are given in increasing order of timescales, with short-range Fickian diffusion being the fastest and long-range Fickian diffusion being the slowest. The reptation region is the main contributor to interfacial strength [107].

3 Classical approaches to peel test modeling

The peel test is a standard method to evaluate adhesion properties. In a peel test, a peel arm is peeled off from a substrate at an angle θ as shown in Fig. 1. The angle is between 0 and 180°. If the test is done at 0 or 180°, tensile test grips are usually used, while for 90°, a "German wheel" can be used to keep the peel arm at right angle to the substrate. Such a wheel is free to rotate, keeping the angle at (ideally) 90° as the delamination propagates.

3.1 Fracture energy

An energy balance of this system was done by Rivlin [75], assuming a rigid peel arm. If that is the case, it can be shown that the fracture energy required to separate the surfaces is

$$G_c^{Rivlin} = \frac{F}{b}(1 - \cos\theta) \tag{5}$$

where b is the width of the sample (in the out-of-plane direction of Fig. 1).

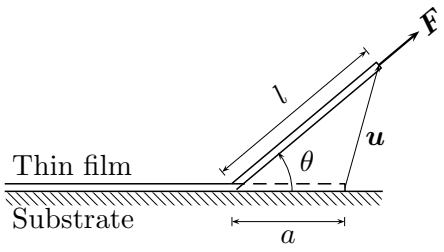

Figure 1: Schematic illustration of peeling of a thin film from a rigid substrate. The film, of width b and thickness $h \ll b$, is peeled of by a force (vector) $\boldsymbol{F}$ at an angle θ from the substrate, which is assumed to be rigid. The displacement of the end of the peel arm is denoted by the vector $\boldsymbol{u}$. The length of the adhesive fracture zone and the length of the stretched peel arm is denoted by a and l, respectively.

However, more recent studies recognize that, in general, the peel arm can not be regarded as rigid. In particular, Kendall [48] extended the energy balance analysis to account for linear elasticity and small strains in the peel arm. This approach provides the fracture energy

$$G_c^{Kendall} = \frac{1}{2}\frac{F^2}{Eb^2h} + \frac{F}{b}(1-\cos\theta) \tag{6}$$

which is greater than the Rivlin fracture energy. Further analyses were provided by Kinloch, e.g. [49], who assumed the peel arm material to be elasto-plastic with bilinear hardening. A general expression for fracture energy by Kinloch's approach is provided by

$$G_c = \frac{1}{b}\left(\frac{dU_{ext}}{da} - \frac{dU_s}{da} - \frac{dU_{dt}}{da} - \frac{dU_{db}}{da}\right) \tag{7}$$

where dU_{ext} is the external work, dU_s the stored (recoverable) strain energy in the peel arm, dU_{dt} the energy dissipated during tensile deformation of the peel arm, and dU_{db} the energy dissipated during bending of the peel arm. Kinloch recognized that during initiation of the peel test, there is first a bending of the peel arm to obtain the angle θ. As the peel test then progresses, however, there is local reverse bending and straightening of the peel arm near the crack front. The dissipation during bending and straightening is what causes the most complications in the calculations. If the bending and straightening are both elastic, then $G_{db} = \frac{1}{b}\frac{dU_{db}}{da} = 0$ and

$$\frac{G_a^{\infty E}}{G_{max}^e} = \frac{1-\cos\theta}{[1-\cos(\theta-\theta_0)]}\cdot\frac{k_0^2}{3} \tag{8}$$

where $G_a^{\infty E}$ is the fracture energy for an infinitely stiff peel arm in tension with zero bending stiffness, G_{max}^e the maximum elastic strain energy, θ_0 the root rotation angle at the peel front and $k_0 = \frac{R_1}{R_0}$ is the ratio of the radius of curvature at the onset of plastic deformation $R_1 = \frac{h}{2\epsilon_y}$ to the radius of curvature at the peel front R_0 . This case arises when $0 < k_0 < 1$. If the initial bending is plastic, but the unloading elastic, Kinloch states that

$$\frac{G_{db}}{G_{max}^e} = (1-\alpha)\left\{\frac{k_0^2}{3} + \frac{2(1-\alpha)^2}{3k_0} - 1\right\} \tag{9}$$

and

$$\frac{G_a^{\infty E}}{G_{max}^e} = \frac{1-\cos\theta}{[1-\cos(\theta-\theta_0)]}\cdot\frac{k_0^2}{3} \tag{10}$$

where $\alpha \in [0,1]$ is the slope related to the bilinear hardening plasticity model. In other words, the dissipated bending energy changes to non-zero, but not the ratio $\frac{G_a^{\infty E}}{G_{max}^e}$. It can

be noted that $\alpha = 1$ corresponds to linear elasticity. This case is found when $1 < k_0 < 2(1-\alpha)/(1-2\alpha)$ or $\alpha \geq 0.5$. A third possibility is plastic bending and unloading, in which case

$$\frac{G_{db}}{G^e_{max}} = f_1(k_0) \tag{11}$$

and

$$\frac{G^{\infty E}_a}{G^e_{max}} = \frac{1-\cos\theta}{[1-\cos(\theta-\theta_0)]} \cdot f_2(k_0) \tag{12}$$

where f_1 and f_2 are functions of k_0 involving α. This case arises when $k_0 > 2(1-\alpha)/(1-2\alpha)$ and $\alpha < 0.5$. It is interesting to note that the loading and unloading case can be predicted purely from the slope α.

Following the arguments by Kinloch in [49], it can in passing be noted that a mixed mode analysis for $0 < \theta < 90^\circ$ is usually not called for and consideration of only mode I loading usually suffices. This is also the viewpoint adopted in several later studies on peeling of thin polymer films, for example in [62].

Relations between the fracture energy, the peel force and the peel angle for general elastic models of the peel arm and with a pre-strain in the peel arm prior to peeling were derived by Williams and Kauzlarich [104]. If the peel arm is assumed to be pre-strained by a strain ε_1 corresponding to a force F, then for the case of linear elasticity, it is shown in [54, 103] that

$$G_c = \frac{P}{b}(1-\cos\theta) + \frac{(P-F)^2}{2b^2Eh} \tag{13}$$

and if the peel force P in the tape is given by a general constitutive law

$$P = f(\varepsilon) \tag{14}$$

it is shown in [104] that the expression for the strain ε_2 in the peel arm becomes

$$(1-\varepsilon_1)(1+\varepsilon_2)f(\varepsilon_2) - \cos\theta f(\varepsilon_2) - \int_{\varepsilon_1}^{\varepsilon_2} f(\varepsilon)d\varepsilon = bG_c \tag{15}$$

where ε_2 is the strain associated with the steady peel force P, i.e. $P = f(\varepsilon_2)$. Eq. (15) was used with two constitutive laws, the first being

$$P = B\varepsilon^n \quad \text{and} \quad n < 1 \tag{16}$$

and the second being

$$F = A\frac{\varepsilon}{c+\varepsilon} \tag{17}$$

where A, B and C are material constants. Inserting eq. (16) into eq. (15) yields

$$\left(\frac{P}{B}\right)^{\frac{n+1}{n}} + P' \left(\frac{P}{B}\right) = q \tag{18}$$

where

$$P' = \frac{1 - \varepsilon_1 - \cos\theta}{1 - \varepsilon_1 - \frac{1}{n+1}} \tag{19}$$

and

$$q = \frac{\frac{G_c b}{B} - \frac{\varepsilon_1}{n} + 1}{1 - \varepsilon_1 - \frac{1}{n+1}} \tag{20}$$

Using the second constitutive law, described by eq. (17), it is shown in [104] that the relation

$$\begin{aligned} &\frac{(1-c)\left[A - (1-c)P\right]}{A-P} + c\frac{A}{P}\ln\left\{\frac{A-F}{A-P}\right\} \\ &+ \frac{A-P}{A-F}\frac{F}{P}\left[c - \left(\frac{Pc}{A-P}\right)^2\right] - \cos\theta = \frac{G_c}{P/b} \end{aligned} \tag{21}$$

between the fracture energy G_c, the peel force P, the pre-tension F and the peel angle θ holds. In the special case $c = 1$,

$$\frac{A}{P}\ln\left\{\frac{A-F}{A-P}\right\} + \frac{A}{A-F}\frac{F}{P}\frac{A-2P}{A-P} - \cos\theta = \frac{G_c}{P/b} \tag{22}$$

holds. Moreover, if there is no pre-tension, the expression is further reduced to

$$A\ln\left\{\frac{A}{A-P}\right\} - P\cos\theta = \frac{G_c}{b} \tag{23}$$

and for both constitutive models it is stated in [104] that for small strains the relations degenerate to eq. (6) or eq. (13), depending on the value of F.

A different possibility is to model the peel arm as hyperelastic, isotropic and incompressible in a finite strain setting. To identify the adhesive fracture energy release rate G_c, an energy balance can be established as

$$G_c\, b\dot{a} = \dot{W} - \dot{U} - \dot{\mathcal{D}} \tag{24}$$

where W is the external work done by the peel force $\boldsymbol{F}$ with magnitude F, U is the strain energy stored in the peel arm and $\mathcal{D} \geq 0$ is the energy dissipation. A superposed dot

denotes differentiation with respect to time. The external work power can be evaluated from the vector product between the peel force and the rate of displacement to provides

$$\dot{W} = \boldsymbol{F} \cdot \dot{\boldsymbol{u}} = F\left(\dot{l} - \dot{a}\cos\theta\right) \tag{25}$$

where l is the length of the peeled-off strip and θ the peel angle. Combining eqs. (24) and (25) yields

$$\dot{U} + G_c\, b\dot{a} = F\left(\dot{l} - \dot{a}\cos\theta\right) - \dot{\mathcal{D}} \tag{26}$$

Next, a finite strain setting is assumed and the polymer film constituting the peel arm is in the present case modeled using a constitutive model that assumes an isotropic, hyperelastic and incompressible material behavior, as discussed in [29]. Under uniaxial tensile loading of the film, the stretch ratio $\lambda = l/a$ can be identified and the elastic strain energy density can, quite generally, be expressed as $\tilde{U} = \tilde{U}(I_1, I_2)$, in terms of $I_1 = \lambda^2 + 2\lambda^{-1}$ and $I_2 = 2\lambda + \lambda^{-2}$, being the first and second invariants of the left Cauchy-Green strain tensor. At this stage, the elastic strain energy can be evaluated as

$$U = bh\int_0^a \tilde{U}(\lambda)ds \tag{27}$$

This strain energy can now be inserted into the energy balance in eq. (26) to provide

$$abh\frac{d\tilde{U}}{d\lambda}\dot{\lambda} + bh\tilde{U}\dot{a} + G_c\, b\dot{a} = F\left(\dot{l} - \dot{a}\cos\theta\right) - \dot{\mathcal{D}} \tag{28}$$

With $\lambda = l/a$, eq. (28) can be further recast into

$$bh\frac{d\tilde{U}}{d\lambda}\dot{l} - bh\frac{d\tilde{U}}{d\lambda}\lambda\dot{a} + bh\tilde{U}\dot{a} + G_c\, b\dot{a} = F\left(\dot{l} - \dot{a}\cos\theta\right) - \dot{\mathcal{D}} \tag{29}$$

Noting that the nominal uniaxial stress in the peel arm is provided by

$$\sigma(\lambda) = \frac{d\tilde{U}}{d\lambda} = \frac{F}{bh} \tag{30}$$

the energy balance in eq. (29) can be stated as

$$\left[bh\tilde{U} + F\left(\cos\theta - \lambda\right) + G_c\, b\right]\dot{a} = -\dot{\mathcal{D}} \leq 0 \tag{31}$$

For $\dot{a} \geq 0$, a positive dissipation is ensured by

$$G_c = \frac{F}{b}(\lambda - \cos\theta) - h\tilde{U}(\lambda) \tag{32}$$

It can be noted that the Rivlin and Kendall models can be obtained as special cases of this model. If the stretch $\lambda = 1$ during the loading, then the elastic strain energy $\tilde{U} = 0$, which corresponds to the situation of a rigid peel arm material. It can then be seen that eq. (32) collapses to the Rivlin model in eq. (5). Assuming instead small strains, such that $\varepsilon \ll 1$, then $\lambda = 1 + \varepsilon$ and the elastic strain energy becomes

$$\tilde{U} = \frac{1}{2}\sigma\varepsilon = \frac{1}{2}\frac{F^2}{E(bh)^2} \tag{33}$$

where E is the elastic Young's modulus of the peel arm material. Inserting eq. (33) into eq. (32) yields

$$G_c = \frac{1}{2}\frac{F^2}{Eb^2h} + \frac{F}{b}(1 - \cos\theta) \tag{34}$$

which is the Kendall fracture energy, cf. eq. (6). Thus, the Rivlin and Kendall models are obtained as special cases of this general model. As shown in [29], the different models of the adhesive fracture energy release rate are related as

$$G_c^{Rivlin} \leq G_c^{Kendall} \leq G_c \tag{35}$$

According to eq. (35), the Rivlin model can be expected to provide a lower-bound estimate of the adhesive energy release rate.

It can be noted that the energy balance provided by eq. (24) corresponds to the one used by Kinloch *et al.* in [49], with the dissipation $\mathcal{D}$ containing contributions from plastic bending close to the peel front. It is, however, shown in the peel experiments on thin low-density polyethylene (LDPE) films conducted in [62], that the energy dissipated in the bending deformation is two orders of magnitude smaller than the peel energy, also for an extreme peel angle of $\theta = 180°$. A similar conclusion is arrived at in [59] where the combined plastic dissipation from bending and stretching of the peel arm is calculated to be about one order of magnitude lower than the fracture energy. The conclusion drawn in [62] is that the energy dissipation due to bending during peeling of a thin polymer film can be neglected. The same viewpoint is adopted also in the present work and the plastic dissipation will not be distinguished as a separate component.

3.2 Phase angle

Thouless and Yang [87] presented an improved expression for the phase angle in the peel test, based on the criterion by Thouless and Jensen in 1992 [86] but taking into account shear at the crack tip. The phase angle indicates the degree of mode mixity. The dimensionless constants α and β, indicating elastic modulus mismatch, were introduced as [87]

$$\alpha = \frac{\bar{E} - \bar{E}_s}{\bar{E} + \bar{E}_s},$$
$$\beta = \frac{\bar{E}g(\nu_s) - \bar{E}g(\nu)}{\bar{E} + \bar{E}_s} \tag{36}$$

where $\bar{E}$ is the effective Young's modulus for the peel arm, with $\bar{E} = E$ for plane stress and $\bar{E} = \frac{E}{1-\nu^2}$ in plane strain and $\bar{E}_s$ is the corresponding effective modulus of the substrate. Further ν is the Poisson's ratio for the peel arm, ν_s is the Poisson's ratio for the substrate and

$$g(\nu) = \begin{cases} \frac{1-2\nu}{2(1-\nu)} & \text{in plane strain} \\ \frac{1-2\nu}{2} & \text{in plane stress} \end{cases} \tag{37}$$

The peel arm was modeled as a beam, assuming an infinitely thick substrate. The phase angle was chosen in accordance with models given in [70, 109] as

$$\psi = \tan^{-1}\sqrt{\frac{G_{II}}{G_I}} \tag{38}$$

where G_I is the fracture energy in Mode I and G_{II} is the fracture energy in Mode II. If a compressive force N is applied at the crack tip, the fracture energy is given by [87]

$$G_N = \frac{1}{2}\frac{N^2}{\bar{E}h} \tag{39}$$

with a phase angle $\psi_N = \psi_N(\alpha, \beta)$ given in [83]. For $\alpha = \beta = 0$, $\psi_N = 52.1°$. If a bending moment M is applied at the crack tip, the fracture energy is given by [87]

$$G_M = 6\frac{M^2}{\bar{E}h^3} \tag{40}$$

with a phase angle $\psi_M(\alpha, \beta) = -90° + \psi_N(\alpha, \beta)$. The fracture energy for a shear force V applied at the crack tip is given by [87]

$$G_V = 3.764\frac{V^2}{\bar{E}h} \tag{41}$$

where $f_V(\alpha, \beta)$ a function of the elastic mismatch given in [51] for $\beta = 0$ and the phase angle $\psi_V = \psi_V(\alpha, \beta)$. If all three components act at the crack tip, the phase angle and fracture energy are given by [51]

$$\psi = \tan^{-1}\left[\frac{\frac{Nh}{M}\sin\,\psi_N + \sqrt{12}\sin\,\psi_M + \sqrt{2}f_V(\alpha,\beta)\frac{Vh}{M}\,\sin\,\psi_V}{\frac{Nh}{M}\cos\,\psi_N + \sqrt{12}\,\cos\psi_M + \sqrt{2}f_V(\alpha,\beta)\frac{Vh}{M}\cos\,\psi_V}\right] \tag{42}$$

and

$$
\begin{aligned}
G =& \frac{N^2}{\bar{E}h}\left[0.5+\sqrt{2}f_V(\alpha,\beta)\left(\frac{V}{N}\right)\cos(\psi_N-\psi_V)\right] \\
&+\frac{M^2}{\bar{E}h^3}\left[6+f_V^2(\alpha,\beta)\left(\frac{Vh}{M}\right)^2+2\sqrt{6}f_V(\alpha,\beta)\left(\frac{Vh}{M}\right)\cos(\psi_V-\psi_M)\right]
\end{aligned}
\tag{43}
$$

If the three loading components are known, the phase angle can be determined. While analytical expressions exist for the calculation of the phase angle for an axial force and a bending moment, the values of the function $f_V(\alpha,\beta)$ cannot be calculated analytically, but have to be estimated numerically. Thus, including shear forces makes analysis of the peel test significantly more complicated [51].

3.3 Rate effects

A lot of work has been done to investigate the rate dependence of the peel test. Peng *et al.* [71] found that the peeling rate of a viscoelastic thin-film on a rigid substrate had a great influence on the adhesion. An expression for the viscolastic energy release rate was derived, based on theoretical analysis by Chen *et al.* in [18]. For steady state peeling, the energy release rate is found to be

$$
G = \frac{F}{w}\left(1+\varepsilon_{peel}-\cos\theta\right)-\frac{1}{w}\int_0^\infty\left(M\frac{dk}{ds}+T\frac{d\varepsilon_m}{ds}\right)ds \tag{44}
$$

where F is the peel force, $\varepsilon_{peel}=F/(E_\infty wh)$ is the film strain at the end of loading and E_∞ is the long-time relaxation modulus. Furthermore, M is the bending moment and T is the axial force in any cross-section of the film, k is the curvature and ε_m the tensile strain in the film. Eq. (44) can be recast into

$$
G = \frac{F}{w}(1-\cos\theta)+\frac{1}{w}\int_0^\infty k\frac{dM}{ds}ds+\frac{1}{w}\int_0^\infty \varepsilon_m\frac{dT}{ds}ds \tag{45}
$$

For small peeling strains, $F/(E_0wh) << 1$, the viscoelastic energy release rate can be approximated as

$$
G \approx \frac{F}{w}(1-\cos\theta) \tag{46}
$$

which has a format similar to the classical Rivlin formula. However, in the viscoelastic case, F is rate-dependent. Peng *et al.*, as well as other experimenters [10, 27, 52, 112] have found that the dependence on peeling rate can be written approximately as

$$
\frac{F}{w} = C_0(1+kv^n) \tag{47}
$$

which can be substituted into eq. (46) to provide

$$G = C_0(1 - \cos\theta)\left(1 + \left(\frac{v}{k_0}\right)^n\right) \tag{48}$$

where $k_0 = \frac{1}{\sqrt[n]{k}}$, C_0 and k are related to the peeling angle and film thickness and n is a constant to be determined. The effect of rate is also studied by Williams and Kauzlarich in [104], where it is first shown that, for a rigid peel arm, there will be a velocity ratio between the peel velocity and the crosshead speed, given by

$$\frac{v}{v_{ch}} = \frac{1}{1 - \cos\theta} \tag{49}$$

where v is the peeling rate and v_{ch} the crosshead speed in the tensile loading stage. If the tape extends, however, the peeling rate is shown in [104] to be

$$v = \frac{v_{ch}}{[(1 - \varepsilon_1)(1 + \varepsilon_2) - \cos\theta]} \tag{50}$$

where ε_1 is the pre-strain and ε_2 the peel strain. A relationship between fracture energy and peeling rate was also found from experiments in [104] as

$$G_c \propto v^z \tag{51}$$

where the exponent z was found to be 0.07 for a synthetic acrylic adhesive tape, indicating a very low rate dependence. For a tape with a rubber based adhesive, z was found to be 0.4 for peel angles $\theta > 60°$ and 0.25 for $\theta = 20°$, at constant temperature conditions. With a silicon adhesive, z was 0.21 for $\theta > 50°$ and 0.12 for $\theta = 20°$ [104]. Thus, the rate dependence also seems to depend on the peel angle, with lower rate dependence for smaller peel angles. It can be noted that Peng *et al.* as well as Williams and Kauzlarich found a power-law dependence of the fracture energy on the peeling rate.

4 Numerical modeling

In this section some background to cohesive zone modeling is provided along with a brief summary of aspects and considerations of importance in relation to such modeling.

4.1 Cohesive zone modeling

A common way of modeling interfacial failure between two bodies is by using cohesive zones. The concept of cohesive zones was originally proposed by Barenblatt [6]. The general idea is to obtain finite stresses in the vicinity of a crack tip, as opposed to the stress singularity that arises in classical fracture mechanics, dating back to Irwin [44]. Ideally, the cohesive zone is rigid unless an activation stress T_0 is applied, after which

there is a gradual softening of the material until complete failure, i.e. zero stiffness. For numerical implementations, a finite initial stiffness K is usually required. This is achieved by relating the activation stress T_0 to an initial separation of the interfaces, δ_0. Some common variants of the resulting traction-separation law are illustrated in Fig. 2. As indicated in the figure, the fracture energy G_{Ic} is obtained by integration of the traction-separation law (the index I indicates mode I fracture).

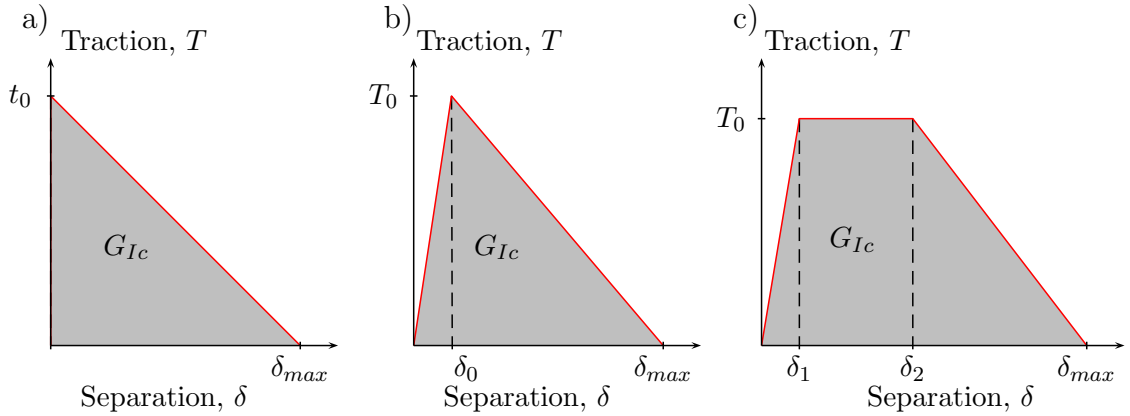

Figure 2: Different traction-separation laws. a) Ideal bilinear b) Bilinear model with finite initial stiffness c) Trapezoidal model.

4.2 Damage initiation criteria

To initiate damage in the cohesive zone, different criteria can be used. The criteria are usually expressed in terms of stress components or separation in the interfacial layer. Different fracture modes may interact or be considered separately. As an example, a damage criterion based on maximum tractions can be formulated as

$$\max\left(\frac{\langle t_n\rangle}{t_0^n}, \frac{t_s}{t_0^s}, \frac{t_t}{t_0^t}\right) = 1 \tag{52}$$

where t_0^n is the maximum normal traction and t_s, t_t are the maximum shear tractions in mode II and III, respectively. The Macaulay brackets around t_n provide $\langle t_n\rangle = (t_n + |t_n|)/2$, thereby avoiding damage initiation from compressive normal loading. The damage criterion in eq. (52) ensures that only the mode with the highest stress activates damage. In contrast, an alternative criterion can be defined as

$$\sqrt{\left(\frac{\langle t_n\rangle}{t_0^n}\right)^2 + \left(\frac{t_s}{t_0^s}\right)^2 + \left(\frac{t_t}{t_0^t}\right)^2} = 1 \tag{53}$$

in which the different modes interact to compound the stress. In the commercial finite element software Abaqus, used for the numerical simulations in the present study, eq. (52) and eq. (53) are implemented as the "maxs" and "quads" damage criterion, respectively. For the 90° peel test considered in the present study, it can be assumed that the delamination progresses as a pure Mode I fracture. Therefore, high threshold values are set for the

shear modes, ensuring that shear deformation does not activate damage. This also causes the criteria in eq. (52) and eq. (53) to be roughly equal, since the shear terms vanish for large threshold stresses.

Once damage is initiated, the interface gradually loses stiffness. This is usually traced by using a damage variable D, $0 \leq D \leq 1$, where $D = 0$ is an undamaged material and $D = 1$ a fully damaged material, that scales the stiffness of the cohesive zone.

4.3 Cohesive zone stiffness

The stiffness K of the cohesive zone needs to be as large as possible to prevent excessive compliance in the interface. For very high values however, numerical problems often arise. Different guidelines to estimate K have been proposed in the literature. For fiber reinforced plastics, the mode I interface stiffness was proposed by Daudeville *et al.* [22] to depend on the out-of-plane ply stiffness E_3 and the interfacial thickness t according to

$$K = \frac{E_3}{t} \tag{54}$$

In [113], Zou *et al.* proposed an interface stiffness of 10^4 to 10^7 times the interfacial strength, also for fiber reinforced plastics. In [89], Turon *et al.* proposed an interface stiffness

$$K = \alpha \frac{E_3}{t} \tag{55}$$

where $\alpha >> 1$ is a numerical factor, proposed to be around 50 by the authors. This will give a loss of stiffness near the interface of less than 2 %. One issue with all of the above models is that they assume orthotropic elasticity of the bulk material, which is not the case here. For a nonlinear material, it is not clear what E_3 corresponds to. If the peel arm is undeformed or at small strain, the initial stiffness might be appropriate, but for finite deformation a different and ideally dynamic stiffness appears as the candidate.

Yuan and Li [110] used a trapezoidal cohesive zone law with a J_2 plasticity model for the bulk material, with Ramberg-Osgood hardening. In their model, the specific cohesive zone stiffness was expressed as

$$K = \frac{T_{max}}{\delta_1} \xi \tag{56}$$

where T_{max} is the maximum traction and δ_1 the separation at which the maximum traction is first reached, cf. Fig. 2c. The parameter ξ is the characteristic length of the cohesive zone. Yuan and Li found the effect of cohesive zone stiffness on force versus displacement to be negligible, while the prediction of the crack length Δa varied as much as 35 % depending on the value of the initial cohesive stiffness K.

4.4 Cohesive zone length

Cohesive zones introduce a length scale into the model. The cohesive zone length l_{cz} is defined as the distance from the crack tip to the point at which the material has retained its full stiffness. The material in between has softened but not yet failed. There is no consensus on how to determine this length scale, but in general it can be estimated from

$$l_{cz} = ME\frac{G_c}{T_0^2} \tag{57}$$

where M is a parameter that depends on the particular material and application and where E is the Young's modulus of the bulk material, G_c the fracture energy and T_0 the peak stress. In general, M is chosen in the interval between 0.21 and 1. Hui *et al.* [42] used $M = 0.21$ for soft elastic solids, Irwin proposed a value of 0.31 for a ductile solid [45]. Dugdale and Barenblatt arrived at a value of 0.40 for an elastic-ideal plastic mode I crack and an ideally brittle material, respectively [7, 28]. Falk *et al.* and Rice used a value of 0.88 in [31] and [74], in studies on dynamic fracture. Hillerborg [39] used a value of unity for concrete. Harper *et al.* [38] found that eq. (57) has a tendency to overestimate the cohesive zone length and wrongly motivate use of coarser meshes than called for and argued for a factor $M = 0.5$ to provide a conservative estimate for delamination in an orthotropic composite material. In general, the pattern seems to be a higher factor for more brittle materials like concrete, and a lower factor for more ductile materials.

It is important to resolve the cohesive zone length with a sufficient number of cohesive elements to provide a realistic representation of the cohesive fracture [31, 58, 89]. If the mesh is too coarse, two strategies exist: the first is to refine the mesh by increasing the number of elements spanning the cohesive zone length. This is not always feasible if the finite element model is large compared to the cohesive zone, e.g. an adhesive patch on a full vehicle model, since the run time may become prohibitive. The second approach is to reduce the cohesive strength. Alfano and Crisfield [1] found that when reducing the interface strength, the load/displacement curve did not change drastically for a double cantilever beam model, while the stress field did. Hence, the accuracy of the stress field is uncertain, but the load/displacement curve is still fairly stable.

Turon *et al.* [89] found that for a double cantilever beam specimen, below a certain interfacial strength, the resulting force was higher and more oscillatory than for lower strengths. Blackman *et al.*, on the other hand, found that for a double cantilever beam specimen of carbon fiber reinforced plastics, the load decreased with lower interfacial strength [13]. The same study also found a nonlinearity present in the beginning of the curve which did not appear for higher interface strengths. The cantilever arms were made of materials with similar properties in both studies and the geometries had similar dimensions. It is not clear why the discrepancy emerges. The initial crack length was shorter (22 mm) for Blackman than for Turon (55 mm), which may make a difference. Blackman also performed an analysis of a 90° peel test in the same study, using a cubic cohesive zone model. It was concluded that using a two-parameter cohesive zone model, there is a lack of uniqueness of the solution, since it was found that several combinations

of G_c and T_0 could give a reasonable estimation of the force. Others have also used the method of reducing the interfacial strength to use a coarser mesh, for example in [30].

Another expression for cohesive zone length for slender bodies was first given by Bao and Suo [5] as

$$l_{cz} = \left(E \frac{G_c}{T_0^2} \right)^{1/4} h^{3/4} \tag{58}$$

where h is the half-thickness of a laminate. This length is related to fiber bridging mechanisms in composites and therefore is not technically relevant in the current work, but it is interesting to compare eq. (58) to eq. (57). The main difference is that the thickness h of the laminate affects the cohesive zone length in a major way, which is reasonable for slender bodies.

Some skepticism about the possibility to increase the cohesive zone length by reducing interfacial strength was voiced by Harper and Hallett [38], who concluded that while it may be possible for mode I analyses of carbon epoxy composites, a similar reduction in mode II can cause excessive softening ahead of the crack tip due to very long cohesive zones. Harper and Hallett also made a distinction between the physical cohesive zone length, defined as the length over which irreversible damage processes occur ahead of a crack tip and the numerical cohesive zone length, over which cohesive elements are on the softening branch of their constitutive response. Based on the definition by Harper and Hallett, Álvarez *et al.* [2] stated that each integration point which is irreversibly damaged, but not broken, belongs to the numerical cohesive zone. The numerical cohesive zone length was then calculated as

$$l_{CZ,numerical} = \sum_{j}^{0<d<1} \frac{w_j}{2} l_e^i \tag{59}$$

i.e. by the sum over all integration points j for which $0 < \mathrm{d} < 1$, where l_e^i is the total length of the deformed midsurface of the element and w_j is the Gauss weight factor used, divided by two for Gauss-Legendre integration. This definition evaluates the contribution of each integration point. The authors used both classical linear cohesive elements and quadratic elements and found the quadratic elements superior and far less mesh-dependent. Due to the higher number of nodes per element, and increased accuracy of the quadratic shape functions in describing displacements, a coarser mesh can be used with retained accuracy, although too coarse a mesh will still yield inaccurate results. For industrial simulations of large structures such as adhesive bonds in airplanes or vehicles, such a reduction in element size can be crucial in reducing the computational cost.

4.5 The Xu-Needleman model

Most of the cohesive models available in commercial software are classic models. The commonly encountered exponential model was originally proposed by Xu and Needleman in 1994 [108]. The trapezoidal model is based on work by Tvergaard [90] and Tvergaard

and Hutchinson [91] from the 1990s. Some models, like the Xu-Needleman model, are based on a potential function, while others are non-potential-based. A potential-based model has the property of path-independence for mixed-mode fracture, i.e. it does not matter how a state of combined normal and shear damage is reached [56]. For uncoupled models, the normal traction is independent of the tangential opening separation and vice versa, making the model in general path dependent. A common critique of non-potential based models is that they are in general not thermodynamically consistent. This is problematic since such models are quite popular. Also, the tangent stiffness matrix is not guaranteed to be symmetric, in contrast to the potential-based models, where the components of the tangent stiffness matrix are given by the second derivatives of the potential. The potential models can be classified into two groups: potentials depending only on the displacement jump, and potentials which depend on the displacement jump as well as on internal variables representing the loading history [61].

In its original form, the potential ϕ in the Xu-Needleman model is given by

$$\phi = \phi_n + \phi_n \exp\left(-\frac{\Delta_n}{\delta_n}\right)\left\{\left[1 - r + \frac{\Delta_n}{\delta_n}\right]\frac{1-q}{r-1} - \left[q + \frac{r-q}{r-1}\frac{\Delta_n}{\delta_n}\right]\exp\left(-\frac{\Delta_t^2}{\delta_t^2}\right)\right\} \tag{60}$$

where $q = \frac{\phi_t}{\phi_n}$, i.e. the ratio of tangential fracture energy to normal fracture energy. Moreover, $r = \frac{\Delta_n^*}{\delta_n}$, where Δ_n^* is the value of Δ_n after complete shear separation with $T_n = 0$. The normal and tangential work of separation can be written as

$$\phi_n = e\sigma_{max}\delta_n, \qquad \phi_t = \sqrt{\frac{e}{2}}\tau_{max}\delta_t \tag{61}$$

respectively, with σ_{max} and τ_{max} being the peak tractions and δ_n and δ_t being the corresponding separations. Thus, the model is intrinsically different in the normal and shear directions, although some equalities can be enforced. For example, if the peak tractions and work of separation are equal, the displacements at peak traction will differ. Since the stresses and the tangent stiffness are based on a potential, the formulation is path-independent. Assuming $q = 1$, the tractions are given by the gradient of the potential, i.e.

$$\begin{aligned} T_n &= \frac{\partial\phi}{\partial\Delta_n} = \frac{\phi_n\Delta_n}{\delta_n^2}\exp\left(-\frac{\Delta_n}{\delta_n}\right)\exp\left(-\frac{\Delta_t^2}{\delta_t^2}\right) \\ T_t &= \frac{\partial\phi}{\partial\Delta_t} = \frac{2\phi_n\Delta_t}{\delta_t^2}(1 + \frac{\Delta_n}{\delta_n})\exp\left(-\frac{\Delta_n}{\delta_n}\right)\exp\left(-\frac{\Delta_t^2}{\delta_t^2}\right) \end{aligned} \tag{62}$$

where some terms in eq. (60) were eliminated and simplified.

It was recognized by van den Bosch *et al.* [95] that the Xu-Needleman model needs improvements in order to accurately describe mixed-mode failure. The ratio of fracture energies in Mode I and Mode II, provided by q, is often assumed to be 1, i.e. identical fracture energies in Mode I and II are adopted. For $q \neq 1$, the coupling between the modes

is non-physical. For example, if $q < 1$ (smaller fracture energy in Mode II), additional separation energy is required for normal fracture even when the failure shear strain has been reached. In [95], an analytical test case is devised where the model is first loaded in the normal direction and then in the tangential direction, and vice versa. If $\phi_n > \phi_t$ and normal loading is performed first, the total work of separation can be expected to increase monotonically from ϕ_t to ϕ_n with the normal displacement Δ_n. In other words, a higher work of separation should be required when first applying normal and then shear load than when applying a pure shear load, and as the normal failure separation is reached or exceeded, the work of separation should approach ϕ_n. Conversely, when first applying a shear and then a normal load, the work of separation should decrease monotonically from ϕ_n to ϕ_t. This is not the case with the classical Xu-Needleman model. Instead, the total work of separation as a function of Δ_n decreases to less than ϕ_t to a minimum and then approaches ϕ_n for large normal separations. In the other case, the total work of separation does not reach the expected value of ϕ_t for large Δ_t, but is found to equal ϕ_n irrespective of Δ_t, so that additional work is required even when the interface should have failed in shear. Because of this, van den Bosch *et al.* proposed to modify the shear traction by replacing the normal fracture energy ϕ_n with an independent shear fracture energy ϕ_t, yielding

$$T_t = -\frac{2\phi_t\Delta_t}{\delta_t^2}\left(1+\frac{\Delta_n}{\delta_n}\right)\exp\left(-\frac{\Delta_n}{\delta_n}\right)\exp\left(-\frac{\Delta_t^2}{\delta_t^2}\right) \tag{63}$$

while the normal traction is unchanged. Due to this change, the tractions can no longer be derived from a potential function. However, van den Bosch *et al.* were still able to verify that the model behaves correctly under mixed-mode loading and could fit simulation data to double cantilever beam experiments done by Benzeggagh and Kenane [11] at different mode-mixities with reasonable accuracy. Due to the non-potential based tractions, there is a path dependency, for example apparent if the failure separation in mode I is reached, which makes the normal traction become zero. For the test case previously described, it was found that the total work of separation increased monotonically from ϕ_t to ϕ_n when first prescribing a normal displacement, and decreased from ϕ_n to ϕ_t in the other case, as expected.

Similar problems with the original Xu-Needleman were identified by McGarry *et al.* for $q = 2$ [56]. When applying an initial tangential separation, it was found that negative work in the normal direction had to be provided, resulting in negative, i.e. repulsive, normal tractions for mixed-mode loading. This is because the work of separation for mixed-mode loading approaches ϕ_n, as seen in eq. (60) where the second term vanishes due to the exponentially decaying terms. The maximum normal traction after complete tangential separation was in [56] found to be

$$T_{n,max} = -\sigma_{max}\exp(-r)\frac{1-q}{r-1} \tag{64}$$

Clearly, this term only becomes zero when $q = 1$ and in other cases, spurious residual normal tractions exist. McGarry *et al.* further showed that for $q = 1$ the tangential

behavior will be erratic in case of mixed-mode over-closure. The tangential tractions were shown to decrease as the over-closure and turn negative for large over-closures. To overcome these issues, a modified potential was proposed in [56] on the form

$$\begin{aligned}\phi(\Delta_n,\Delta_t) =&\phi_n\left[1+\exp\left(-\frac{f(\Delta_t)\Delta_n}{\delta_n}\right)\left(\left(1-r+\frac{f(\Delta_t)\Delta_n}{\delta_n}\right)\left(\frac{1-q}{r-1}\right)\right.\right.\\ &\left.\left.-\exp\left(-\frac{\Delta_t^2}{\delta_t^2}\right)\left(q+\frac{f(\Delta_t)\Delta_n}{\delta_n}\left(\frac{r-q}{r-1}\right)\right)\right)\right]\end{aligned} \tag{65}$$

where

$$f(\Delta_t) = 1+m-m\exp\left(-\frac{\Delta_t^2}{\delta_t^2}\right) \tag{66}$$

and the parameter m provides additional coupling between normal and tangential behavior. The tractions now appear as

$$\begin{aligned}T_n(\Delta_n,\Delta_t) =&f(\Delta_t)\frac{\phi_n}{\delta_n}\exp\left(-\frac{f(\Delta_t)\Delta_n}{\delta_n}\right)\left\{\frac{f(\Delta_t)\Delta_n}{\delta_n}\exp(-\frac{\Delta_t^2}{\delta_t^2})\right.\\ &\left.+\frac{1-q}{r-1}\left[1-\exp\left(-\frac{\Delta_t^2}{\delta_t^2}\right)\right]\left[r-\frac{f(\Delta_t)\Delta_n}{\delta_n}\right]\right\}\end{aligned} \tag{67}$$

and

$$\begin{aligned}T_t(\Delta_n,\Delta_t) = 2\frac{\phi_n}{\delta_t}\frac{\Delta_t}{\delta_t}\exp\left(-\frac{\Delta_t^2}{\delta_t^2}\right)\exp\left(-\frac{f(\Delta_t)\Delta_n}{\delta_n}\right)\left[\left\{q+\left(\frac{r-q}{r-1}\right)\frac{f(\Delta_t)\Delta_n}{\delta_n}\right\}\right.\\ +\left\{\frac{m\Delta_n}{\delta_n}\left(\frac{f(\Delta_t)\Delta_n}{\delta_n}\exp\left(-\frac{\Delta_t^2}{\delta_t^2}\right)\right.\right.\\ \left.\left.\left.+\left(\frac{1-q}{r-1}\right)\left(1-\exp\left(-\frac{\Delta_t^2}{\delta_t^2}\right)\right)\left(r-\frac{f(\Delta_t)\Delta_n}{\delta_n}\right)\right)\right\}\right]\end{aligned} \tag{68}$$

The parameter m, appearing in eq. (66), controls the region of influence of pure tangential separation for mixed-mode conditions and the model degenerates to the Xu-Needleman model for $m = 0$ [56]. As m increases, the negative normal tractions after initial tangential separation are reduced, but it is also pointed out in [56] that negative normal tractions cannot be fully eliminated for a potential-based model where $q > 1$, i.e. with a higher work of separation in shear than under normal loading.

A study of the thermodynamic consistency of a number of cohesive models was done by Dimitri *et al.* [26]. The evaluated models comprise: the improved Xu-Needleman model proposed by van den Bosch *et al.* [95], a model by McGarry *et al.* [56] and the

two mixed-mode bilinear models by Högberg [41] and Camanho *et al.* [16]. It was found that all models, except for the improved Xu-Needleman model, were thermodynamically inconsistent due to incomplete dissipations or non-monotonic variations of the total fracture energy, i.e. the same problems identified by van den Bosch *et al.* for the original Xu-Needleman model in [95]. For the model by van den Bosch *et al.*, another issue is identified. Due to the non-potential based tractions, loading and unloading are defined separately and neither unloading or contact were covered in the original work. Dimitri *et al.* therefore proposed further improvements by defining a Helmholtz energy. The elastic energy is assumed to be additively decomposed according to [26]

$$\psi^e = \psi_n(\Delta_n) + \psi_n(\Delta_t) \tag{69}$$

where each term is only associated with one mode of displacement. Further, the damage is introduced through scalar damage variables with a multiplicative coupling according to

$$\psi = (1-d_n^n)(1-d_n^t)\psi_n(\Delta_n) + \psi = (1-d_t^n)(1-d_t^t)\psi_t(\Delta_t) \tag{70}$$

where $d_i^j \in [0,1]$ with $i = n,t$ and $j = n,t$. By applying the Coleman-Noll procedure to the Helmholtz energy in eq. (70), the traction vector becomes [26]

$$\boldsymbol{T} = (1-d_n^n)(1-d_n^t)\frac{\partial\psi_n(\Delta_n)}{\partial\boldsymbol{\Delta}} + (1-d_t^n)(1-d_t^t)\frac{\partial\psi_t(\Delta_t)}{\partial\boldsymbol{\Delta}} \tag{71}$$

where $\boldsymbol{\Delta} = [\Delta_n \Delta_t]$ is the displacement vector. A quadratic assumption for the elastic energies is made, yielding

$$\begin{aligned}\psi_n &= \frac{1}{2}K_n\Delta_n^2 \\ \psi_t &= \frac{1}{2}K_t\Delta_t^2\end{aligned} \tag{72}$$

where K_n and K_t are the cohesive stiffnesses in the normal and tangential directions, respectively. These elastic energies have the derivatives

$$\begin{aligned}\frac{\partial\psi_n(\Delta_n)}{\partial\boldsymbol{\Delta}} &= K_n\Delta_n\boldsymbol{n} \\ \frac{\partial\psi_t(\Delta_t)}{\partial\boldsymbol{\Delta}} &= K_t\Delta_t\boldsymbol{t}\end{aligned} \tag{73}$$

where $\boldsymbol{n}$ is the unit vector in the normal direction and $\boldsymbol{t}$ is the unit vector in the tangential direction. Using these derivatives, the traction vector becomes

$$\boldsymbol{T} = (1-d_n^n)(1-d_n^t)K_n\Delta_n\boldsymbol{n} + (1-d_t^n)(1-d_t^t)K_t\Delta_t\boldsymbol{t} \tag{74}$$

It was further shown that by writing the tractions on the form

$$\begin{aligned} T_n &= (1-d_n^n)(1-d_n^t)K_n\Delta_n \\ T_t &= (1-d_t^n)(1-d_t^t)K_t\Delta_t \end{aligned} \tag{75}$$

the cohesive stiffnesses can be written [26]

$$\begin{aligned} K_n &= \frac{\phi_n}{\delta_n^2} \\ K_t &= 2\frac{\phi_t}{\delta_t^2} \end{aligned} \tag{76}$$

by equating eqs. (62) and (75) for the tractions. Furthermore, the damage variables can be written

$$\begin{aligned} d_n^n &= 1-\exp\left(-\frac{\Delta_n}{\delta_n}\right) \\ d_t^n &= 1-\left(1+\frac{\Delta_n}{\delta_n}\right)\exp\left(-\frac{\Delta_n}{\delta_n}\right) \\ d_t^t = d_n^t &= 1-\exp\left(-\frac{\Delta_t^2}{\delta_t^2}\right) \end{aligned} \tag{77}$$

and by imposing non-decreasing damage variables, loading and unloading are dealt with automatically. Dimitri *et al.* also dealt with contact by further decomposing the Helmholtz energy according to [26]

$$\psi = (1-d_n^n)(1-d_n^t)\psi_n^+ + \psi_n^- + (1-d_t^n)(1-d_t^t)\psi_t \tag{78}$$

where

$$\psi_n^+ = \frac{1}{2}K_n\langle\Delta_n\rangle^2 \tag{79}$$

and

$$\psi_n^- = \frac{1}{2}K_p\left(\Delta_n - \langle\Delta_n\rangle^2\right)^2 \tag{80}$$

where K_p is a penalty stiffness for $\Delta_n < 0$ and K_n is the usual opening stiffness. This way, the opening stiffness degrades for $\Delta_n > 0$, while contact does not reduce the stiffness. The model was further implemented and verified for a patch test and matrix-fiber debonding [26].

Thus, a lot of proposed improvements to the original Xu-Needleman cohesive model exist. Some authors [56, 95] argue in favor of a non-potential based model while others [26] argue in favor of deriving a potential function from a Helmholtz free energy.

4.6 The PPR cohesive zone model

A notable potential-based model developed in recent years is the Park-Paulino-Roesler model [69]. The potential ψ for mixed-mode fracture in this model is written

$$\begin{aligned}\Psi(\Delta_n,\Delta_t) = \min(\phi_n,\phi_t) + \left[\Gamma_n\left(1-\tfrac{\Delta_n}{\delta_n}\right)^{\alpha}\left(\tfrac{m}{\alpha}+\tfrac{\Delta_n}{\delta_n}\right)^{m} + \langle\phi_n-\phi_t\rangle\right] \\ \times\left[\Gamma_t\left(1-\tfrac{|\Delta_t|}{\delta_t}\right)^{\beta}\left(\tfrac{n}{\beta}+\tfrac{|\Delta_t|}{\delta_t}\right)^{n} + \langle\phi_t-\phi_n\rangle\right]\end{aligned} \tag{81}$$

where ϕ_n, ϕ_t are the fracture energies in Mode I and II, respectively, Γ_n, Γ_t are energy constants, m and n are non-dimensional exponents and α, β are shape parameters for Mode I and II, respectively. The non-dimensional exponents m and n are defined as

$$\begin{aligned} m &= \frac{\alpha(\alpha-1)\lambda_n^2}{(1-\alpha\lambda_n^2)} \\ n &= \frac{\beta(\beta-1)\lambda_t^2}{(1-\beta\lambda_t^2)}\end{aligned} \tag{82}$$

where the initial slope indicators λ_n and λ_t are defined as the ratio of critical crack opening width to final crack opening width, i.e.

$$\lambda_n = \frac{\delta_{nc}}{\delta_n} \quad \text{and} \quad \lambda_n = \frac{\delta_{tc}}{\delta_t} \tag{83}$$

The smaller the value of λ_n or λ_t, the stiffer the initial elastic behavior in the respective modes. The energy constants are defined as

$$\begin{aligned}\Gamma_n &= \begin{cases}(-\phi_n)^{<\phi_n-\phi_t>/(\phi_n-\phi_t)}(\frac{\alpha}{m})^m & \text{for } \phi_n \neq \phi_t \\ -\phi_n(\frac{\alpha}{m})^m & \text{for } \phi_n = \phi_t\end{cases} \\ \Gamma_t &= \begin{cases}(-\phi_t)^{<\phi_t-\phi_n>/(\phi_t-\phi_n)}(\frac{\beta}{n})^n & \text{for } \phi_n \neq \phi_t \\ (\frac{\beta}{n})^n & \text{for } \phi_n = \phi_t\end{cases}\end{aligned} \tag{84}$$

thus being different depending on whether the fracture energies in normal and shear separation are equal or not.

By calculating the gradient of the potential function, the tractions in the normal and tangential directions can be evaluated as

$$\begin{aligned}T_n(\Delta_n,\Delta_t) = \frac{\Gamma_n}{\delta_n}\left[m\left(1-\tfrac{\Delta_n}{\delta_n}\right)^{\alpha}\left(\tfrac{m}{\alpha}+\tfrac{\Delta_n}{\delta_n}\right)^{m-1} - \alpha\left(1-\tfrac{\Delta_n}{\delta_n}\right)^{\alpha-1}\left(\tfrac{m}{\alpha}+\tfrac{\Delta_n}{\delta_n}\right)^{m}\right] \\ \times\left[\Gamma_t\left(1-\tfrac{|\Delta_t|}{\delta_t}\right)^{\beta}\left(\tfrac{n}{\beta}+\tfrac{|\Delta_t|}{\delta_t}\right)^{n} + \langle\phi_t-\phi_n\rangle\right]\end{aligned} \tag{85}$$

and

$$T_t(\Delta_n,\Delta_t)=\frac{\Gamma_t}{\delta_t}\left[n\left(1-\frac{|\Delta_t|}{\delta_t}\right)^{\beta}\left(\frac{m}{\alpha}+\frac{\Delta_n}{\delta_n}\right)^{m-1}-\beta\left(1-\frac{|\Delta_t|}{\delta_t}\right)^{\beta-1}\left(\frac{n}{\beta}+\frac{|\Delta_t|}{\delta_t}\right)^{n}\right] \\ \times\left[\Gamma_n\left(1-\frac{\Delta_n}{\delta_n}\right)^{\alpha}\left(\frac{m}{\alpha}+\frac{\Delta_n}{\delta_n}\right)^{m}+\langle\phi_n-\phi_t\rangle\right] \tag{86}$$

The thermodynamic consistency of the PPR model has been examined in a work [82], noting that the model was not originally derived based on a thermodynamics consistency principle. In [82], an anisotropic Helmholtz free energy function is first introduced as

$$\psi=\sum_{i=1}^{n}(1-d_i)\psi_i=(1-d_n)\psi_n+(1-d_t)\psi_t \tag{87}$$

where ψ_n is the energy related to the normal separation and ψ_t the energy related to tangential separation. d_n and d_t are damage variables related to damage in the normal and tangential directions, respectively, with values ranging from 0 to 1 where 0 indicates an undamaged material and 1 a fully damaged material. From these preliminaries, the dissipation inequality comes out as

$$D=\psi_n\dot{d}_n+\psi_t\dot{d}_t\geq 0 \tag{88}$$

and since the energies ψ_n and ψ_t are assumed to be positive, the second law of thermodynamics is satisfied if

$$\dot{d}_n\geq 0\quad\text{and}\quad\dot{d}_t\geq 0 \tag{89}$$

i.e. the damage variables need to be monotonically increasing. By rewriting the PPR potential in terms of the Helmholtz free energy function, the damage variables for this model become

$$d_n(\kappa_n,\kappa_t)=1-\frac{T_n(\kappa_n,\kappa_t)}{E_n\kappa_n} \tag{90}$$

and

$$d_t(\kappa_n,\kappa_t)=1-\frac{T_t(\kappa_n,\kappa_t)}{E_t\kappa_t} \tag{91}$$

where κ_n and κ_t are history variables representing the maximum normal and the absolute tangential opening attained during the loading history. The tractions $T_n(\kappa_n,\kappa_t)$ and $T_t(\kappa_n,\kappa_t)$ are provided by

$$T\prime_n(\kappa,\kappa_t)=\frac{\Gamma_n}{\delta_n}\left[m\left(1-\tfrac{\kappa_n}{\delta_n}\right)^{\alpha}\left(\tfrac{m}{\alpha}+\tfrac{\kappa_n}{\delta_n}\right)^{m-1}-\alpha\left(1-\tfrac{\kappa_n}{\delta_n})^{\alpha-1}(\tfrac{m}{\alpha}+\tfrac{\kappa_n}{\delta_n}\right)^{m}\right]$$
$$\times\left[\Gamma_t\left(1-\tfrac{\kappa_t}{\delta_t}\right)^{\beta}\left(\tfrac{n}{\beta}+\tfrac{\kappa_t}{\delta_t}\right)^{n}+\langle\phi_t-\phi_n\rangle\right] \tag{92}$$

and

$$T\prime_t(\kappa_n,\kappa_t)=\frac{\Gamma_t}{\delta_t}\left[n\left(1-\tfrac{\kappa_t}{\delta_t})^{\beta}(\tfrac{m}{\alpha}+\tfrac{\kappa_n}{\delta_n}\right)^{m-1}-\beta\left(1-\tfrac{\kappa_t}{\delta_t}\right)^{\beta-1}\left(\tfrac{n}{\beta}+\tfrac{\kappa_t}{\delta_t}\right)^{n}\right]$$
$$\times\left[\Gamma_n\left(1-\tfrac{\kappa_n}{\delta_n}\right)^{\alpha}\left(\tfrac{m}{\alpha}+\tfrac{\kappa_n}{\delta_n}\right)^{m}+\langle\phi_n-\phi_t\rangle\right] \tag{93}$$

which is very similar to eqs. (85) and (86). The only difference is that these tractions depend on the maximum normal and tangential separations reached at any stage of loading, while eqs. (85) and (86) are used with the current separations. E_n and E_t are the initial stiffness parameters in the normal and tangential directions, respectively. The stiffness parameters are evaluated as

$$E_n=-\frac{\Gamma_n}{\delta_n^2}\left(\frac{m}{\alpha}\right)^{m-1}(m-\alpha)\left[\Gamma_t\left(\tfrac{n}{\beta}\right)^{n}+\langle\phi_t-\phi_n\rangle\right] \tag{94}$$

$$E_t=-\frac{\Gamma_t}{\delta_t^2}\left(\frac{n}{\beta}\right)^{n-1}(n+\beta)\left[\Gamma_n\left(\tfrac{m}{\alpha}\right)^{m}+\langle\phi_n-\phi_t\rangle\right] \tag{95}$$

Due to the thermodynamic constraint that the damage variables must be monotonically increasing, the history parameters are given by

$$\kappa_n=\max\left\{\Delta_n\right\}\quad\text{and}\quad\kappa_t=\max\left\{|\Delta_t|\right\} \tag{96}$$

When unloading, the damage variables and the history parameters should retain their values, i.e. the crack should not, in general, heal due to decreasing displacement. There are three possible unloading cases for the PPR model: unloading in the normal mode, unloading in the tangential mode and simultaneous unloading in both of these modes. The unloading constitutive relations are given by

$$T_n^{\nu}\left(\Delta_n,\Delta_t\right)=T\prime_n(\kappa,\Delta_t)\left(\frac{\Delta_n}{\kappa_n}\right)^{\alpha_\nu} \tag{97}$$

and

$$T_t^{\nu}\left(\Delta_n,\Delta_t\right)=T\prime_n(\Delta_n,\kappa_t)\left(\frac{\Delta_t}{\kappa_t}\right)^{\beta_\nu} \tag{98}$$

where α_v and β_v are unloading parameters to describe different unloading paths. When these parameters are unity, the unloading is linear. For $\alpha_v < 1$, the unloading curve is concave and for $\alpha_v > 1$, it is convex and similarly for β_v. The dissipation inequality must hold in all of these cases for the model to be considered as thermodynamically consistent. Spring *et al.* [82] found that the original PPR formulation is not thermodynamically consistent for simultaneous unloading, as it was found that the damage decreases with decreasing separation. A coupled version was also tested, with a single history variable

$$\kappa = \max(\sqrt{\Delta_n^2 + \Delta_t^2}) \tag{99}$$

But this formulation was also found to be thermodynamically inconsistent for mixed-mode loading, as the damage variable was non-monotonic also for this model. The unloading constitutive relation for the coupled model is

$$\begin{aligned} T_n^\nu(\Delta_n, \Delta_t) &= T\prime_n(\Delta_n^\nu, \Delta_t^\nu) \left(\frac{\sqrt{\Delta_n^2+\Delta_t^2}}{\kappa}\right)^{\alpha_\nu} \\ T_t^\nu(\Delta_n, \Delta_t) &= T\prime_t(\Delta_n^\nu, \Delta_t^\nu) \left(\frac{\sqrt{\Delta_n^2+\Delta_t^2}}{\kappa}\right)^{\beta_\nu} \end{aligned} \tag{100}$$

where the modified displacements $\Delta_n^\nu, \Delta_t^\nu$ are given by

$$\begin{aligned} \Delta_n^\nu &= \frac{\Delta_n \kappa}{\sqrt{\Delta_n^2 + \Delta_t^2}} \\ \Delta_t^\nu &= \frac{\Delta_t \kappa}{\sqrt{\Delta_n^2 + \Delta_t^2}} \end{aligned} \tag{101}$$

To remedy this, a thermodynamically consistent version of the PPR model was proposed in [82]. In this proposed model, the unloading constitutive relation is

$$\begin{aligned} T_n^\nu(\Delta_n, \Delta_t) &= T\prime_n\left(\kappa_n, \kappa_t\right) \left(\frac{\Delta_n}{\kappa_n}\right) \\ T_t^\nu(\Delta_n, \Delta_t) &= T\prime_t\left(\kappa_n, \kappa_t\right) \left(\frac{\Delta_t}{\kappa_t}\right) \end{aligned} \tag{102}$$

where it can be noticed that the tractions $T\prime_n$ and $T\prime_t$ are now dependent on the maximum separation in both directions, rather than just the maximum normal or tangential separation. In addition, the shape parameters are no longer required. The components of the tangent stiffness matrix, D^ν are provided by the gradient of the unloading tractions. The stiffness matrix is thus found as

$$D^v(\Delta_n, \Delta_t) = \begin{bmatrix} D_{nn}^\nu & D_{nt}^\nu \\ D_{tn}^\nu & D_{tt}^\nu \end{bmatrix} = \begin{bmatrix} \frac{\partial T_n^\nu}{\partial \Delta_n} & \frac{\partial T_n^\nu}{\partial \Delta_t} \\ \frac{\partial T_n^\nu}{\partial \Delta_t} & \frac{\partial T_t^\nu}{\partial \Delta_t} \end{bmatrix} \tag{103}$$

and also need to be prescribed for each unloading case. For simultaneous unloading, i.e. $\Delta_n < \kappa_n$ and $|\Delta_t| < \kappa_t$, the stiffness matrix components are given by

$$\begin{aligned} D^{\nu}_{nn} &= T^{\nu}_{\prime n}(\kappa_n, \kappa_t)\frac{1}{\kappa_n} \\ D^{\nu}_{tt} &= T^{\nu}_{\prime t}(\kappa_n, \kappa_t)\frac{1}{\kappa_t} \\ D^{\nu}_{nt} &= D^{\nu}_{tn} = 0 \end{aligned} \tag{104}$$

This provides constant diagonal components and zero off-diagonal components. For normal unloading, the stiffness matrix components appear as

$$\begin{aligned} D^{\nu}_{nn} &= T^{\nu}_{\prime n}(\kappa_n, \Delta_t)\frac{1}{\kappa_n} \\ D^{\nu}_{tt} &= D_{tt}(\kappa_n, \Delta_t) \\ D^{\nu}_{tn} &= 0 \\ D^{\nu}_{nt} &= D_{nt}(\kappa_n, \Delta_t)\frac{\Delta_n}{\kappa_n}[3mm] \end{aligned} \tag{105}$$

and similarly for tangential unloading

$$\begin{aligned} D^{\nu}_{nn} &= D_{nn}(\Delta_n, \kappa_t) \\ D^{\nu}_{tt} &= T^{\nu}_{\prime n}(\kappa_n, \Delta_t)\frac{1}{\kappa_t} \\ D^{\nu}_{nt} &= 0 \\ D^{\nu}_{tn} &= D_{tn}(\Delta_n, \kappa_t)\frac{\Delta_t}{\kappa_t} \end{aligned} \tag{106}$$

The thermodynamic consistency of this model was verified by Parker *et al.* in the same paper [82]. Thus, to ensure thermodynamic consistency, it is not necessary to modify the traction-separation law for loading, but the unloading/reloading relationship must be changed. This is perhaps not surprising since it is stated explicitly by Park and Paulino, two of the inventors of the PPR model, that the unloading relationship is independent of the PPR potential [68]. Thus, the original model satisfies the dissipation inequality for pure loading, since the loading is based on a potential, but not for unloading/reloading where the model becomes reversible. Both the Xu-Needleman and the PPR model have been modified using a Helmholtz function in order to satisfy the dissipation inequality, perhaps indicating a growing trend. The requirements for using cohesive zones at finite displacements were discussed in [66], where it was mentioned that for small displacements the dissipation inequality is the only restriction on the formulation. For finite displacements, however, the balance of angular momentum and the principle of frame indifference

must also be fulfilled. It is mentioned that only elastic isotropic models with or without isotropic damage fulfill all these requirments. An novel elasto-plastic framework was proposed and generalized in [66]

4.7 Other aspects of cohesive zone models

The numerical integration scheme also matters for cohesive elements. It has been found that conventional Gauss integration results in oscillatory tractions if combined with too high cohesive stiffness [73, 79]. For this reason, other integration schemes such as Newton-Cotes and Lobatto integration are usually recommended. In recent years, an adaptive integration scheme was proposed by Bak *et al.* in [4]. In the deformed configuration, the separation was described in a local coordinate system defined on the middle surface, defined as

$$\bar{\boldsymbol{x}} = \boldsymbol{p} + \frac{1}{2}\left(\boldsymbol{u}^+ + \boldsymbol{u}^-\right) \tag{107}$$

where $\boldsymbol{u}^+ + \boldsymbol{u}^-$ is the separation of two initally coinciding points. The local coordinate system $(\boldsymbol{e}^1, \boldsymbol{e}^2, \boldsymbol{e}^3)$ is derived from curvilinear coordinate system (ξ, η) according to [4]

$$\begin{aligned} \boldsymbol{v}^\xi &= \frac{\partial \bar{\boldsymbol{x}}}{\partial \xi} \\ \boldsymbol{v}^\nu &= \frac{\partial \bar{\boldsymbol{x}}}{\partial \eta} \end{aligned} \tag{108}$$

and

$$\begin{aligned} \boldsymbol{e}^1 &= \frac{\boldsymbol{v}^\xi}{|\boldsymbol{v}^\xi|} \\ \boldsymbol{e}^3 &= \frac{\boldsymbol{v}^\xi \times \boldsymbol{v}^\eta}{|\boldsymbol{v}^\xi \times \boldsymbol{v}^\eta|} \\ \boldsymbol{e}^2 &= \boldsymbol{e}^3 \times \boldsymbol{e}^1 \end{aligned} \tag{109}$$

It can be noted that only $\boldsymbol{e}^1$ and $\boldsymbol{v}^\xi$ are parallel, due to η and ξ not being parallel, in general. The transformation tensor Θ between global and local coordinates is

$$\boldsymbol{\Theta} = \begin{bmatrix} e_1^1 & e_2^1 & e_3^1 \\ e_1^2 & e_2^2 & e_3^2 \\ e_1^3 & e_2^3 & e_3^3 \end{bmatrix} \tag{110}$$

An eight-node isoparametric brick element with a bilinear cohesive zone law was used, in which the opening displacements $\boldsymbol{\Delta}$ are defined as [4]

$$\boldsymbol{\Delta} = \boldsymbol{\Theta} \boldsymbol{N} \boldsymbol{q} \tag{111}$$

where $\boldsymbol{N}$ is the shape function vector and $\boldsymbol{q}$ is the nodal displacement vector. The shape functions are given by

$$\begin{aligned} N_1 &= \frac{1}{4}(1-\xi)(1-\eta) \\ N_2 &= \frac{1}{4}(1+\xi)(1-\eta) \\ N_3 &= \frac{1}{4}(1+\xi)(1+\eta) \\ N_4 &= \frac{1}{4}(1-\xi)(1+\eta) \end{aligned} \tag{112}$$

The shape function matrix is then given by [4]

$$\begin{aligned} \boldsymbol{N}^+ &= \begin{bmatrix} N_1 & 0 & 0 & & N_4 & 0 & 0 \\ 0 & N_1 & 0 & \cdots & 0 & N_4 & 0 \\ 0 & 0 & N_1 & & 0 & 0 & N_4 \end{bmatrix} \\ \boldsymbol{N}^- &= -\boldsymbol{N}^+ \\ \boldsymbol{N} &= \begin{bmatrix} \boldsymbol{N}^+ \boldsymbol{N}^- \end{bmatrix} \end{aligned} \tag{113}$$

The internal force vector can then be derived from the principle of virtual work as [37]

$$\boldsymbol{f} = \int_{\bar{S}_e} = \boldsymbol{N}^T \boldsymbol{\Theta} \boldsymbol{\tau} d\bar{S}_e = \int_\xi \int_\eta \boldsymbol{N}^T \boldsymbol{\Theta}^T \boldsymbol{\tau} |\boldsymbol{v}^\xi \times \boldsymbol{v}^\eta| d\eta d\xi \tag{114}$$

where $\bar{S}_e$ is the middle surface of the element in the deformed configuration and $\boldsymbol{\tau}$ is the traction vector obtained from the cohesive law. The element stiffness matrix can then be obtained as the derivative of the internal force vector with respect to the nodal displacements. The element stiffness matrix was written [4]

$$\boldsymbol{K_t} \approx \int_{\bar{S}_e} \boldsymbol{N}^T \boldsymbol{\Theta^T D \Theta N} d\bar{S}_e = \int_\xi \int_\eta \boldsymbol{N}^T \boldsymbol{\Theta}^T \boldsymbol{D \Theta N} |\boldsymbol{v}^\xi \times \boldsymbol{v}^\eta| d\eta d\xi \tag{115}$$

where $\boldsymbol{D}$ is given by the traction-separation law. It was assumed that the damage was purely in Mode I, with no rotation of the midplane of the interface. Under this assumption $\boldsymbol{\Theta}$ and the mode mixity β are constant. In addition to the usual Gauss and Newton-Cotes integration points, an adaptive integration scheme was proposed. The integration scheme was chosen based on the state of deformation. With no damage present, the integrands in eqs. (114) and (115) are second-order polynomials and can be integrated exactly using Gauss-Legendre integration, which was therefore chosen. When the interface is partially damaged, the integrands in eqs. (114) and (115) are not polynomials and have large variations of the slope, which means a higher-order quadrature is necessary. With full

damage, internal force vector and stiffness matrix are zero, except in the case of contact, which was not treated in [4]. It is further stated that convergence difficulties and spurious solutions appear due to too few elements in the cohesive zone. Oscillations in the force-displacement response of a model with too few elements in the cohesive zone were found to have a spatial period of one element length. It was found that Gauss-Legendre integration resulted in a smaller integration error than Newton-Cotes integration, since the outer integration points for Newton-Cotes integration are located on the element boundary, where the traction gradients are large when the element undergoes damage.

There is also a problem with cohesive models in that they do not guarantee uniqueness of the solution. In fact, for peel tests it has been shown that several combinations of G_c and T_{max} can give an almost identical peak force. Hence, some other experimental quantity needs to be compared to the simulation results to find the best parameter set. Suggestions have been made to use damage zone length or fracture displacement [13]. These quantities may, however, not be easily measured experimentally, if it is at all possible. For peel tests, the radius of curvature and other geometrical properties could be used also for calibration, while it is difficult, if not impossible, to measure how far ahead of the crack the material is damaged but not broken. Comparison to geometrical features, such as the peel arm curvature and thickness, is the path taken in the present study.

Recently, some interesting work has been done to optimize the structure of the peel arm during a peel test. As an example, Mergel *et al.* [57] did a shape optimization of the peel arm. The aim was to have a strong adhesion to the substrate while minimizing large strains in the peel arm. Additional constraints were placed on the volume of the peel arm, whereby the height and width were subjected to box-constraints. A finite rotation beam formulation was used, introduced by Sauer *et al.* [78]. It was found that the optimal shape was much thicker close to the point of application for the peel force than at the far end, while the width was smaller close to the peel front. Interestingly, this resembles the shape of a gecko spatula. The optimization was done on a microstructural level, with dimensions in the sub-micron range [57]. While interesting, this shape would not be suitable for packages, since the height cannot be allowed to be zero anywhere, as this would cause undesired contact between layers. Still, an optimal or improved structure might be achieved variable thickness of some layers. However, the sub-micron scale optimization done by Mergel *et al.* cannot be readily realized in package manufacturing.

5 Experimental methods

In this section, a background is provided to the experimental work in the present study. In addition to these methods, classic tensile tests have been used. Different experimental methods have been employed for peel test investigations in the literature, such as scanning electron microscopy (SEM) [65, 96, 99]. Neggers et al. [65] used SEM and optical microscopy for a metal-elastomer interface separated by peeling to study the dissipative mechanisms. A copper peel arm was peeled off a PDMS substrate in T-peel test and a 0° peel test. A fibrillation mechanism at the peel front was observed. In addition, Digital Image Correlation (DIC) was used to obtain the strain field in the 0° peel test. The

fibrillation mechanism turned out to be related to the surface roughness and to initiate by mechanical interlocking in the copper roughness valleys. The fibrillation was found to dissipate significant amounts of energy. It was also found that the copper surfaces were covered by of PDMS, showing that the crack had spread into the substrate. Since the fracture toughness of PDMS was known to be significantly larger than the interface adhesion energy, it was concluded that large stress separations must have been present. Similar results were obtained by Vossen et al. [99], who investigated reasons for the high work of separation. Three potential reasons were given: dynamic release of stored elastic energy by fibril fracture, the interaction of the fibrils with the adjacent deforming bulk material and the highly nonlinear behavior of the elastomer.

5.1 X-ray tomography

One of the novelties in the present work is the combination of the peel test with X-ray tomography. X-ray tomography is an experimental technique that can be used to characterize materials, for example by 3D imaging. A sample is placed between an X-ray source and a detector, schematically illustrated in Fig. 3. Three different scanning modes exist: absorption (used in this work), phase contrast and holotomography. In the absorption mode, radiographs are taken at angles between 0 and 180° or between 0 and 360°. Each radiograph shows the transmission of the X-rays through the material and this is linked to the absorption coefficient μ by the Beer-Lambert law. Contrast in the images is then given by the difference in absorption coefficient. The absorption coefficient is related to the atomic number and the density. In general, the absorption coefficient increases with atomic number, i.e. heavier elements absorb more X-rays than light elements. This means that it may be difficult to distinguish phases with similar atomic numbers, if their spatial distribution is not previously known. Light elements, such as polymers which contain a lot of carbon, may be difficult to distinguish from the background. Using a filtered backprojection algorithm, the volume can be reconstructed from the radiographs.

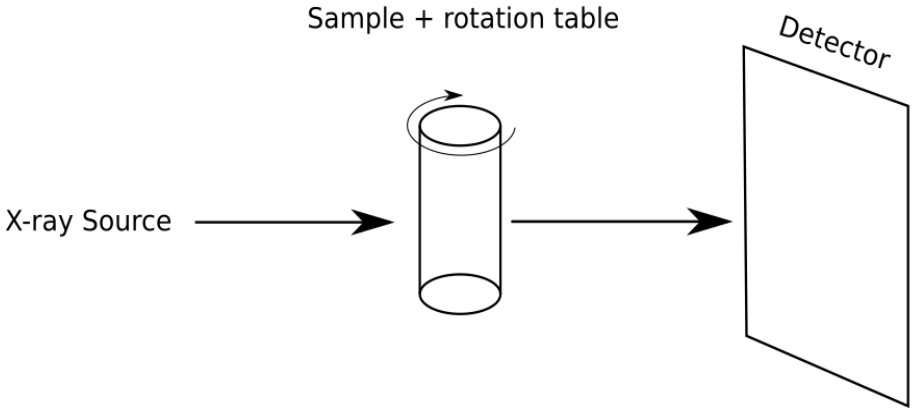

Figure 3: Principle of X-ray tomography. The sample is exposed to X-rays and rotated to obtain a 3D image.

Two main setups exist for X-ray tomography: X-ray tube (lab) tomography and synchrotron tomography. In lab tomography, a metallic X-ray tube is exposed to an ion beam, generating a polychromatic, divergent X-ray beam. Depending on the detector, the beam is called a fan beam if a line (1D) detector is used, or cone beam if a 2D detector is used. Due to the divergent beam, a geometric magnification of the sample will take place. The advantages of a lab tomography is that it is comparably cheap and can be installed in-house at any research department. The disadvantage is that the scan takes a long time compared to a synchrotron source, and a number of artefacts can arise due to the polychromatic and divergent nature of the beam. Beam hardening happens when a polychromatic beam passes through a dense material. Due to the density, lower energy ("soft") X-rays are attenuated while higher energy ("hard") X-rays pass through at a higher rate, raising the mean energy of the beam [14].

In a synchrotron facility, high intensity X-rays are generated by acceleration of electrically charged particles such as electrons. A white beam can be obtained or a monochromator used to obtain a single wavelength. The X-ray beam is parallel, with no magnification and if a monochromatic beam is used, there will be no beam hardening. A synchrotron is advantageous in that it offers a higher intensity beam and shorter scan time than a lab tomograph. The downside is that synchrotrons only exist at a few designated facilities and usually require applications for beam time that is provided after a proposal review process [77].

Once the X-ray scan is completed, a series of radiograms and slices are generated. These slices then have to be used with a reconstruction software to generate a 3D image. The 3D image shows the distribution of the absorption coefficient μ within the sample and the smallest unit is called a voxel (being the volume equivalent to a 2D "pixel"). The reconstruction can be done in two main ways. The first is by algebraic methods, solving a linear system of equations to obtain the coefficients μ throughout the sample. The other is backprojection of the transmitted intensity using Fourier transform.

To extend the range of experiment that can be performed, the sample can be held in different environments, such as a furnace, or be deformed in a load stage, to perform *in-situ* testing. Such *in-situ* experiments are sometimes referred to as 4D testing (3D + time). In this work, a load stage, permitting testing by pure tensile loading as well as by 90° peeling, has been used with X-ray tomography to provide *in-situ* measurements.

5.2 Digital Volume Correlation

The experimental technique Digital Volume Correlation (DVC) is based on Digital Image Correlation (DIC), which has been around since the 1980s [15] [19] [85] [84]. When doing DIC, a speckle pattern is created on the surface of a sample prior to experimental testing. During the experiment, the speckle pattern is tracked using a camera. By identifying distinct regions and tracking them from one state of deformation to the next, a full deformation pattern can be obtained. It should be pointed out that individual pixels are not being tracked, since it may be difficult to distinguish one point from another. Instead, a small square region of pixels is tracked, which ideally has a wider variation in light intensity values and can be distinguished from other regions more easily. To identify

the deformation the region has undergone, a cross-correlation coefficient must be defined, which measures the similarity of two regions. The simplest criteria is the cross-correlation coefficent, defined in two dimensions by

$$C_{CC} = \sum_{i=-M}^{M} \sum_{j=-M}^{M} f(x_i, y_i) g(x'_j, y'_j) \tag{116}$$

where $2M + 1$ is the number of pixels in each dimension, $f(x_i, y_i)$ is the grayscale value of the undeformed pixel and $g(x'_j, y'_j)$ is the grayscale value of the deformed pixel. Other correlation coefficients are the normalized cross-correlation (NCC), which normalizes by the mean of f and g and the sum of squared differences (SSD), which instead measures the difference of the pixels and hence should be minimized. It is also common to interpolate the displacement within pixels, called sub-pixel interpolation. The displacement yielding the highest correlation coefficient or the lowest squared difference is found by using an optimization algorithm [67].

The 2D DIC can be extended to 3D-surface DIC by using two cameras and stereoscopic vision [46], but the out-of-plane deformation can obviously only be measured on the surface of the sample and not within the sample. DVC is the extension of DIC to obtain the full 3D deformation field. Where DIC uses pixels for correlation, DVC uses voxels (volumetric pixels). Similar to DIC, DVC requires the material to have some inhomogeneous texture in order to distinguish regions [8]. One of the first use cases was ontrabecular bone [9]. There are different methods to obtain the volumetric image, most commonly using X-ray tomography, but confocal microscopy and optical slicing of transparent samples are other alternatives [8].

For any of the three methods, the deformation gradient can be calculated, but the number of components that can be calculated differs. For 2D DIC, only the in-plane derivatives of the in-plane displacments can be calculated. For 3D surface DIC, the in-plane derivatives of the out-of-plane displacements can be calculated. Since there is no information on the variation in the thickness direction, no out-of-plane derivatives can be computed. Finally, with DVC, the full 3D deformation gradient and strain field can be computed.

An interesting approach was taken by Shen and Paulino [81] who used DIC together with a cohesive model. To illustrate the method, it is noted that the FE formulation of a crack problem can be stated as

$$\int_{\Omega} \boldsymbol{\sigma} : \delta \boldsymbol{E} d\Omega - \int_{\Gamma_{ext}} \boldsymbol{T}_{ext} \cdot \delta \boldsymbol{u} d\Gamma_{ext} - \int_{\Gamma_{coh}} \boldsymbol{T}_{coh} \cdot \delta \Delta \boldsymbol{u} d\Gamma_{coh} = 0 \tag{117}$$

where Ω is the specimen domain [111]. In addition, Γ_{ext} is the boundary where the surface traction $\boldsymbol{T}_{ext}$ is applied, Γ_{coh} is the cohesive surface where the cohesive traction $\boldsymbol{T}_{coh}$ and crack opening displacement $\Delta \boldsymbol{u}$ exist, $\boldsymbol{\sigma}$ is the Cauchy stress tensor, $\mathbf{E}$ is the Green strain tensor and $\boldsymbol{u}$ is the displacement tensor. Following [81] and using the Galerkin discretization scheme provides [81]

$$(\boldsymbol{K}_b + \boldsymbol{K}_c(\mathbf{u};\boldsymbol{\lambda}))\boldsymbol{u} = \boldsymbol{F}_{ext} \tag{118}$$

where $\boldsymbol{K}_b$ is the global bulk material stiffness matrix, $\mathbf{K}_c$ the global cohesive stiffness matrix, $\boldsymbol{u}$ the global displacement vectors, $\boldsymbol{\lambda}$ a set of parameters related to the cohesive model and $\boldsymbol{F}_{ext}$ the externally applied force. The inverse problem of deciding $\boldsymbol{\lambda}$ with known displacements $\boldsymbol{u}$ was studied in [81] where the optimization problem was formulated as

$$\min_{\boldsymbol{\lambda}\in\mathbb{R}_m} \phi(\boldsymbol{\lambda}) = \left\|(\boldsymbol{u}^*(\boldsymbol{\lambda}) - \bar{\boldsymbol{u}})^T\right\|_2, \boldsymbol{\lambda} \in \boldsymbol{\Omega}_\lambda \tag{119}$$

where M is the number of input parameters, $\phi(\boldsymbol{\lambda})$, the difference between the numerical and experimental displacements, is the cost function to be minimized, $\boldsymbol{\Omega}_\lambda$ the feasible domain for cohesive zone parameters and $\bar{\boldsymbol{u}}$ the displacement field obtained from DIC. The numerical displacement is given by

$$\boldsymbol{u}^*(\boldsymbol{\lambda}) = \boldsymbol{K}_b^{-1}\hat{\boldsymbol{F}}_{ext}(\bar{\boldsymbol{u}};\boldsymbol{\lambda}) \tag{120}$$

where

$$\hat{\boldsymbol{F}}_{ext}(\bar{\boldsymbol{u}};\boldsymbol{\lambda}) = \boldsymbol{F}_{ext} - \boldsymbol{K}_c(\bar{\boldsymbol{u}};\boldsymbol{\lambda})\bar{\boldsymbol{u}} \tag{121}$$

Flexible spline interpolation was used to construct the cohesive model, with a number of control points. The vector $\boldsymbol{\lambda}$ is associated with the cohesive traction σ_c and the opening displacement $\Delta_{n,i}$ at each control point,

$$\boldsymbol{\lambda} = \left\{\sigma_1, \Delta_{n,1}, \sigma_2, \Delta_{n,2}, ..., \sigma_\mu, \Delta_{n,\mu}\right\} \tag{122}$$

The opening displacement control points must be positive and in ascending order to construct a reasonable cohesive zone law, which is written mathematically as [81]

$$\boldsymbol{\Omega}_\lambda = \left\{\boldsymbol{\lambda}|\lambda_i > 0, \Delta_{n,1} < \Delta_{n,2} < ... < \Delta_{n,\mu}\right\} \tag{123}$$

A Nelder-Mead optimization method was used to minimize the objective function. A limitation of the method is the assumption that the bulk material remins elastic. Fracture testing was done on single-edge notched beam specimens of PMMA bonded by adhesive and Garolite. As verification of the extracted cohesive zone models, the fracture energy of the finite element model was compared to the experimentally computed fracture energy, obtained from the force-displacement relationship. A good agreement was found in [81].

It has been recognized that capturing a crack opening at sub-pixel level for a fractured material can be extremly difficult. In response to this, a new DVC method called H-DVC (H for Heaviside), where H is for Heaviside, was developed recently in [92]. The method is based on similar methods as H-DIC in 2D [93], and stereoscopic H-SDIC for 3D surface analysis [94]. For classical DVC, the objective function is written by Valle *et al.* [92] as

$$
\begin{aligned}
S_i\left(\mathbf{P}\right) &= S_i\left(u, v, w, \frac{\partial u}{\partial x}, \frac{\partial v}{\partial x}, \frac{\partial w}{\partial x}, \frac{\partial u}{\partial y}, \frac{\partial v}{\partial y}, \frac{\partial w}{\partial y}, \frac{\partial u}{\partial z}, \frac{\partial v}{\partial z}, \frac{\partial w}{\partial z}\right) \\
&= \frac{f(\mathbf{X}_i) - \bar{f_D}}{\sigma_D} - \frac{g(\mathbf{x}_i) - \bar{g_{D'}}}{\sigma_{D'}}
\end{aligned}
\tag{124}
$$

where D denotes the domain under consideration and where u, v, w are the x, y and z displacements respectively. In addition, $\mathbf{X}$ the initial configuration and $\mathbf{x}$ the current configuration. Further, $\bar{f_D}$ and $\bar{g_{D'}}$ are the averages of the subregion gray level in the initial state D and the final state D', respectively, while σ_D and $\sigma_{D'}$ are the corresponding standard deviations. The inverse problem is to find the vector $\mathbf{P}$ of displacements and their gradients that satisifies $S_i(\mathbf{P}) = 0$. The mathematical formula for the position in the deformed configuration, using the H-DVC method, is

$$
\mathbf{x} = \mathbf{\Phi}(\mathbf{X}) = \mathbf{X} + \mathbf{U} + \frac{\partial \mathbf{U}}{\partial \mathbf{X}}(\mathbf{X} - \mathbf{X}_0) + \mathbf{U}' H(\mathbf{X} - \mathbf{X}_0) \tag{125}
$$

where $\mathbf{U}$ is the displacement vector and the third term is the first order derivative of $\mathbf{U}$ with respect to $\mathbf{X}$ at point $\mathbf{X}_0$, used for a Taylor approximation. The first three terms correspond to classic DVC methods [35] and the last term consists of a jump vector $\mathbf{U}'$ which is activated depending on the value of the Heaviside function $H(\mathbf{X} - \mathbf{X}_0)$. This corresponds to cutting the domain in two parts, D_1 and D_2, with different kinematics φ_1 and φ_2

$$
\begin{aligned}
\varphi_1(\mathbf{X}) &= \mathbf{X} + \mathbf{U}_1 + \frac{\partial \mathbf{U}}{\partial \mathbf{X}}(\mathbf{X} - \mathbf{X}_0) \text{ in domain } D_1 \, (H = 0) \\
\varphi_2(\mathbf{X}) &= \mathbf{X} + \mathbf{U}_2 + \frac{\partial \mathbf{U}}{\partial \mathbf{X}}(\mathbf{X} - \mathbf{X}_0) \text{ in domain } D_2 \, (H = 1)
\end{aligned}
\tag{126}
$$

A spherical coordinate system (r, θ, γ) is introduced to describe the opening plane defined by the Heaviside function. The jump vector $\mathbf{U}'$ is defined as

$$
\mathbf{U}' = \mathbf{U}_2 - \mathbf{U}_1 = (u', v', w') \tag{127}
$$

and the Heaviside function

$$
H(\mathbf{X} - \mathbf{X}_0) = H((x\cos\theta + z\sin\theta, \cos\gamma + y\sin\gamma - r) = H(r, \theta, \gamma) \tag{128}
$$

defines the cutting plane. The objective function for H-DVC is then written

$$
S_i(\mathbf{P}) = S_i\left(u, v, w, \frac{\partial u}{\partial x}, \frac{\partial v}{\partial x}, \frac{\partial w}{\partial x}, \frac{\partial u}{\partial y}, \frac{\partial v}{\partial y}, \frac{\partial w}{\partial y}, \frac{\partial u}{\partial z}, \frac{\partial v}{\partial z}, \frac{\partial w}{\partial z}, u', v', w', r, \theta, \gamma\right) \tag{129}
$$

i.e. six additional variables compared to eq. (124) which increases the computational cost considerably. A comparison of runtimes by Valle et al. [92] showed that a DVC calibration

of a volume of a few millions that took 15 min took 5h with H-DVC. The performed H-DVC method was verified with a simulated opening mode and a sliding mode deformation of a sphere inclusion in a cube and subsequently applied to a real tensile test of polypropylene with 3 weight % zinc filler particles. The model could identify displacement jumps in a satisfactory manner, while the classic DVC method was less successful in this [92].

The optimization-based methods can be used to obtain a better strain measure than with a classic macroscopic test. If the deformation is inhomogeneous to a substantial degree, a strain gauge at a single point will not capture this field. In the peel test, for example, the strain field at the top of the peel arm is not the same as that near the peel front. However, this is not taken into account when the displacement is measured at the top of the peel arm. The strain field can also be used for inverse analysis to calibrate parameters in constitutive models. This has been done for tensile tests [20] and for compression of concrete [32], but it has also been done for cohesive models [81] and crack propagation laws [53]. Speedup of DVC using Graphical Processing Units (GPUs) has been achieved as discussed in [101]. The resulting DVC algorithm implementation was used for the inverse problem of finding the displacement field in three different setups: a sequential implementation, a multithreaded CPU implementation and a GPU implementation. A substantial speedup was found using GPUs compared to the sequential process (18-23x) and even the multithreaded process (3-3.7x).

A graphical user interface (GUI) for DVC called TomoWarp2 has been developed by Tudisco *et al.* in recent years [88]. The program uses a local approach to DIC. The code is open source and uses both Python and C. To use the program, two images in the undeformed and deformed state must be provided, along with an estimated displacement range, the size of the region of interest and the spacing between analysis points. The program is parallelized through the use of Python multiprocessing libraries. The pixel search is implemented in C and connected to Python using Swig. The program has three main processes, a single management process, a single process handling data loading and communication, and numerous identical worker processes. The correlation coefficients are computed for all displacements in the displacement range for a particular pixel, and the worker processes handle a region each, allowing for parallelization [88]. Thus, user-friendly and modifiable software for DVC analysis is readily available.

6 Materials and experimental preparations

A packaging material for the food and dairy industry comprises several layers. A typical laminate is shown in Fig. 4. The inside layer has contact with the content of the package and is commonly made of a polymer like polyethylene, providing a barrier between the content and the other layers. The aluminum layer keeps out light and oxygen, and is bonded to the inside layer by an intermediate adhesive layer. This adhesion may also be due to the inside layer itself forming a bond to the aluminum during manufacturing, as the materials are rolled together at high temperature and subsequently cooled quickly. The paperboard provides stiffness to the structure and the laminate layer provides adhesion between the aluminum and the paperboard. The decor layer usually has a clay coat to

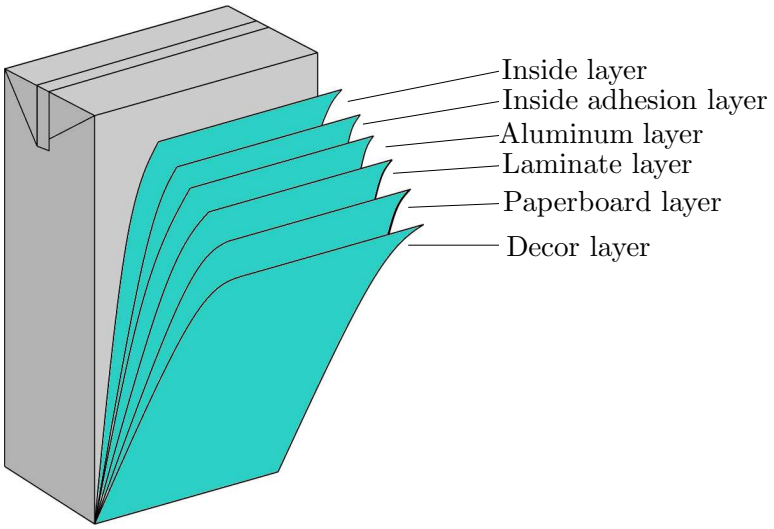

Figure 4: Schematic illustration of a typical packaging material laminate, comprising several layers of different materials such as polymer films, adhesive layers, paperboard and aluminum foil.

provide a good surface for printing.

Since packaging materials are manufactured in a system of rollers and extruders, there will be distinct material properties in the direction along which the material is produced, called the machine direction (MD). The laminate will also have a certain width, as set in the manufacturing process. The direction across the width is called the cross direction (CD). The third direction is the out-of-plane direction, often called Z-direction (ZD). The manufacturing process induces an anisotropy into the materials. The produced materials will usually be stiffest in MD, somewhat more compliant in CD and most compliant in ZD. A rule of thumb is that the MD stiffness is an order of magnitude higher than the CD stiffness and two orders of magnitude higher than the ZD stiffness. This is due to fibers in the paperboard, polymer chains in the inside polymer etc. aligning with the MD to a certain extent, making MD the preferred direction for load transfer. The reason ZD is so much more compliant is that it is much thinner than the other two directions and in the case of paperboard, the fibers mostly orient in the MD-CD plane. For this reason, it is also much harder to do experiments to evaluate ZD properties.

Different batches of materials were considered in the present experimental campaign. Three different batches were produced, with structures illustrated in Fig. 5. Each material is then described in more detail, outlining the reasoning behind each produced material and giving detailed descriptions of each laminate structure.

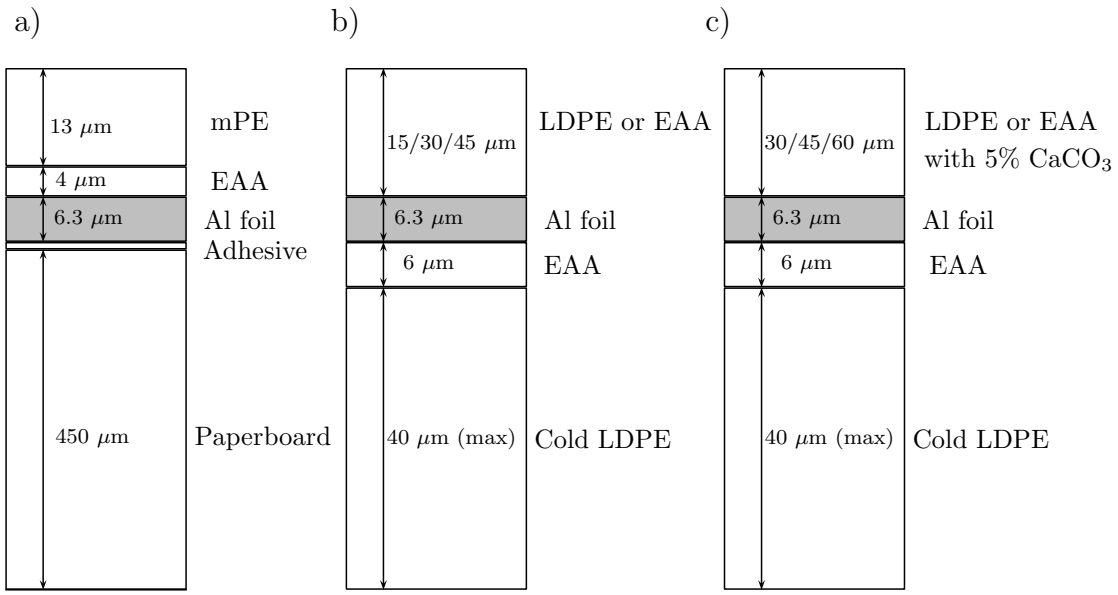

Figure 5: Sketch illustrating the different layers (not drawn to scale) in: a) Material 1, b) Material 2 and c) Material 3 .

The first type of material, denoted "Material 1" consists of a paperboard substrate about 450 μm thick with clay coat on the outside, a thin adhesive layer, a 6.3 μm thick aluminum foil, an inside polymer of ethylene acrylic acid copolymer (EAA) of 4 μm thickness and a 13 μm metallocene-catalyzed polyethylene (mPE) film. Of all three material types, Material 1 most closely resembles packaging materials used for commercial production. The EAA and mPE have almost identical mechanical properties and together formed the peel arm in the tests. The adhesion studied is that between the aluminum and the inside polymer, with the latter being the peel arm material.

Material 1 is creased, with lines guiding and decreasing the moment required for folding, as shown in Fig. 6. This introduces a heterogeneity into the structure. To prevent this from affecting measurements, it was always ensured that the peeling was done over non-creased regions. Moreover, all tests are done with peeling along MD.

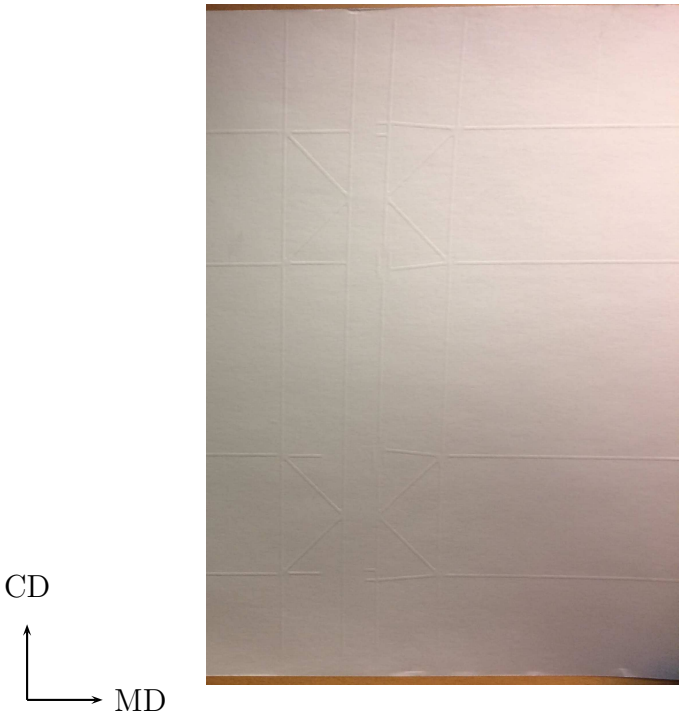

Figure 6: The crease pattern in Material 1.

When using Material 1, due to the small radius of the wheel and the high bending stiffness of the paperboard, the paperboard does not easily conform to the shape of the wheel. Because of this the paperboard does not always adhere well to the wheel/tape. In addition, there are usually zones of internal delamination within the paperboard after the significant bending required to fit the substrate onto the wheel. To prevent this from affecting the experiments, it was sometimes found necessary to peel past such zones by hand before starting the experiment. Since all the layers adhere to each other from the start, it is crucial to separate the inside polymer from the aluminum. At the same time it is also important not to delaminate the aluminum foil from the paperboard or cause delamination within the paperboard since this would cause the delamination to follow these paths instead of the interface between the inside polymer and the aluminum. Due to the very thin inside polymer, it is also crucial to avoid cohesive failure of the polymer when creating the peel arm.

The second type of material, denoted “Material 2”, was produced in an attempt to alleviate the aforementioned issues. To obtain a peel arm quicker and easier, a number of mylar sheets were placed between the inside polymer and the aluminum layer during laminate production. These sheets provide zones with little or no adhesion, which can be used to peel off the inside polymer directly, while the process for Material 1 was more manual and therefore unpredictable. The use of mylar sheets is shown in Fig. 7a.

Material 2 was produced with paperboard, but with the clay coat on the other side, weakly adhered to the aluminum foil. LDPE extruded at a low temperature adheres to the paperboard and EAA adheres to the Al foil. The low extrusion temperature of the LDPE causes weak adhesion to the clay coat, which means that the adhesive between Al foil and clay coat, the Al foil and the inside polymer can easily be peeled off from

the paperboard. This material conforms easily to the shape of the wheel, compared to Material 1 with stiff paperboard. Material 2 is shown in Fig 7b, where it is seen that a very clean separation from the paperboard is obtained. For the first material, separation of aluminum and paperboard could not be done without some amount of fibers sticking to the aluminum. Some of the clay coat usually adheres to the surface of the aluminum foil after separation, but this surface can be cleaned prior to experiments. The thickness of the peel arm in this round of materials is 15, 30 or 45 μm. The peel arm is made of EAA or LDPE, and the composition of Material 2 is illustrated in Fig. 5b.

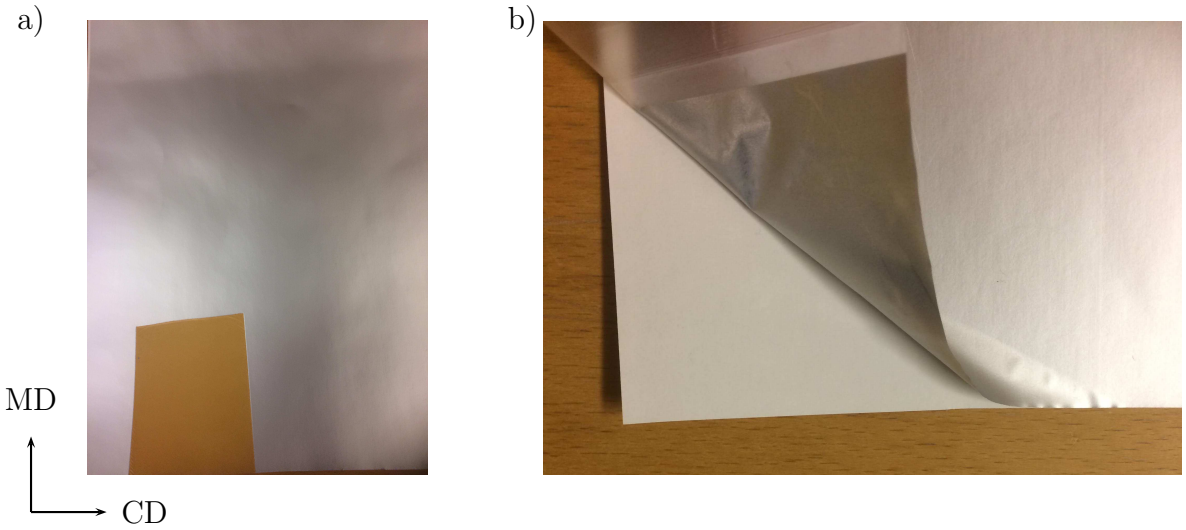

Figure 7: a) Brown mylar sheet making the creation of a peel arm easier. b) The aluminum foil and peel arm are easily separated from the paperboard in the second batch of materials.

To investigate the potential of using Digital Volume Correlation (DVC) with the peel test, a number of polymer films with different filler materials have also been produced. These polymer films have been scanned using X-ray tomography to assess their suitability for DVC, cf. Section 7. Based on the findings in Section 7, a peel arm material with 5 % $CaCO_3$ filler has been identified as a suitable candidate for DVC experiments. A third batch of materials was subsequently produced, denoted Material 3. Two different peel arm materials were chosen for Material 3: LDPE and EAA. In addition, the LDPE was produced both with thin paperboard with high out-of-plane stiffness, and with easily removable paperboard, similar to Material 2. Greater thicknesses of the peel arm were used compared to Material 2, since the smallest thickness of 15 μm was found to be hard to use in practice. The composition of the paperless variant of Material 3 is illustrated in Fig. 5c.

The experimental set-up has been developed to be able to perform 90° peel tests as well as tensile tests. In the development of the experimental set-up, certain criteria had to be met. To be able to bring the X-ray source and detector closer together in the tomograph, to enhance radiogram resolution, the rig dimensions have to be minimized.

Instabilities, friction and other sources of error in force/displacement measurement also have to be reduced.

A procedure for specimen handling and mounting was developed with the intention to be as reproducible as possible. First, the laminate is mounted to a wheel with adhesive tape. The next (optional) step is to place the wheel under pressure for up to three days. The reason for this is that the laminates with no paperboard can sometimes delaminate from the adhesive tape. By placing the samples under pressure and aging, the laminate/tape adhesion can be somewhat improved by curing. This step can be skipped when the laminate contains paperboard, because it is less of an issue then. Two different jigs for applying pressure are shown in Fig. 8a. In the metal jig shown at the top, the wheels are placed between two metal casings which are held together by the three black bolts. At the bottom of Fig. 10a, the second jig type is shown. Two wheels (one on each side of the white plastic cylinders) are placed inside the plastic casing which is tightened with a bolt.

After the pressing/curing step, the free end of the peel arm is attached to the grip of the loading stage. For repeatability, a jig is used to keep the length of the peel arm reasonably constant, as shown in Fig. 8b. The wheel is then mounted to a hub using a small bolt, mounted using roller bearings to reduce friction, as seen in Fig. 8c. Finally, the hub is placed on top of a transparent plastic tube and mounted on the test rig, as shown in Fig. 9. The plastic tube carries the load during testing and is transparent to X-rays, so that the setup itself does not block the X-rays during scanning. When the sample is mounted, the position of the grip needs to be adjusted and aligned with the wheel.

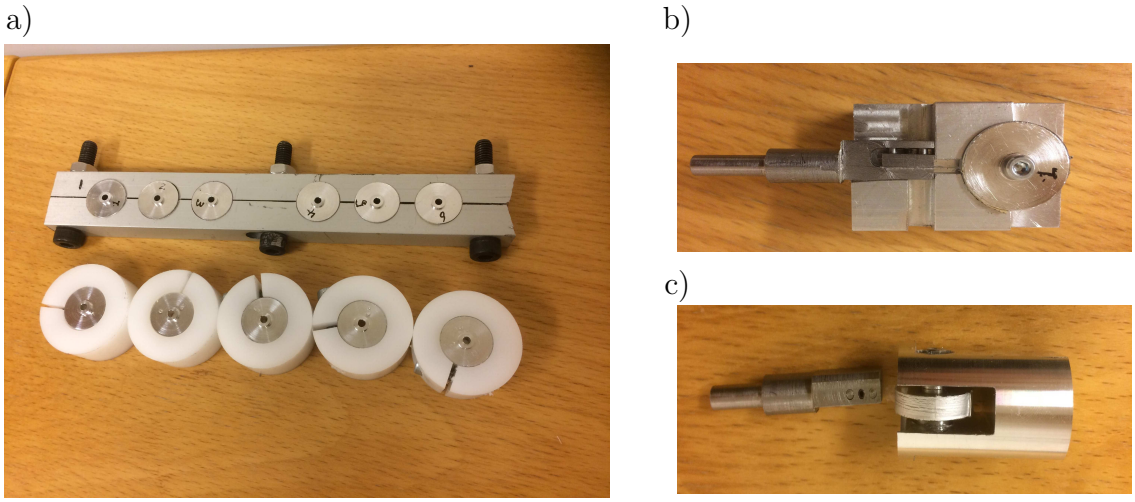

Figure 8: Steps in mounting procedure. a) First, the wheels and samples are put under pressure for 1-3 days to cure the bond (adhesive double-sided tape) between the laminate material and the wheel. b) The length of the peel arm is maintained between tests through the use of a jig. c) The wheel is attached to a metal hub.

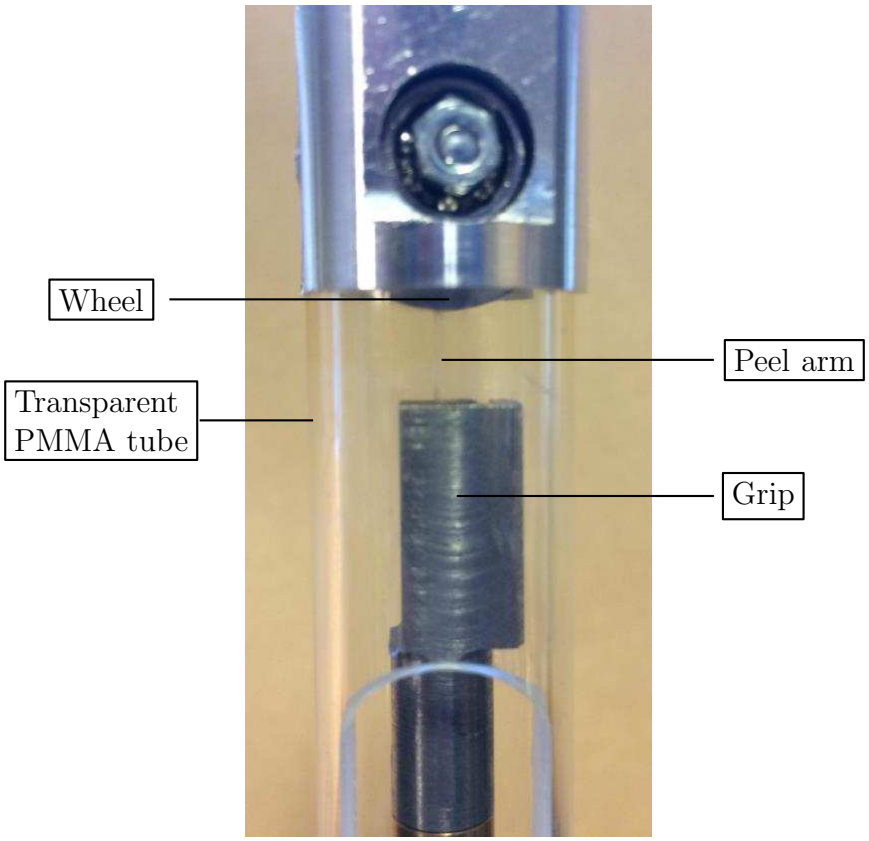

Figure 9: Zoomed-in sideview of the experimental set-up *ex-situ* (outside the tomograph). To perform peeling, the lower grip is moved downwards. The roller bearings reduce friction during rotation of the wheel. The plastic tube is transparent to X-rays and the hole helps with adjustments during setup.

When the hub has been mounted on the test rig, the test rig can be used *in-situ* (inside a tomograph) or *ex-situ*. Fig. 10 shows the test rig mounted *in-situ*. The test rig is placed between the X-ray source and detector. Note that the source and detector are spaced much further apart in Fig. 10 than during an experiment, for visualization purposes.

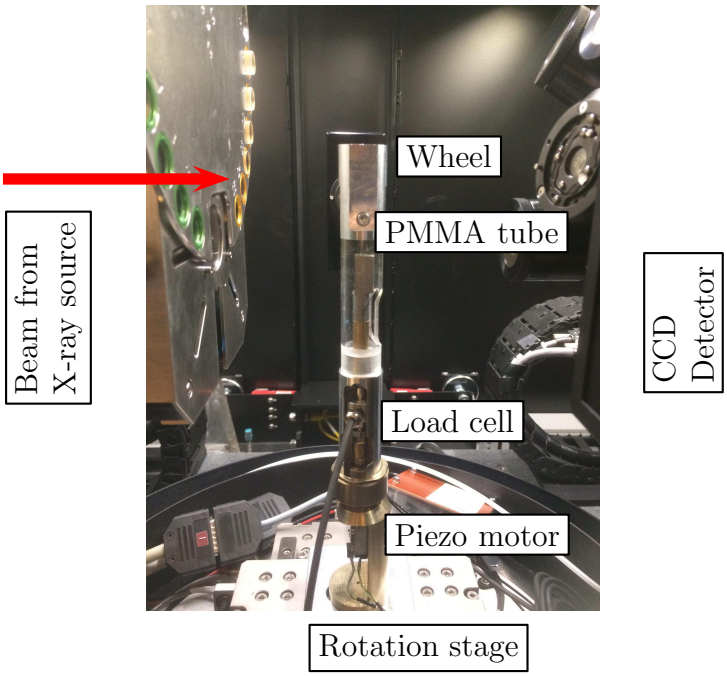

Figure 10: The peel test device developed for the present study with main components marked. The X-ray source is to the left, and the CCD detector to the right of the test specimen. Note that during the experiment, the source and detector are brought much closer to the device, to increase resolution. The diameter of the PMMA tube is 20 mm.

7 Preliminary notes on Digital Volume Correlation using particle-filled peel arm polymers

It is well known that the strain of the peel arm material has an influence on the measured peel force and fracture energy [49]. However, so far only the macroscopic strain has been measured or estimated, e.g. Karbhari and Engineer [47]. With the aid of experimental techniques such as Digital Image Correlation for 2D and Digital Volume Correlation for 3D, a full strain field can be obtained, cf. Section 5.2. To be able to use Digital Volume Correlation during a peel test, the peel arm can be filled with a suitable particle filler during manufacturing. A good filler must show sufficient contrast to the bulk material when scanned in the X-ray tomograph. It must also be sufficiently dispersed and relatively evenly spread. However, a perfectly even spread is not desired since there must be an inhomogeneous pattern to distinguish between particles and clusters of particles. Moreover, the filler must not significantly change the mechanical properties of the peel arm, compared to an unfilled polymer. With these criteria in mind, a preliminary study of different filler materials and fill ratios has been conducted. The bulk polymer material is LDPE, which is commonly used as a peel arm material. Three different filler materials are investigated: Calcium carbonate, talc and titanium dioxide. Three different fill ratios are also scrutinized: 2, 5 and 10 weight % of each type of filler. A reference batch of unfilled polymer is also produced for comparison of mechanical properties. X-ray scans of the polymer carrying 10 wt. % of each filler material is shown in Fig. 11.

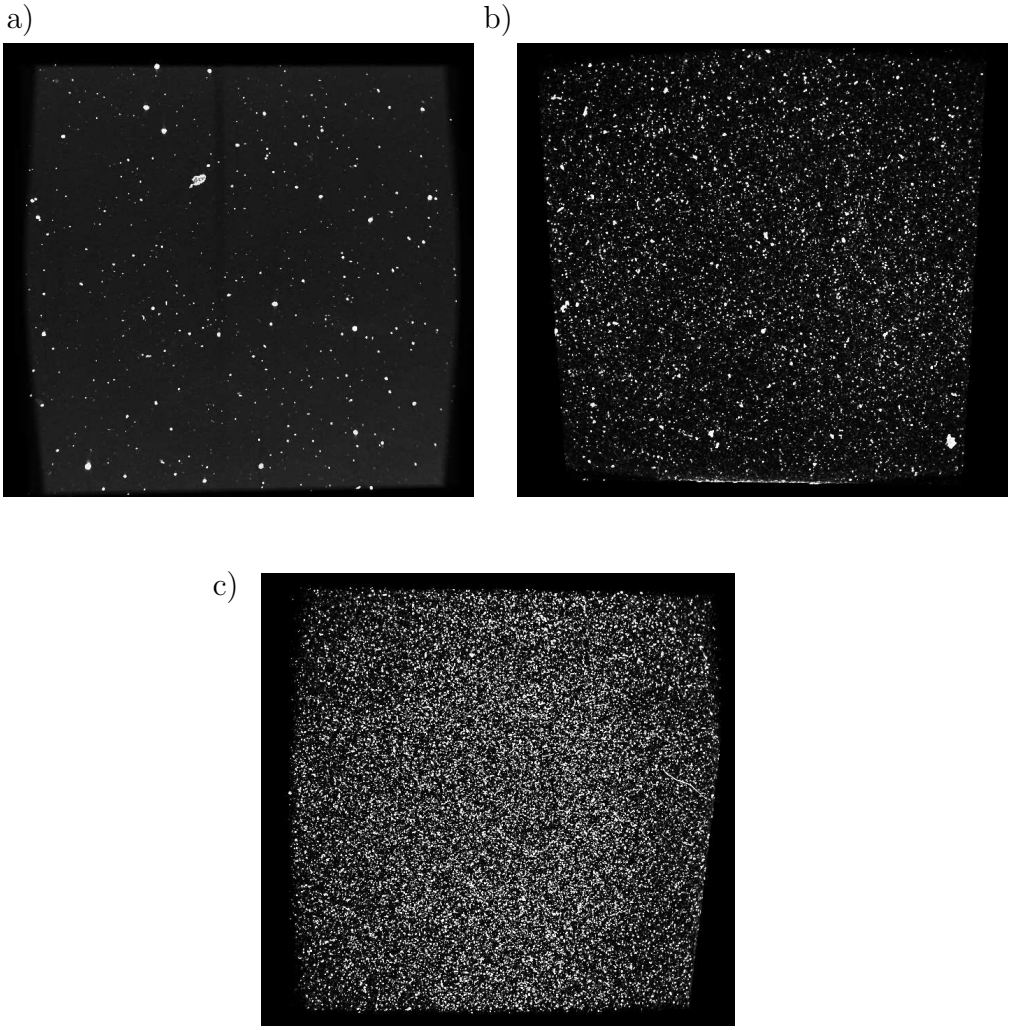

Figure 11: X-ray scans of LDPE filled with 10 wt % of a) Titanium dioxide, b) Talc and c) Calcium carbonate

Based on Fig. 11 and additional scans with lower fill grades, it can be concluded that both talc and titanium dioxide give insufficient patterning, while the calcium carbonate looks promising. Consequently, the calcium carbonate materials are studied further by performing tensile tests on filled and unfilled polymer samples. The results are shown in Fig. 12 and scans of polymer films carrying calcium carbonate with different weight fractions are shown in Fig. 13.

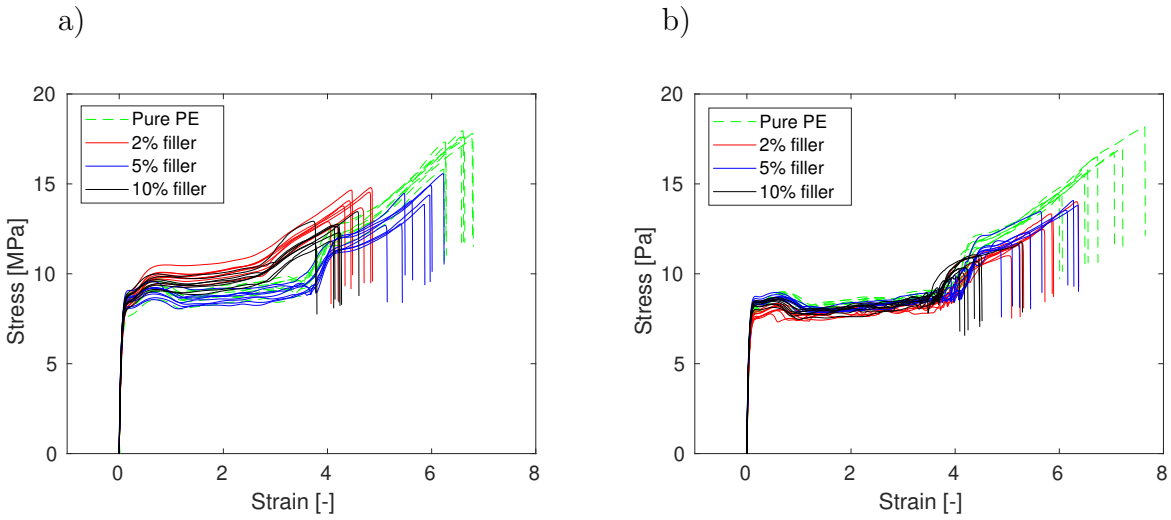

Figure 12: a) Force-displacement curve registered during tensile tests (loaded in MD) of pure and calcium-carbonate filled polymer samples. b) Samples tested in CD.

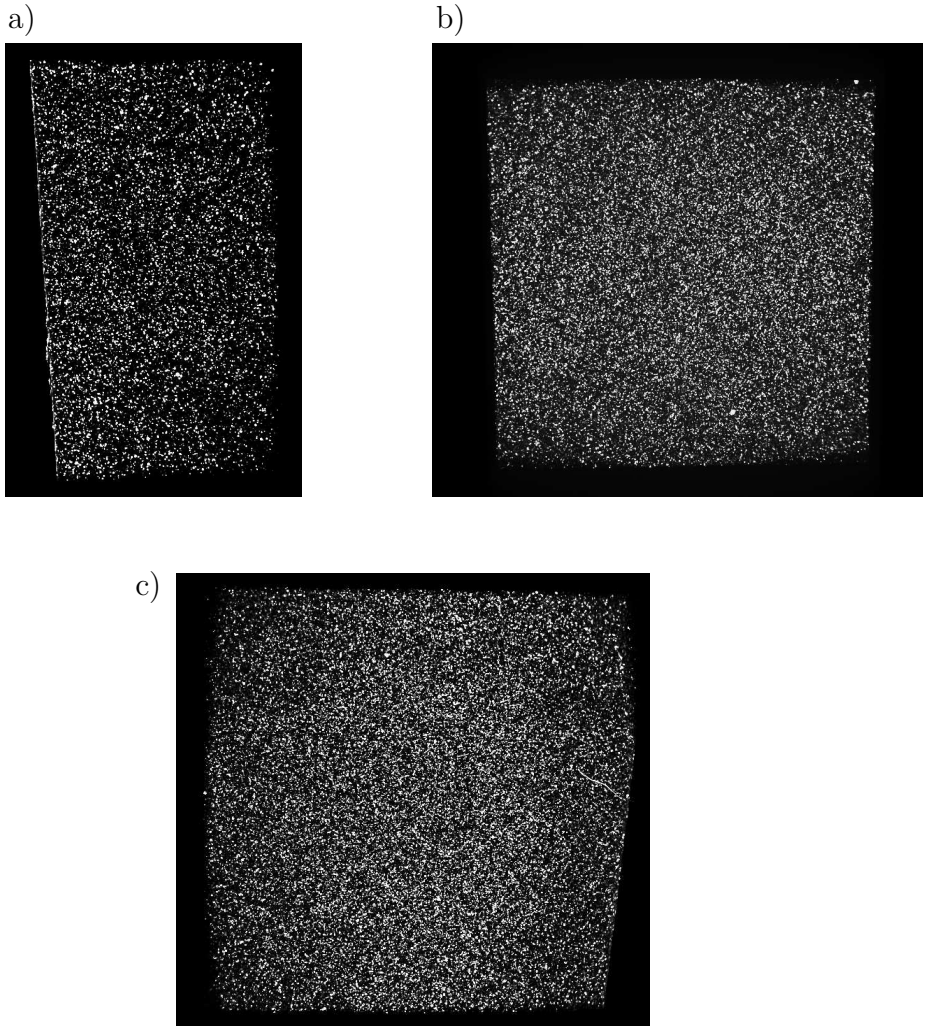

Figure 13: X-ray scans of PE filled with $CaCO_3$ with fill ratios of: a) 2 %, b) 5 % and c) 10 %

The unfilled and the 5 % filled polymers used in the tensile tests in Fig. 12 have an average thickness of 47 μm while the 2 and 10 % filled polymers have an average thickness of 100 μm. Even though there are some variations in the stress-strain response, the differences are minor. The more brittle response of the 2 and 10 % may be due to their lower thickness. The 5 % filled polymer most closely resembles the pure polymer in terms of stress-strain response and hence that fill ratio is chosen for further study. From Fig. 13, it can be seen that all fill grades look quite similar in terms of dispersion. The material with 2% filler is a bit more sparsely filled compared to the other fill ratios, but both 5 and 10 % are deemed sufficient. Based on this, laminate materials with 5 weight % $CaCO_3$ in the peel arm were produced manufactured for further experimental studies.

8 Experimental work

In this section, the experimental work done in the present study is summarized.

8.1 Tensile testing of the peel arm material

To mechanically characterize the peel arm material in Material 1, a series of tensile tests were performed. Tensile test specimens were produced from the peel arm material by chemically removing the LDPE film from the rest of the laminate. Dog bone shaped specimens were then punched out from the free-standing LDPE film and tested in a tensile load frame. The tensile tests were performed at four different deformation rates, 10 mm/min, 50 mm/min, 100 mm/min and 500 mm/min. The results from the tensile tests are shown in Fig. 14. A total of 6-9 tests were performed at each deformation rate and the error bars in Fig. 14 indicate the spread in the test data. Despite the quite wide span of deformation rates, it appears that the rate dependence is negligible and the peel arm material is therefore treated as rate independent for the remainder of the present study. The average thickness of the specimens was 20 μm.

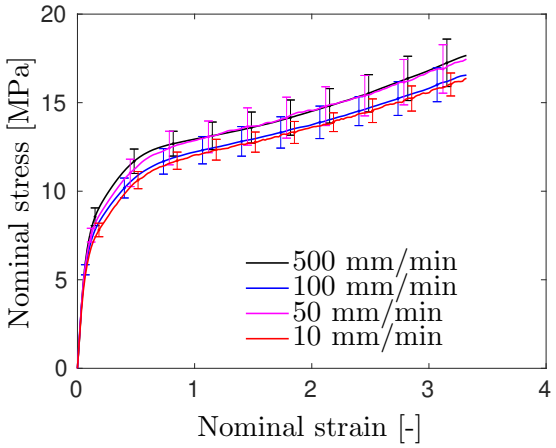

Figure 14: Results from tensile testing of the peel arm material at different deformation rates. The rate dependence is found to be negligible.

Images from an experiment done on Material 1 are shown in Figs. 16 and 17 and the corresponding force-displacement curve is provided in Fig. 15. Some images of the other batches are also shown.

8.2 *In-situ* peel tests

All three types of materials (Material 1, 2 and 3) were analyzed in the Zeiss Xradia XRM 520 Versa tomography system, hosted by the 4D Imaging Lab at Lund University, using 80 kV X-rays at 7 W power.

8.2.1 Material 1

A sample of the first material has been peeled 2.5 mm in Fig. 16 and 5 mm in Fig. 17. The sample is peeled at a rate of 0.5 mm/min. The width of the sample is 2 mm. The fracture appears to be interfacial, i.e. the fracture did not occur inside either the peel arm or the substrate. The images are also reasonably stable, even though relaxation has occurred during acquisition, which is evident from the two drops in force seen in Fig. 15.

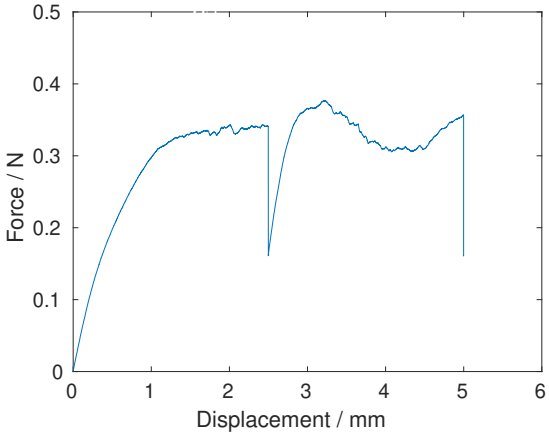

Figure 15: Force-displacement curve of an *in-situ* peel test of Material 1.

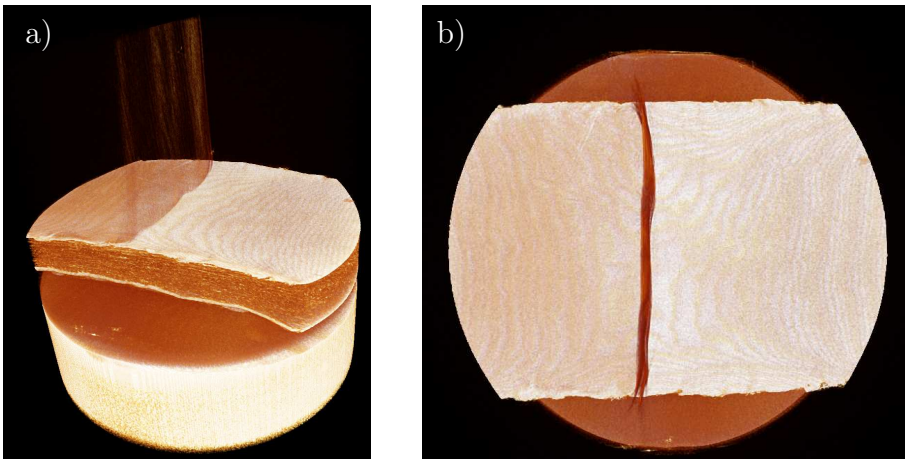

Figure 16: Example image from *in-situ* peel testing of Material 1 after 2.5 mm peeling: a) Side view and b) Top view.

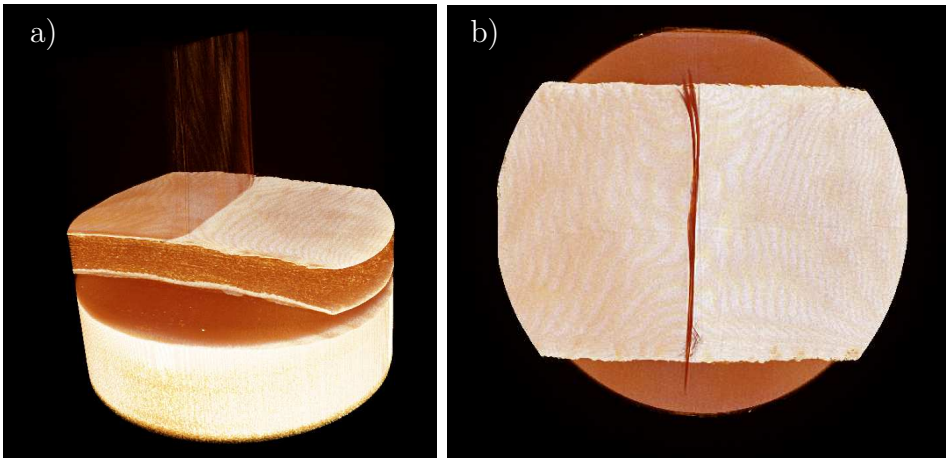

Figure 17: Example image from *in-situ* peel testing of Material 1 after 5 mm peeling: a) Side view and b) Top view.

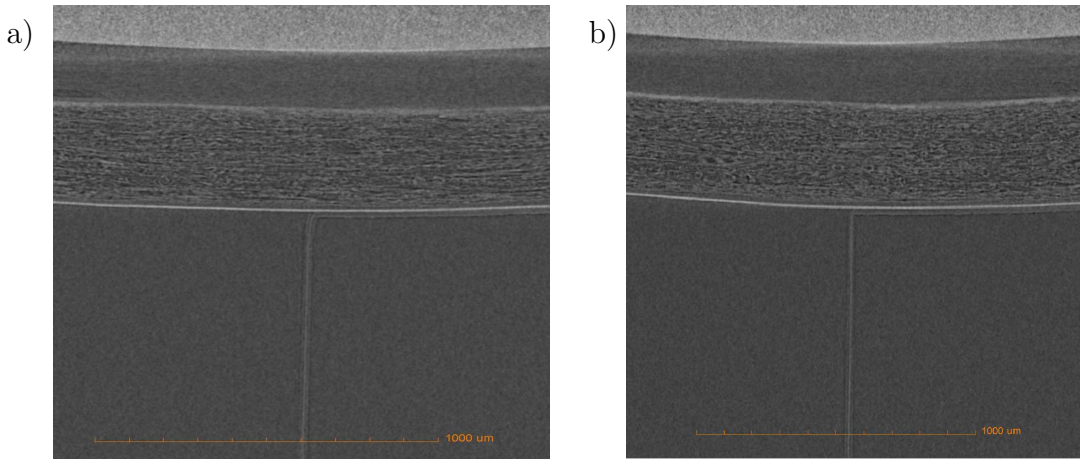

Figure 18: Example image from *in-situ* peel testing of Material 1 after 5 mm peeling: a) After peeling 2.5 mm and b) After peeling 5 mm.

Some differences between the sample at 2.5 and 5 mm peel displacement are evident. In both states, the sample delaminates first at the edges and later at the center, which is seen from the fact that the delamination is further progressed along the edges than in the middle. However, the pattern is more uniform at 5 mm than 2.5 mm displacement, which has a more wavy delamination front, as seen when comparing Fig. 16a and Fig. 17a. This might be due to edge distortions induced during sample cutting. It could also be due to the fact that during the creation of the peel arm, the peel arm can be peeled off in an inhomogeneous, uneven manner, owing to the manual nature of the process. This pattern may then persist from the beginning of the peeling process, until the peeling reaches a steady state. In both states, the laminate sticks well to the tape. This is relevant later on when comparing to the other laminates.

Another phenomenon is shown in Fig. 19. In some of the tests, the peel arm appears to split, with strands of adhesive sticking to the substrate. A possible reason is that the peel arm may split since it is made of two materials (EAA+mPE), cf. Fig. 5a. In the experiments, a split peel arm was found to correspond to a lower peak force than otherwise, indicating that the mode of fracture had been altered. It can thus be seen that in a single type of peel test, quite different failure mechanisms can be induced. This highlights the need to identify the damage mechanism involved to be sure of what type of process is actually being evaluated during a standard peel test.

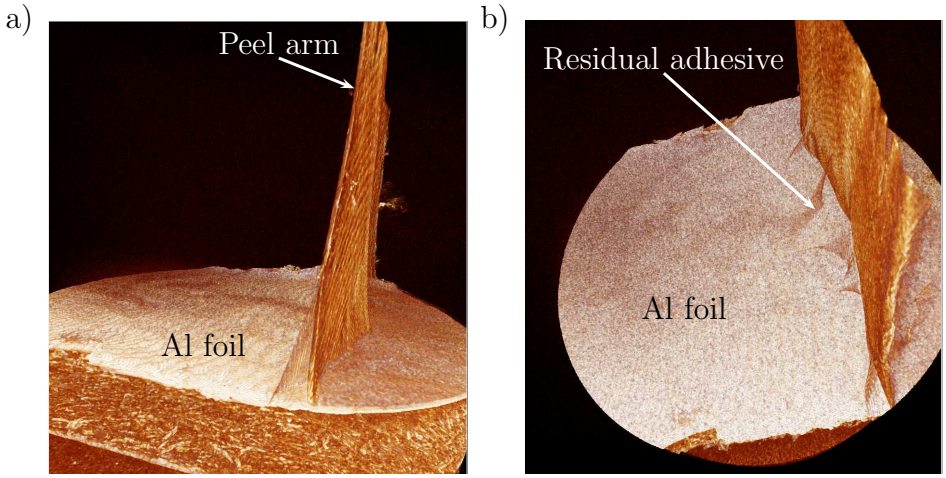

Figure 19: Example images from *in-situ* peel testing a) Laminate seen from the side. b) Peeling seen from above

The relaxation of this material was further studied *ex-situ*, i.e. outside the tomograph, as shown in Fig. 20. A sample was peeled to a force of 0.4 N and then held at the same displacement. After 1h, a typical scanning time in the tomograph, the force was reduced to 0.2 N and relaxation was still prevalent after 60+ hours. Hence, relaxation is not something that can be avoided in the lab tomograph.

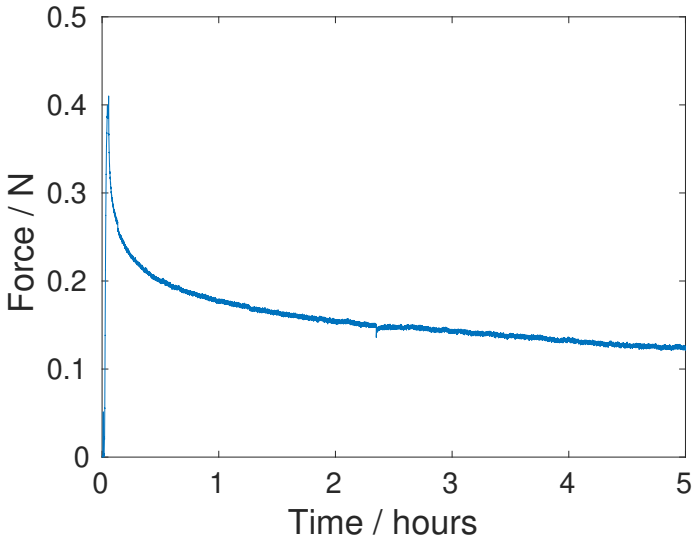

Figure 20: Force-time response during a relaxation test in the peel test load rig. The force is first increased to 0.4 N, after which the relaxation test commences.

8.2.2 Material 2

Side view 2D images of peel tests are shown in Fig. 21 and 22. Material 2 has a peel arm made of EAA, with a thickness of 30 μm and no paperboard in the substrate. The sample is peeled at a rate of 0.1 mm/min and the width of the sample is 3 mm. Note that the fibrous structure in the images is not paperboard but the cellulose core of the adhesive tape, which is a different tape from the one used in the images of the first material.

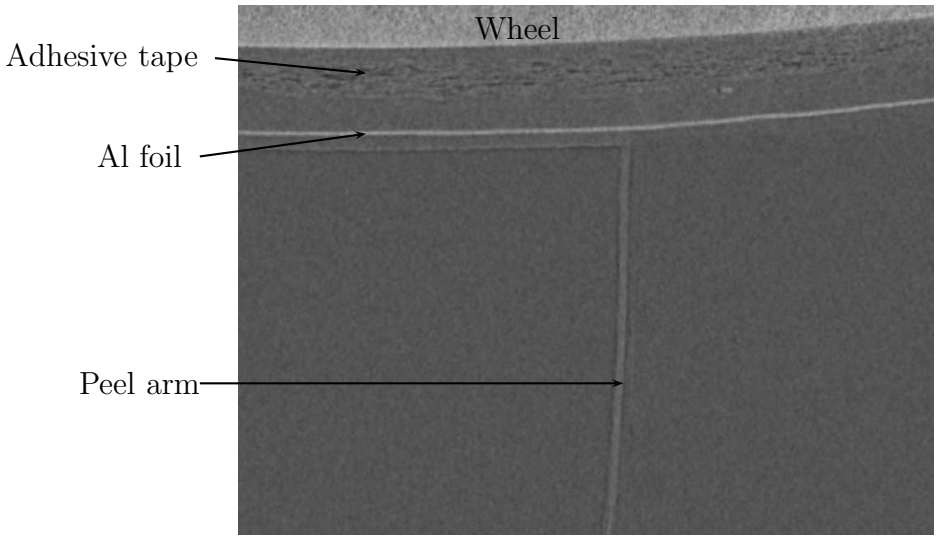

Figure 21: Images from *in-situ* peel testing of a material without paperboard at 0 mm displacement. The peel arm is made of EAA and unfilled.

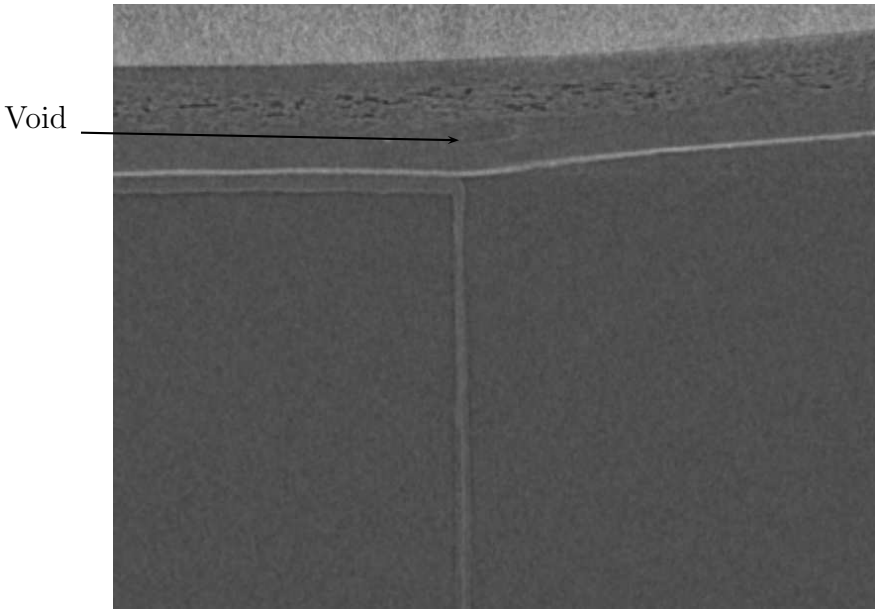

Figure 22: Images from *in-situ* peel testing of a material without paperboard at 0.4 mm displacement. Note the void between the tape and the polymer covering the aluminum.

In Fig. 22 it can be seen that a void has started to grow at the interface between the tape and the polymer on the wheel-side of the aluminum foil. Since the polymer in this layer was produced at a low temperature to ensure low adhesion to the paperboard, it is not surprising that it has low adhesion to other surfaces as well. Based on these and similar results, a procedure for improving the adhesion to the tape was developed. The procedure described in Section 6 was developed for this purpose. The laminates without paperboard were placed on the wheel and then put under pressure for some time.

8.2.3 Material 3

Fig. 23 shows the force-displacement curve for a laminate material with a filled polymer acting as the peel arm. The 3D images acquired at 0 and at 1.5 mm displacement, respectively, are shown in Fig. 24. The substrate consisted of a thin paperboard, adhering to the aluminum foil and the peel arm was a 60 μm thick LDPE film with 5 weight % $CaCO_3$. The paperboard was thinner and with higher out-of-plane stiffness than for Material 1.

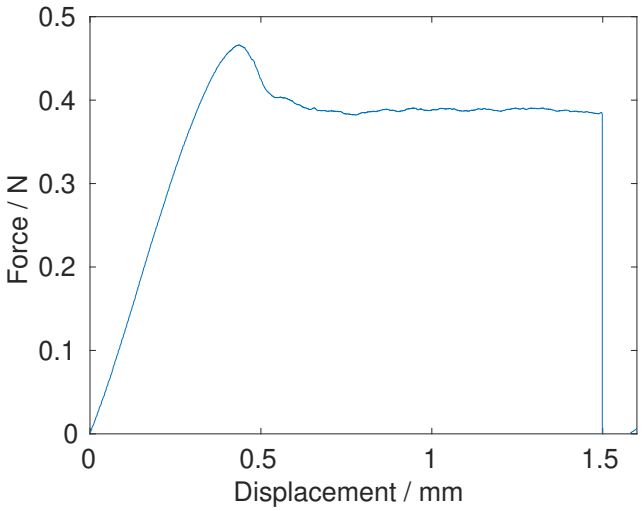

Figure 23: Force-displacement curve for a peel test with a filled polymer.

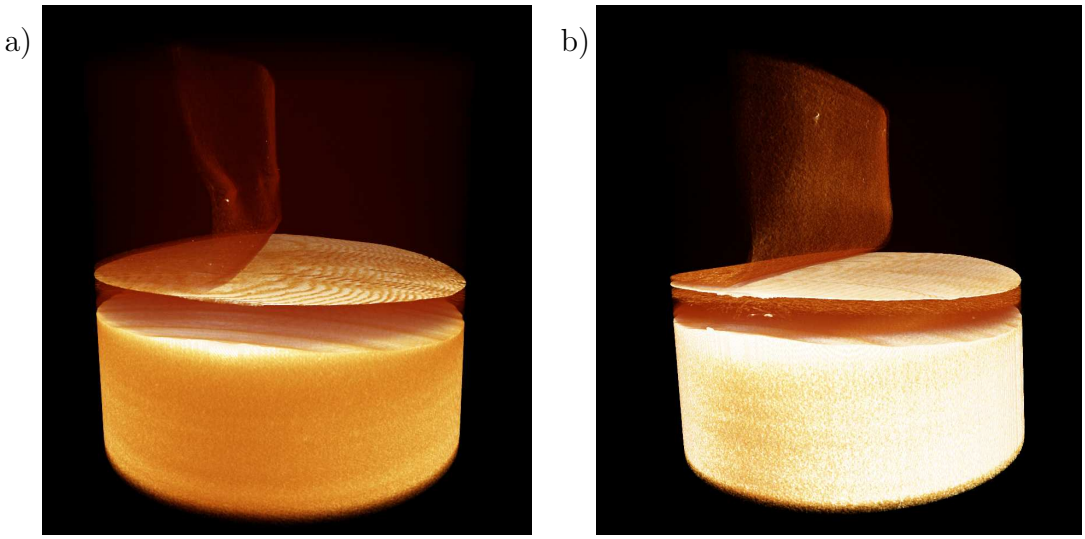

Figure 24: Images from *in-situ* peel testing with the filled LDPE material as peel arm. The images are acquired a) Before peeling and b) After 1.5 mm peeling.

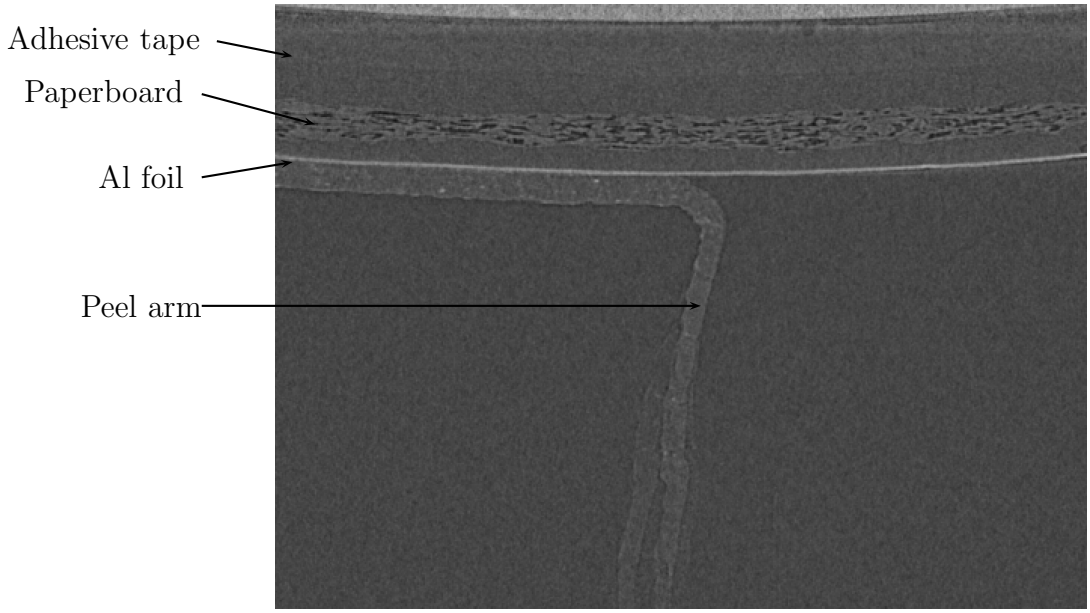

Figure 25: Image from *in-situ* peel testing of the filled PE material, before peeling.

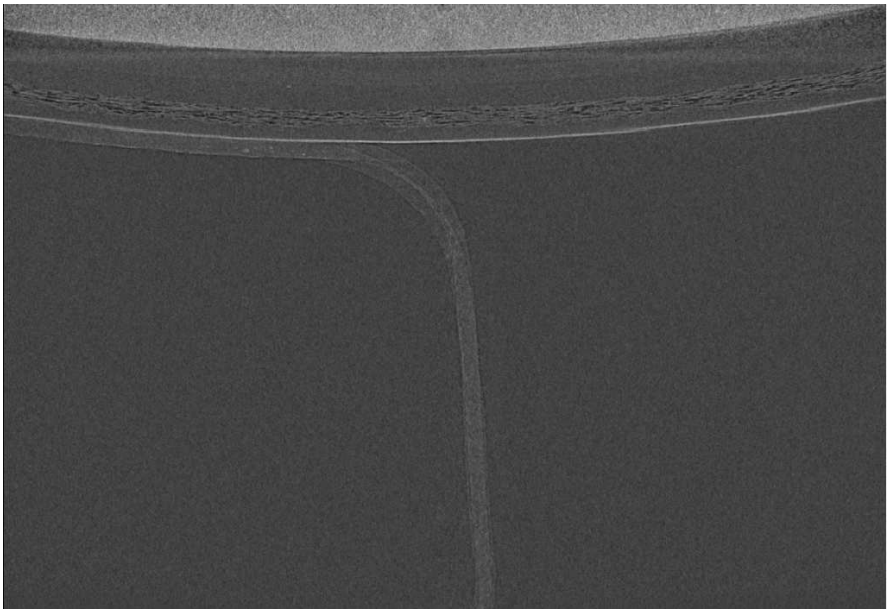

Figure 26: Image from *in-situ* peel testing of the filled PE material, after 1.5 mm peeling.

Looking at the peel front in Fig. 24b, it appears that the peel front is much more straight than in the original material. As seen in the 2D image after peeling in Fig. 26, the peel arm is also much more rounded than for the first two materials. A similar experiment of the same material is shown in Fig. 27.

a) b)

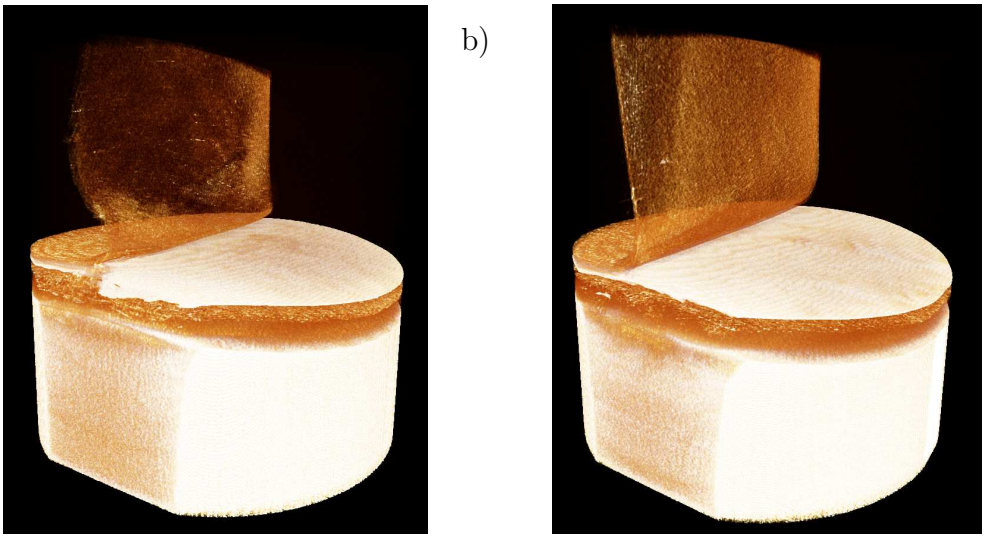

Figure 27: Images from *in-situ* peel testing with the filled PE material as peel arm. a) Before peeling. b) After 3 mm peeling.

8.3 Pilot study at the PSI synchrotron

Additional experiments were done at the TOMCAT beamline at the Paul Scherrer Institute (PSI) in Switzerland. With the higher flux and parallel beam provided at the synchrotron, it was possible to obtain images at a much higher rate than in the lab. It was even possible to perform *in-situ*, continuous, peeling. The exposure time was set to 1 ms and the voxel size to 1.6 μm. Most of the PSI tests focused on Material 1 and on one of the materials with a filled polymer as the peel arm. The material with a filled polymer had a substrate of thin paperboard with extra out-of-plane stiffness so that it could easily be attached to the wheel, while ideally preventing tape delamination previously associated with the materials containing no paperboard. The first peeling rate was 0.07 mm/min or about 1.16 μm/s, which allowed continuous scanning without too much movement relative to the voxel size. Two other rates, 0.2 mm/min and 0.3 mm/min, were also used. To prevent radiation damage, the samples were not scanned continuously, but every 30 s until the end, with an intermittent period where the sampling rate was increased. The period of higher sampling rate was chosen at a time when the peeling was believed to have stabilized. Some preliminary results from the first experiment done at PSI is shown in Figs. 28. The test was done with Material 1 and the lowest peel rate previously mentioned. A total of about 110 scans were done during the experiment and scan number 1, 50 and 100 are shown in Figs. 28a-c. Note that due to imperfect alignment between the grip and the wheel, the peel arm was not perfectly vertical at the synchrotron experiments, but should still be acceptable since a 90° angle between the wheel and the peel arm.

a)

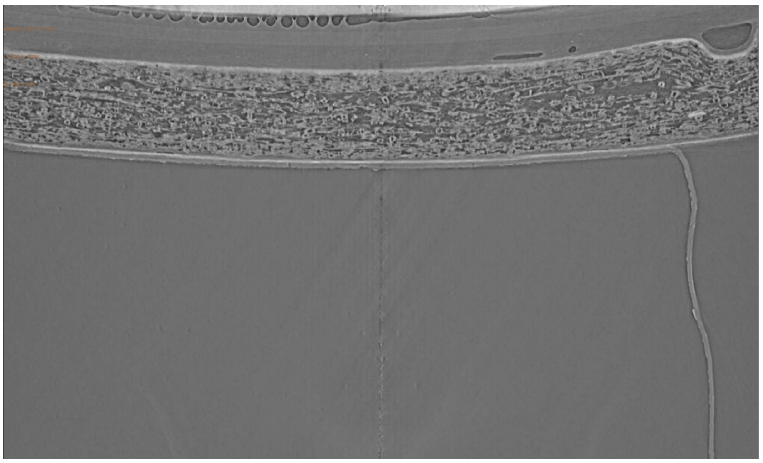

b)

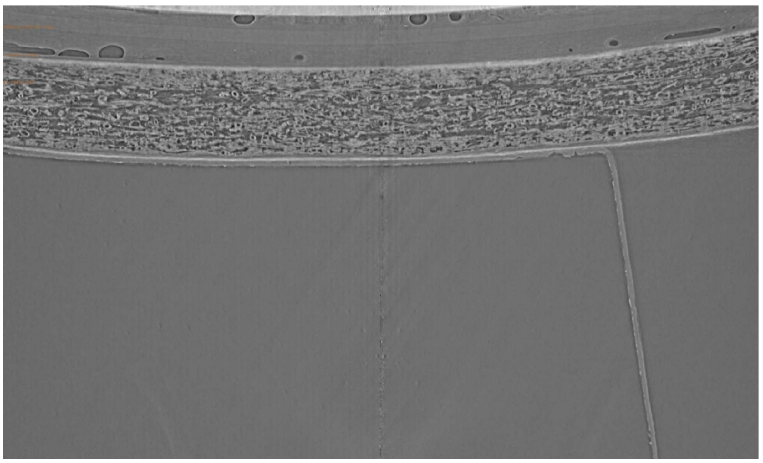

c)

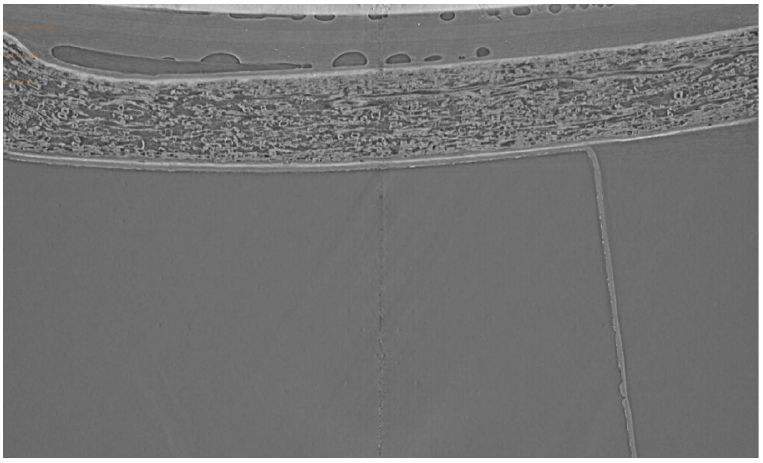

Figure 28: Images from continuous peel testing at PSI with Material 1 taken at scan number a) 1, b) 50 and c) 100.

The resolution of the images in Figs. 28a-c is a lot better than for the images obtained in the lab tomograph. It appears that the adhesion to the tape was not optimal in this particular test, especially in Fig. 28c. Still, it seems to have been acceptable in Figs. 28b and 28c, at the start and in the middle of the test, respectively. Some variation in the

peel arm thickness can be seen, particularly in Fig. 28c, where the peel arm looks close to failure at the lower end of the peeled off part. Further analysis of the data from PSI is part of future work.

9 Numerical simulations

A numerical model of the peel test has been developed in the commercial finite element software Abaqus. The model uses a van der Waals hyperelastic model for the peel arm material and a bilinear cohesive law for the interface between the peel arm and substrate. Consistent with [59, 60], a Van der Waals hyperelastic model was adopted for the peel arm material. Assuming incompressibility, the strain energy potential function for this model has the format

$$\tilde{U}\left(I_2\right) = \mu\left\{-\left(\lambda_m^2-3\right)\left[\ln\left(1-\eta\right)+\eta\right]-\frac{2}{3}a\left(\frac{I_2-3}{2}\right)^{3/2}\right\}, \quad \eta=\sqrt{\frac{I_2-3}{\lambda_m^2-3}} \tag{130}$$

This form is in fact somewhat special, assuming only a dependence on I_2. In the most general form, I_2 is replaced by $\tilde{I} = (1-\beta)I_1 + \beta I_2$ where $0 \leq \beta \leq 1$. In the present case, the experimental data was found to be acceptably fitted by the hyperelastic model using $\beta = 1.$. The constitutive model for the peel arm material is fitted, using least-squares fitting, to the average of the tensile test data shown in Fig. 29. From the calibration procedure, the locking stretch $\lambda_m = 5.28$, the interaction parameter $a = 0.53$ and the shear modulus $\mu = 16.8$ MPa were identified. The calibrated model response is shown together with the experimental data in Fig. 29.

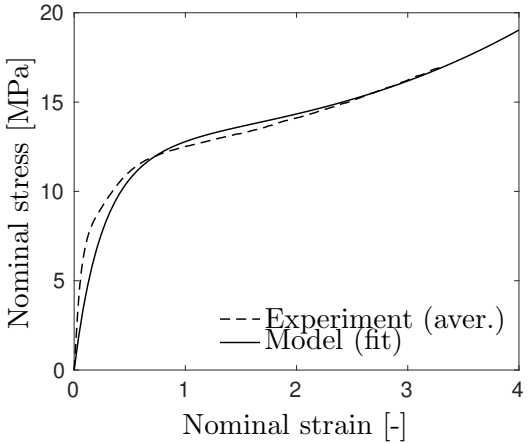

Figure 29: Uniaxial tensile response of the Van der Waals hyperelastic model (solid line), fitted to the averaged tensile test data from Fig. 14

The interface is modeled as a cohesive surface. A total of 2, 24 and 108 elements are used through the thickness, across the width and along the wheel perimeter, respectively. The aluminum foil and paperboard are assumed to be rigidly bonded to the wheel and are not explicitly modeled, but only represented as a rigid surface with an offset in the

radial position. The parameters of the calibrated cohesive zone were a fracture energy G_c = 210 J/m^2 and interface strength t_0 = 7.5 MPa. The interface stiffness was set to K = 10^{13} Pa/m. Using eq. (55) with E_3 = 100 MPa, t = 20 μm, and α = 2. Turon et al. [89] recommended a factor of around 50. However, it is emphazised that eq. (55) was derived for an orthotropic peel arm material. Moreover, by the time peeling initiates, the stiffness of the peel arm material will be lower due to the strain in the peel arm, cf. Fig. 14. Hence, it can be assumed that excessive compliance of the interface is not a problem. Assuming an initial stiffness E = 100 MPa for the peel arm material, the cohesive zone length is between 78.5 μm and 374 μm according to eq. (57), depending on the value used for M. Compared to the element dimensions used for modeling, this length is spanned by a sufficient number of elements.

An *in-situ* test of Material 1 is used for model verification. The force-displacement curve and the geometry of the peel arm (curvature and peel arm thinning) are matched against the experimental observations, as shown in Fig. 30.

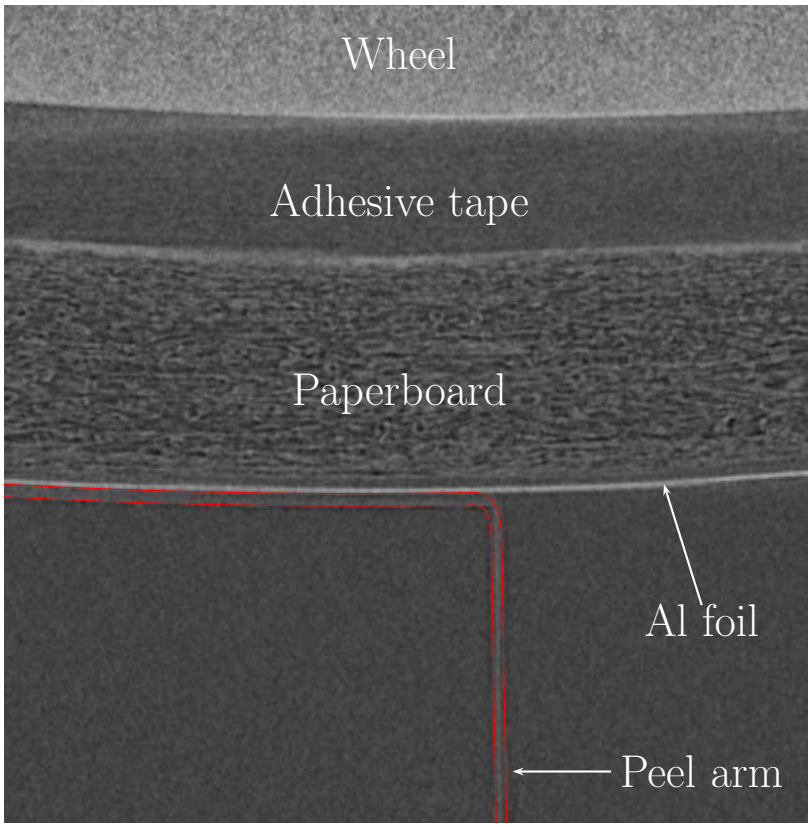

Figure 30: Side view of the peel test. The red lines represent the simulated peel arm geometry, overlaid on top of an experimental X-ray image.

It is seen in experiments of the first material that the delamination front is curved, cf. Fig. 17. This behavior can be reproduced with the numerical model, with the interface being damaged and failing at the edges earlier than in the middle, as shown in Fig. 31.

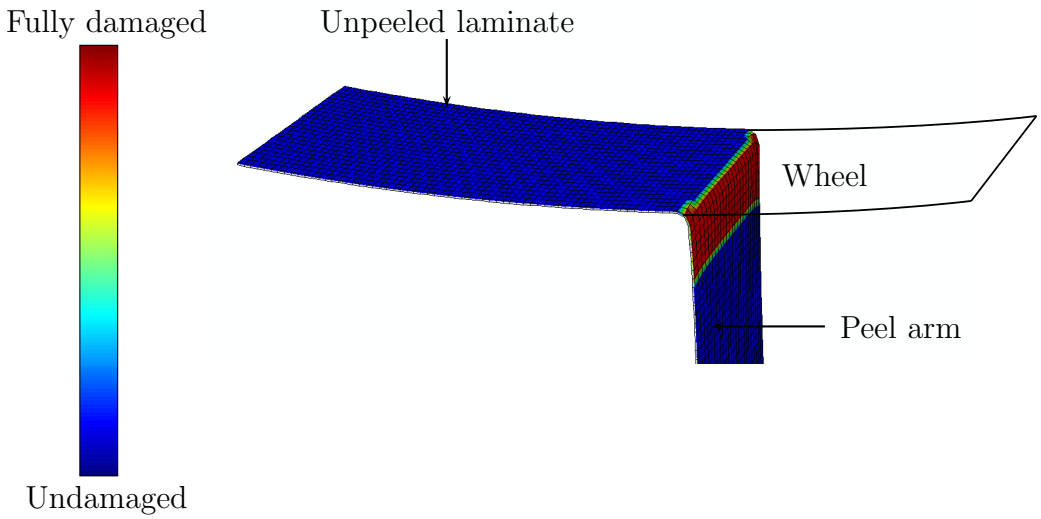

Figure 31: View of the peel front. The peel arm is pulled downwards. The colors indicate the damage in the cohesive zone, with red elements having failed and blue or green elements having a lower degree of damage.

10 Conclusions

Adhesion has been studied extensively for the past century. This collective work has resulted in a number of theories on adhesion and decohesion. A distinction can be made between fundamental and practical adhesion, where the field of solid mechanics is mainly concerned with practical adhesion, i.e. what it is that causes surfaces to separate and identification of the forces, energies etc. required to do so. The view has shifted in recent years from one of mutual exclusivity to one of complementarity, meaning that a grand unified theory on adhesion is no longer the central quest, but rather a patchwork of complementary theories.

Peel testing has previously been studied with other *in-situ* methods, such as scanning electron microscopy (SEM) [64, 65, 99], transmission electron microscopy [63] and optical microscopy [71, 97, 99], but the present approach with X-ray tomography appears new. A main motivation for using tomography is to gain 3D information about the peeling process, not provided other methods. While X-ray tomography does not have the highest resolution of the available imaging methods, it enables a complementary insight into 3D phenomena related to adhesion and can be used together with other methods. For example, using *in-situ* tomography, a region of interest can be identified which can then be studied at higher resolution with SEM. *In-situ* X-ray tomography also generates the 3D displacement field

necessary to use Digital Volume Correlation. Digital Volume Correlation has increased in use in recent years and steps have been taken to increase efficiency by using GPUs rather than CPUs [101]. The correlation for volumes with cracks has also been improved by introducing a Heaviside function in the kinematical transformation [92].

Even though cohesive zone models are widely used, there are considerable issues related to many of the models available in commercial simulation softwares. A number of the frequently used models are not thermodynamically consistent, or consistent only in special cases. In recent years, more focus than previously has been placed on developing thermodynamically consistent cohesive laws, based on potentials and on Helmholtz free energy functions utilizing history-dependent variables. Models such as the PPR model are thermodynamically consistent for loading, but not for general unloading, unless properly modified. Exponential models like the Xu-Needleman model require improvements to fulfill the laws of thermodynamics. For a peel test between 0 and 90°, it has been argued that a mixed-mode analysis is not usually called for [49, 62]. Still, a future analysis of decohesion mechanisms in packaging materials should include a mixed-mode analysis and a complex loading history during e.g. creasing and folding. For this reason, it is important that the unloading/reloading behavior is described in a physically relevant manner.

In the present work, the adhesion between the layers in a packaging material laminate has been studied with a novel *in-situ* method. The combination of peel testing with X-ray tomography allows adhesion phenomena and mechanisms that are not apparent from macroscopic testing to be investigated in great detail. It is, for example, found that the delamination does not necessarily propagate in a homogeneous manner along the width of the sample, but can initiate earlier at the edges than at the peel arm center. The reason for this is thought to be the transverse contraction of the peel arm as well as edge effects and local damage caused by sample cutting. It is also seen that peel arms composed of two layers may split. The reasons for this are not entirely clear, but may be related to artifacts from the sample preparation. In the test shown in Fig. 19, the peel arm starts to split during testing. However, it is also possible to involuntarily split the peel arm during sample preparation, so that a thin layer of adhesive on the aluminum foil remains stuck. Using a synchrotron beamline for *in-situ* X-ray tomography shows great improvements in resolution, providing further data for analysis.

The elimination of the paperboard from the laminate presented additional challenges in the testing procedure. For the materials without paperboard or with thinner paperboard than Material 1, it appears that the adhesion to the tape is a potential issue when performing peel tests. This is also evident in that the displacements are lower, 1.5 mm compared to 5 mm for Material 1. One way to reduce this effect is to place the laminate and tape under pressure for a few days. This should both increase the areas in contact and allow the adhesion between the tape and laminate to cure to achieve a greater strength. A recommended aging time from many tape manufacturers is three days. Even with these efforts, however, issues related to weak adhesion often remain. Ensuring adhesion to the tape proves important, which is usually not a major concern when the structure contains paperboard.

When the peel arm is filled with 5% $CaCO_3$, the peel front appears much more rounded than for both of the other types of materials (Materials 1 and 2). Although the addition

of a filler does not seem to alter the tensile properties of the investigated polymers to a significant extent, it is possible that the adhesive properties are altered. It is also clear that the sample preparation is important when it comes to measuring adhesion. Some phenomena, like edge lift-off, may be due to the way the samples are cut and can be somewhat alleviated by considering alternative cutting methods.

For certain material combinations, fibrillation or crazing can be observed between the adherends, e.g. when a rubbery material is attached to a metal [65, 97, 99] or a polymer to a polymer [76]. This is thought to be due to localized stretching near the peeling zone. In the current work, no such effect is seen. This seems to indicate that a purely adhesive fracture happens. This is also confirmed by the fact that no evidence is found of cracks spreading into the substrate or into peel arm. The exception is the cohesive fracture of the peel arm observed in some cases when the peel arm comprises two similar polymer layers. This phenomenon needs to be studied further, for example by complementary SEM scans.

References

[1] G. Alfano and M. A. Crisfield. Finite element interface models for the delamination analysis of laminated composites: mechanical and computational issues. *International journal for numerical methods in engineering*, 50(7):1701–1736, 2001.

[2] D. Álvarez, B.R.K. Blackman, F.J. Guild, and A.J. Kinloch. Mode i fracture in adhesively-bonded joints: A mesh-size independent modelling approach using cohesive elements. *Engineering Fracture Mechanics*, 115:73–95, 2014.

[3] H.E. Bair, S. Matsuoka, R.G. Vadimsky, and T.T. Wang. Consideration of energy dissipation for the strength of adhesive joints. *The Journal of Adhesion*, 3(2):89–102, 1971.

[4] B.L.V. Bak, E. Lindgaard, and E. Lund. Analysis of the integration of cohesive elements in regard to utilization of coarse mesh in laminated composite materials. *International Journal for Numerical Methods in Engineering*, 99(8):566–586, 2014.

[5] G Bao and Z Suo. Remarks on crack-bridging concepts. *Applied Mechanics Reviews*, 45(8):355–366, 1992.

[6] G.I. Barenblatt. Equilibrium cracks formed during brittle fracture rectilinear cracks in plane plates. *Journal of Applied Mathematics and Mechanics*, 23(4):1009–1029, 1959.

[7] G.I Barenblatt. The mathematical theory of equilibrium cracks in brittle fracture. In *Advances in applied mechanics*, volume 7, pages 55–129. Elsevier, 1962.

[8] B.K. Bay. Methods and applications of digital volume correlation. *The Journal of Strain Analysis for Engineering Design*, 43(8):745–760, 2008.

[9] B.K. Bay, T.S. Smith, D.P. Fyhrie, and M. Saad. Digital volume correlation: three-dimensional strain mapping using x-ray tomography. *Experimental Mechanics*, 39(3):217–226, 1999.

[10] L. Benyahia, C. Verdier, and J.M. Piau. The mechanisms of peeling of uncross-linked pressure sensitive adhesives. *The Journal of Adhesion*, 62(1-4):45–73, 1997.

[11] M.L. Benzeggagh and M.J.C.S. Kenane. Measurement of mixed-mode delamination fracture toughness of unidirectional glass/epoxy composites with mixed-mode bending apparatus. *Composites Science and Technology*, 56(4):439–449, 1996.

[12] J.J. Bikerman. The science of adhesive joints. Technical report, Academic Press,, 1961.

[13] B.R.K. Blackman, H. Hadavinia, A.J. Kinloch, and J.G. Williams. The use of a cohesive zone model to study the fracture of fibre composites and adhesively-bonded joints. *International Journal of Fracture*, 119(1):25–46, 2003.

[14] R.A. Brooks and G. Di Chiro. Beam hardening in x-ray reconstructive tomography. *Physics in medicine & biology*, 21(3):390, 1976.

[15] H.A. Bruck, S.R. McNeill, M.A. Sutton, and W.H. Peters. Digital image correlation using newton-raphson method of partial differential correction. *Experimental mechanics*, 29(3):261–267, 1989.

[16] P.P. Camanho, C.G. Davila, and M.F. De Moura. Numerical simulation of mixed-mode progressive delamination in composite materials. *Journal of composite materials*, 37(16):1415–1438, 2003.

[17] B. Chen, D.A. Dillard, J.G. Dillard, and R.L. Clark. Crack path selection in adhesively bonded joints: the roles of external loads and speciment geometry. *International journal of fracture*, 114(2):167–190, 2002.

[18] H. Chen, X. Feng, Y. Huang, Y. Huang, and J.A. Rogers. Experiments and viscoelastic analysis of peel test with patterned strips for applications to transfer printing. *Journal of the Mechanics and Physics of Solids*, 61(8):1737–1752, 2013.

[19] T.C. Chu, W.F. Ranson, and M.A. Sutton. Applications of digital-image-correlation techniques to experimental mechanics. *Experimental mechanics*, 25(3):232–244, 1985.

[20] S. Cooreman, D. Lecompte, H. Sol, J. Vantomme, and D. Debruyne. Identification of mechanical material behavior through inverse modeling and dic. *Experimental Mechanics*, 48(4):421–433, 2008.

[21] L.F.M. Da Silva, A. Öchsner, and R.D. Adams. *Handbook of adhesion technology*. Springer Science & Business Media, 2011.

[22] L. Daudeville, O. Allix, and P. Ladeveze. Delamination analysis by damage mechanics: some applications. *Composites Engineering*, 5(1):17–24, 1995.

[23] B.V. Derjaguin and V.P. Smilga. Adhesion: fundamentals and practice. *London: McLaren*, 1969.

[24] B.V. Deryagin, N.A. Krotova, and V.P. Smilga. Adhesion of solids, 1978. Engl. Ed. Translated by RK Johnson.

[25] B.V. Deryaguin, N.A. Krotova, V.V. Karassev, Y.M. Kirillova, and I.N. Aleinikova. Electrical phenomena accompanying the formation of new surfaces, and their role in adhesion and cohesion. In *Proceedings of the 2nd International Congress of Surface Activity*, volume 3, page 417, 1957.

[26] R. Dimitri, M. Trullo, G. Zavarise, and L. De Lorenzis. A consistency assessment of coupled cohesive zone models for mixed-mode debonding problems. *Frattura ed Integrità Strutturale*, 8(29):266–283, 2014.

[27] J. Du, D.D. Lindeman, and D.J. Yarusso. Modeling the peel performance of pressure-sensitive adhesives. *The Journal of Adhesion*, 80(7):601–612, 2004.

[28] D.S. Dugdale. Yielding of steel sheets containing slits. *Journal of the Mechanics and Physics of Solids*, 8(2):100–104, 1960.

[29] V.A. Eremeyev and K. Naumenko. A relationship between effective work of adhesion and peel force for thin hyperelastic films undergoing large deformation. *Journal of the Mechanics and Physics of Solids*, 69:24–26, 2015.

[30] N. Ersoy, S. Ahmadvashaghbash, M. Engul, and F. Oz. A comparative numerical study aiming to reduce computation cost for mode-i delamination simulations. 18th European Conference on Composite Materials, Athens, Greece, 2018.

[31] M.L. Falk, A. Needleman, and J.R. Rice. A critical evaluation of cohesive zone models of dynamic fracture. In *Proceedings of the 5th European mechanics of materials conference on scale transitions from atomistics to continuum plasticity*, pages 43–50, 2001.

[32] T. Gajewski and T. Garbowski. Calibration of concrete parameters based on digital image correlation and inverse analysis. *Archives of Civil and Mechanical Engineering*, 14(1):170–180, 2014.

[33] J.L. Gardon. Treatise on adhesion and adhesives. *Arnold, London*, 1:320, 1967.

[34] A.N. Gent and J. Schultz. Effect of wetting liquids on the strength of adhesion of viscoelastic material. *The Journal of Adhesion*, 3(4):281–294, 1972.

[35] A. Germaneau, P. Doumalin, and J.C. Dupré. Full 3d measurement of strain field by scattered light for analysis of structures. *Experimental mechanics*, 47(4):523–532, 2007.

[36] R.J. Good. Theory of "cohesive" vs "adhesive" separation in an adhering system. *The Journal of Adhesion*, 4(2):133–154, 1972.

[37] V.K. Goyal. *Analytical modeling of the mechanics of nucleation and growth of cracks*. PhD thesis, Virginia Polytechnic Institute and State University, 2002.

[38] P.W. Harper and S.R. Hallett. Cohesive zone length in numerical simulations of composite delamination. *Engineering Fracture Mechanics*, 75(16):4774–4792, 2008.

[39] A. Hillerborg, M. Modéer, and P.-E. Petersson. Analysis of crack formation and crack growth in concrete by means of fracture mechanics and finite elements. *Cement and concrete research*, 6(6):773–781, 1976.

[40] P.J. Hine, S.E. Muddarris, and D.E. Packham. Surface pretreatment of zinc and its adhesion to epoxy resins. *The Journal of Adhesion*, 17(3):207–229, 1984.

[41] J.L. Högberg. Mixed mode cohesive law. *International journal of Fracture*, 141(3-4):549–559, 2006.

[42] C.Y. Hui, A. Jagota, S.J. Bennison, and J.D. Londono. Crack blunting and the strength of soft elastic solids. In *Proceedings of the Royal Society of London A: Mathematical, Physical and Engineering Sciences*, volume 459, pages 1489–1516. The Royal Society, 2003.

[43] J.R. Huntsberger. Treatise on adhesion and adhesives. *Arnold, London*, 1:21, 1967.

[44] G.R. Irwin. Analysis of stresses and strains near the end of a crack traversing a plate. *Journal of Applied Mechanics*, 1957.

[45] G.R. Irwin. Plastic zone near a crack and fracture toughness. Proceedings of the 7th Sagamore Conference, p. IV-63, 1960.

[46] Z.L. Kahn-Jetter and T.C. Chu. Three-dimensional displacement measurements using digital image correlation and photogrammic analysis. *Experimental Mechanics*, 30(1):10–16, 1990.

[47] V.M. Karbhari and M. Engineer. Investigation of bond between concrete and composites: use of a peel test. *Journal of Reinforced Plastics and Composites*, 15(2):208–227, 1996.

[48] K. Kendall. Thin-film peeling - the elastic term. *Journal of Physics D: Applied Physics*, 8:1449–1452, 1975.

[49] A.J. Kinloch, C.C. Lau, and J.G. Williams. The peeling of flexible laminates. *International Journal of Fracture*, 66:45–70, 1994.

[50] S.R. Leadley and J.F. Watts. The use of monochromated xps to evaluate acid-base interactions at the pmma/oxidised metal interface. *The Journal of Adhesion*, 60(1-4):175–196, 1997.

[51] S. Li, J. Wang, and M.D. Thouless. The effects of shear on delamination of beam-like geometries. *Journal of the Mechanics and Physics of Solids*, 52:193–214, 2004.

[52] G. Marin and C. Derail. Rheology and adherence of pressure-sensitive adhesives. *The Journal of Adhesion*, 82(5):469–485, 2006.

[53] F. Mathieu, F. Hild, and S. Roux. Identification of a crack propagation law by digital image correlation. *International Journal of Fatigue*, 36(1):146–154, 2012.

[54] D. Maugis. *Contact, Adhesion and Rupture of Elastic Solids*, volume 130. Springer Science & Business Media, 2000.

[55] J.W. McBain and D.G. Hopkins. On adhesives and adhesive action. *The Journal of Physical Chemistry*, 29(2):188–204, 1925.

[56] J.P McGarry, É.Ó. Máirtín, G. Parry, and G.E. Beltz. Potential-based and non-potential-based cohesive zone formulations under mixed-mode separation and over-closure. part i: Theoretical analysis. *Journal of the Mechanics and Physics of Solids*, 63:336–362, 2014.

[57] J.C. Mergel, R.A. Sauer, and A. Saxena. Computational optimization of adhesive microstructures based on a nonlinear beam formulation. *Structural and Multidisciplinary Optimization*, 50(6):1001–1017, 2014.

[58] N. Moës and T. Belytschko. Extended finite element method for cohesive crack growth. *Engineering fracture mechanics*, 69(7):813–833, 2002.

[59] I.K. Mohammed, M.N. Charalambides, and A.J. Kinloch. Modelling the interfacial peeling of pressure-sensitive adhesives. *Journal of Non-Newtonian Fluid Mechanics*, 222:141–150, 2015.

[60] I.K. Mohammed, A.J. Kinloch, and M.N. Charalambides. Modelling the peeling behavior of soft adhesives. In *Procedia Structural Integrity*, volume 2, pages 326–333. Proceedings of the 21st European Conference on Fracture, ECF21, Catania, Italy, June 2016.

[61] J. Mosler and I. Scheider. A thermodynamically and variationally consistent class of damage-type cohesive models. *Journal of the Mechanics and Physics of Solids*, 59(8):1647–1668, 2011.

[62] M. Nase, B. Langer, and W. Grellmann. Fracture mechanics on polyethylene/polybutene-1 peel films. *Polymer Testing*, 27:1017–1025, 2008.

[63] M. Nase, B. Langer, and W. Grellmann. Fracture mechanics on polyethylene/polybutene-1 peel films. *Polymer Testing*, 27(8):1017–1025, 2008.

[64] M. Nase, A. Zankel, B. Langer, H.J. Baumann, W. Grellmann, and P. Poelt. Investigation of the peel behavior of polyethylene/polybutene-1 peel films using in situ peel tests with environmental scanning electron microscopy. *Polymer*, 49(25):5458–5466, 2008.

[65] J. Neggers, J.P.M. Hoefnagels, O. van der Sluis, O. Sedaghat, and M.G.D. Geers. Analysis of the dissipative mechanisms in metal–elastomer interfaces. *Engineering Fracture Mechanics*, 149:412–424, 2015.

[66] N.S. Ottosen, M. Ristinmaa, and J. Mosler. Fundamental physical principles and cohesive zone models at finite displacements–limitations and possibilities. *International Journal of Solids and Structures*, 53:70–79, 2015.

[67] B. Pan, K. Qian, H. Xie, and A. Asundi. Two-dimensional digital image correlation for in-plane displacement and strain measurement: a review. *Measurement science and technology*, 20(6):062001, 2009.

[68] K. Park and G.H. Paulino. Computational implementation of the ppr potential-based cohesive model in abaqus: Educational perspective. *Engineering fracture mechanics*, 93:239–262, 2012.

[69] K. Park, G.H. Paulino, and J.R. Roesler. A unified potential-based cohesive model of mixed-mode fracture. *Journal of the Mechanics and Physics of Solids*, 57(6):891–908, 2009.

[70] J.P. Parmigiani and M.D. Thouless. The effects of cohesive strength and toughness on mixed-mode delamination of beam-like geometries. *Engineering Fracture Mechanics*, 74(17):2675–2699, 2007.

[71] Z. Peng, C. Wang, L. Chen, and S. Chen. Peeling behavior of a viscoelastic thin-film on a rigid substrate. *International Journal of Solids and Structures*, 51:4596–4603, 2014.

[72] A. Pizzi and K.L. Mittal. *Handbook of Adhesive Technology, Revised and Expanded*. CRC Press, 2003.

[73] X. Qiu, M.E. Plesha, and D.W. Meyer. Stiffness matrix integration rules for contact-friction finite elements. *Computer methods in applied mechanics and engineering*, 93(3):385–399, 1991.

[74] J.R. Rice. *The mechanics of earthquake rupture*. Division of Engineering, Brown University, 1979.

[75] R.S. Rivlin. The effective work of adhesion. *Paint Technology*, 9:215–216, 1944.

[76] V. Ronesi, Y.W. Cheung, A. Hiltner, and E. Baer. Adhesion of ethylene–styrene copolymers to polyethylene in microlayers. *Journal of applied polymer science*, 89(1):153–162, 2003.

[77] L. Salvo, P. Cloetens, E. Maire, S. Zabler, J.J. Blandin, J.Y. Buffière, W. Ludwig, E. Boller, D. Bellet, and C. Josserond. X-ray micro-tomography an attractive characterisation technique in materials science. *Nuclear instruments and methods in physics research section B: Beam interactions with materials and atoms*, 200:273–286, 2003.

[78] R.A. Sauer. The peeling behavior of thin films with finite bending stiffness and the implications on gecko adhesion. *The Journal of Adhesion*, 87(7-8):624–643, 2011.

[79] J.C.J. Schellekens and R. De Borst. On the numerical integration of interface elements. *International Journal for Numerical Methods in Engineering*, 36(1):43–66, 1993.

[80] L.H. Sharpe and H. Schonhorn. Theory gives direction to adhesion work. *Chemical and engineering news*, 41(15):67–68, 1963.

[81] B. Shen and G.H. Paulino. Direct extraction of cohesive fracture properties from digital image correlation: a hybrid inverse technique. *Experimental Mechanics*, 51(2):143–163, 2011.

[82] D.W. Spring, O. Giraldo-Londono, and G.H. Paulino. A study on the thermodynamic consistency of the park–paulino–roesler (ppr) cohesive fracture model. *Mechanics Research Communications*, 78:100–109, 2016.

[83] Z. Suo and J.W. Hutchinson. Interface crack between two elastic layers. *International Journal of Fracture*, 43(1):1–18, 1990.

[84] M.A. Sutton, C. Mingqi, W.H. Peters, Y.J. Chao, and S.R. McNeill. Application of an optimized digital correlation method to planar deformation analysis. *Image and Vision Computing*, 4(3):143–150, 1986.

[85] M.A. Sutton, W.J. Wolters, W.H. Peters, W.F. Ranson, and S.R. McNeill. Determination of displacements using an improved digital correlation method. *Image and vision computing*, 1(3):133–139, 1983.

[86] M.D. Thouless and H.M. Jensen. Elastic fracture mechanics of the peel-test geometry. *The Journal of Adhesion*, 38(3-4):185–197, 1992.

[87] M.D. Thouless and Q.D. Yang. A parametric study of the peel test. *International Journal of Adhesion and Adhesives*, 28:176–184, 2008.

[88] E. Tudisco, E. Andò, R. Cailletaud, and S.A. Hall. Tomowarp2: a local digital volume correlation code. *SoftwareX*, 6:267–270, 2017.

[89] A. Turon, C.G. Dávila, P.P. Camanho, and J. Costa. An engineering solution for mesh size effects in the simulation of delamination using cohesive zone models. *Engineering Fracture Mechanics*, 74:1665–1682, 2007.

[90] V. Tvergaard and J.W. Hutchinson. The relation between crack growth resistance and fracture process parameters in elastic-plastic solids. *Journal of the Mechanics and Physics of Solids*, 40(6):1377–1397, 1992.

[91] V. Tvergaard and J.W. Hutchinson. The influence of plasticity on mixed mode interface toughness. *Journal of the Mechanics and Physics of Solids*, 41(6):1119–1135, 1993.

[92] V. Valle, P. Bokam, A. Germaneau, and S. Hedan. New development of digital volume correlation for the study of fractured materials. *Experimental Mechanics*, 59(1):1–15, 2019.

[93] V. Valle, S. Hedan, P. Cosenza, A.L. Fauchille, and M. Berdjane. Digital image correlation development for the study of materials including multiple crossing cracks. *Experimental Mechanics*, 55(2):379–391, 2015.

[94] V. Valle, L. Laou, I. Léandry, S. Yotte, S. Rossignol, and S. Hedan. Crack analysis in mudbricks under compression using specific development of stereo-digital image correlation. *Experimental Mechanics*, 58(3):475–486, 2018.

[95] M.J. Van den Bosch, P.J.G. Schreurs, and M.G.D. Geers. An improved description of the exponential xu and needleman cohesive zone law for mixed-mode decohesion. *Engineering Fracture Mechanics*, 73(9):1220–1234, 2006.

[96] M.J. Van den Bosch, P.J.G. Schreurs, and M.G.D. Geers. On the development of a 3d cohesive zone element in the presence of large deformations. *Computational mechanics*, 42(2):171–180, 2008.

[97] O. Van Der Sluis, Y.Y. Hsu, P.H.M. Timmermans, M. Gonzalez, and J.P.M. Hoefnagels. Stretching-induced interconnect delamination in stretchable electronic circuits. *Journal of Physics D: Applied Physics*, 44(3):034008, 2010.

[98] H. G. Von Harrach and B.N. Chapman. Charge effects in thin film adhesion. *Thin Solid Films*, 13(1):157–161, 1972.

[99] B.G. Vossen, O. Van Der Sluis, P.J.G. Schreurs, and M.G.D. Geers. High toughness fibrillating metal-elastomer interfaces: on the role of discrete fibrils within the fracture process zone. *Engineering Fracture Mechanics*, 164:93–105, 2016.

[100] W.C. Wake. *Adhesion and the Formulation of Adhesives*. Applied Science Publishers Ltd,Essex, 2 edition, 1982.

[101] T. Wang, Z. Jiang, Q. Kemao, F. Lin, and S.H. Soon. Gpu accelerated digital volume correlation. *Experimental Mechanics*, 56(2):297–309, 2016.

[102] T.T. Wang and H.N. Vazirani. Peel strength and failure mechanisms in oxidized copper-polyethylene lap joints bonded with flexible epoxy. *The Journal of Adhesion*, 4(4):353–364, 1972.

[103] J.A. Williams and J.J. Kauzlarich. Peeling shear and cleavage failure due to tape prestrain. *The journal of Adhesion*, 80(5):433–458, 2004.

[104] J.A. Williams and J.J. Kauzlarich. The influence of peel angle on the mechanics of peeling flexible adherends with arbitrary load–extension characteristics. *Tribology International*, 38(11-12):951–958, 2005.

[105] R.P. Wool. *Polymer interfaces: structure and strength*. Hanser, 1995.

[106] R.P. Wool. Diffusion and autohesion. In *Adhesion Science and Engineering*, pages 351–401. Elsevier, 2002.

[107] R.P. Wool. Polymer diffusion: reptation and interdigitation. *Handbook of Adhesion, 2nd ed. John Wiley & Sons, Bath, UK*, pages 341–344, 2005.

[108] X.P. Xu and A. Needleman. Numerical simulations of fast crack growth in brittle solids. *Journal of the Mechanics and Physics of Solids*, 42(9):1397–1434, 1994.

[109] Q.D. Yang and M.D. Thouless. Mixed-mode fracture analyses of plastically-deforming adhesive joints. *International Journal of Fracture*, 110(2):175–187, 2001.

[110] H. Yuan and X. Li. Effects of the cohesive law on ductile crack propagation simulation by using cohesive zone models. *Engineering Fracture Mechanics*, 126:1–11, 2014.

[111] Z.J. Zhang and G.H. Paulino. Cohesive zone modeling of dynamic failure in homogeneous and functionally graded materials. *International journal of plasticity*, 21(6):1195–1254, 2005.

[112] M. Zhou, Y. Tian, N. Pesika, H. Zeng, J. Wan, Y. Meng, and S. Wen. The extended peel zone model: effect of peeling velocity. *The Journal of Adhesion*, 87(11):1045–1058, 2011.

[113] Z. Zou, S.R. Reid, S. Li, and P.D. Soden. Modelling interlaminar and intralaminar damage in filament-wound pipes under quasi-static indentation. *Journal of composite materials*, 36(4):477–499, 2002.

Paper A

S. Pettersson, J. Engqvist, S. Hall, N. Toft and H. Hallberg

Peel testing of a packaging material laminate studied by in-situ X-ray tomography and cohesive zone modeling

Submitted for publication in Journal of Adhesion and Adhesives.

Peel testing of a packaging material laminate studied by in-situ X-ray tomography and cohesive zone modeling

Simon Pettersson[†], Jonas Engqvist[†], Stephen Hall[†],
Nils Toft[‡], Håkan Hallberg[*†]

[†] Division of Solid Mechanics, Lund University, P.O. Box 118, SE-221 00 Lund, Sweden

[‡] Tetra Pak Packaging Solutions AB, Ruben Rausings gata, SE-221 86 Lund, Sweden

Abstract

In the present work, peel testing is performed on a packaging material laminate in order to investigate the mechanisms that are involved in the adhesive fracture and that provide the adhesive properties, as measured by standard macroscopic tests. Using a peel test load rig, specially designed for the present purposes, peel tests are performed *in-situ* in a laboratory X-ray tomograph. The peel test results are analyzed using a combination of theoretical models for the adhesive fracture and 3D finite element simulations based on a cohesive zone model approach. Complementary experiments are performed to characterize the properties of the peel arm material. Relaxation of the material is found to occur during image acquisition in the *in-situ* tests. Despite this, it is possible to obtain 3D reconstructions with good quality during peeling. Peel test properties like root rotation angle and peel arm thinning are quantified. In the present 90° peel tests, it is found that the delamination progresses in an inhomogeneous manner, with the edges delaminating before the center. A number of issues and mechanisms during the peel test are identified. As an example, the peel arm itself can sometimes split, leaving residues of adhesive on the substrate surface. Such phenomena indicate the ambiguities involved in assessing adhesion properties from standard macroscopic force-displacement measurements, without accounting for the mechanisms involved on finer length scales.

Keywords: Peel test, Delamination, Cohesive zone, Packaging materials, X-ray tomography

1 Introduction

Packages for food and dairy products, for example, commonly comprise multiple layers of different materials that together form a laminate, as illustrated in Fig. 1. Each layer serves a different purpose in preserving and protecting the package content and in providing package rigidity. During manufacturing and handling, the packaging material is

*Corresponding author. Mail: hakan.hallberg@solid.lth.se. Tel.: +46 46 222 90 92.

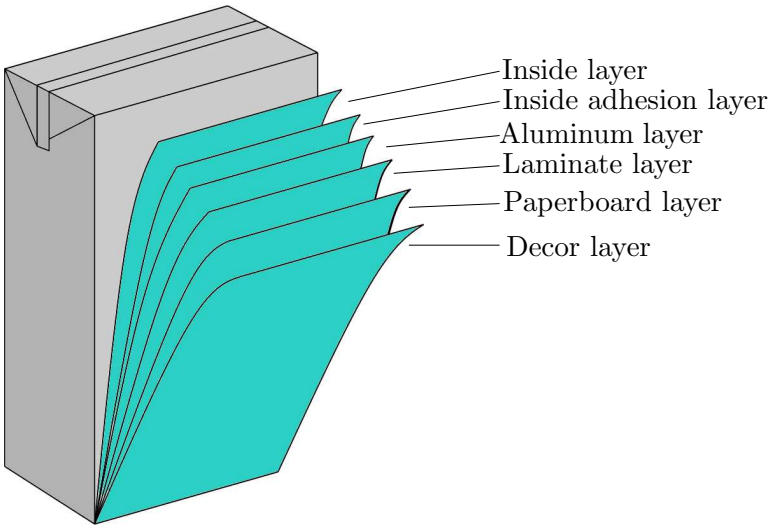

Figure 1: Schematic illustration of a typical packaging material laminate, comprising several layers of different materials such as polymer films, adhesive layers, paperboard and aluminum foil.

subject to conditions that may cause unwanted delamination between the layers. This can decrease the barrier properties of the package and result in a reduced product shelf-life and overall unsatisfactory package performance. In contrast, controlled delamination can also be required in some cases, for example during creasing and folding of the packaging material laminate during manufacturing or in different built-in mechanisms for opening of the package. Being such a critical aspect in the use and performance of packaging material laminates, understanding and controlling adhesion between the laminate layers is of pivotal importance. There is a clear need for an increased understanding of the fracture mechanisms that are involved in the delamination and for an improved ability to predict the adhesion properties of different packaging material laminates and under different loading conditions. In this study, a combination of experimental investigations and numerical simulations is employed to study the fracture zone during delamination in a typical packaging material laminate.

Peel testing is a commonly used approach to assess the adhesion properties in laminate materials and many different types of peel tests have been developed for different applications and for investigating different delamination mechanisms [1, 6, 8]. Most standardized peel test methods are, however, based on macroscopic measurements and provide little insight into the adhesion mechanisms that are active on the microscale. A peel test device has been developed in the present work that is specially adapted to the peeling of very thin polymer films, as often used in packaging material laminates. The test device is designed such that it permits *in-situ* testing in a laboratory X-ray tomograph system or at larger synchrotron facilities. Peel testing of thin polymer films with *in-situ* imaging has been performed previously using digital cameras, for example, in the T-peel experiments in [10, 11, 16]. However, the use of X-ray tomography for *in-situ* imaging of peel tests appears to be an unexplored approach, but one that could provide additional insights into the peeling process by adding 3D understanding of the process as opposed to just boundary force and displacement measurements or observation of the edges which will be

subject to edge-effects. A first aim of the present study is to provide a proof-of-concept study of the specially designed peel test rig, in addition to investigating the processes of peeling in 3D to shed new light on the mechanisms involved in the adhesive fracture. To permit further analyses of the experimental results, a 3D finite element model of the peel test setup is established using a cohesive zone representation of the adhesive fracture region. Complementary tensile testing of the peel arm material is performed to permit calibration of the constitutive model that is used in the numerical simulations.

This paper is structured with the experimental work presented first in Section 2, comprising a presentation of the newly developed peel test load rig as well as a discussion on the *in-situ* peel testing itself. In the same section, the characterization of the peel arm material is also discussed. The finite element simulation model is detailed in Section 3 along with a discussion on the cohesive zone model of the adhesive fracture path and on the modeling and model calibration related to the thin polymer film constituting the peel arm. A discussion is provided in Section 4, in which the experimental results are analyzed and confronted with the aforementioned simulation results. Based on an energy balance, an analytic general fracture energy model is established that contains the classical Rivlin and Kendall formulations as special cases. In the present formulation, however, non-classical finite stretching of the peel arm, modeled as hyperelastic, is also considered. The applicability of such an analytical approach in the present case is discussed. Finally, some concluding remarks close the paper in Section 5.

2 Experimental work

As illustrated in Fig. 1, a packaging material laminate usually comprises a number of layers of different materials. The laminate's adhesion properties can be quite cumbersome to assess when performing peel testing on a complete packaging material laminate in which several interfaces are present between the layers and where also damage processes, not least in the fiber structure of the paperboard, can be expected to influence the test results. To facilitate the present investigations, a specially designed laminate was manufactured at Tetra Pak by extrusion. This custom laminate consists of a paperboard substrate about 450 μm thick, a thin adhesive layer, aluminum foil of 6.3 μm thickness, an ethylene acrylic acid copolymer (EAA) adhesive layer of 4 μm thickness and a 13 μm thick metallocene-catalyzed polyethylene (mPE) film, as shown conceptually in Fig. 2. The adhesive layer and the mPE film have nearly identical mechanical properties, and together formed the peel arm in the tests. The nominal thickness of the combined mPE+EAA peel arm is 17 μm.

To characterize mechanical properties, standard tensile testing was performed on standalone films of the peel arm material. A custom built load rig was used to perform peel testing of the laminate material under *in-situ* peeling in a laboratory X-ray tomograph as well as in complementary *ex-situ* peel tests. The different experiments are further discussed in the following subsections.

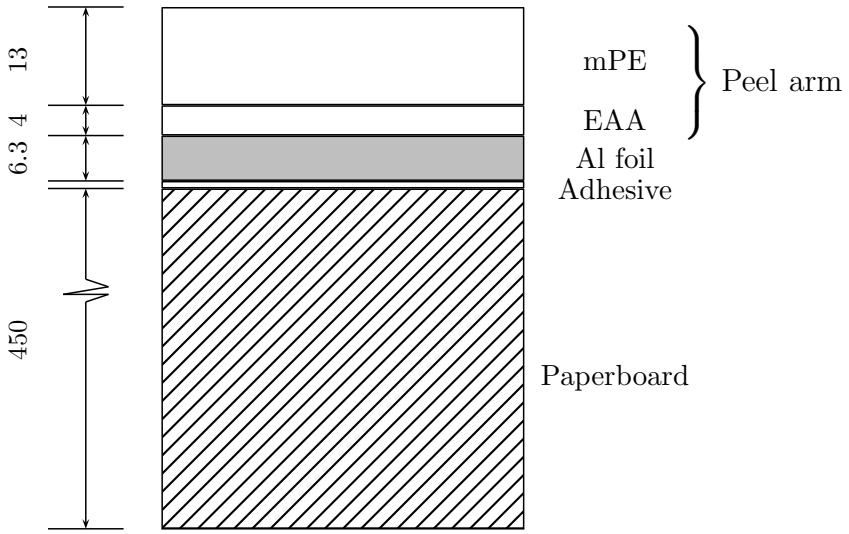

Figure 2: Sketch illustrating the different layers in the studied laminate material, with dimensions in μm (not drawn to scale).

2.1 Tensile testing of the peel arm material

A number of tensile test specimens were produced from the peel arm material by chemically removing the polymer film from the rest of the laminate. This was achieved by separating as much of the aluminum foil from the paperboard as possible by hand, then placing the foil and peel arm material in a bath of acetic acid. The acetic acid had a concentration of 10 %, which was concentrated enough to weaken the adhesion, but not to damage the polymer. The material was held in this bath for one week, after which the adhesion between the peel arm and aluminum was weak enough that they could be separated by hand without any tangible force. The polymer films were then dried at 23° C and 50% relative humidity in a climate controlled environment. Dog bone shaped specimens were punched out from the free-standing polymer film and tested in a tensile load frame. The average thickness of the peel arm material was 20 μm, somewhat more than the nominal 17 μm of the mPE+EAA used in the peel test experiments.. The tensile tests were performed at four different deformation rates: 10 mm/min, 50 mm/min, 100 mm/min and 500 mm/min. The results from the tensile tests are shown in Fig. 3. A total of 6-9 tests were performed at each deformation rate and the error bars in Fig. 3 indicate the spread in the test data. Despite the quite wide span of deformation rates, it appears that the rate dependence is negligible and the peel arm material can be treated as rate independent for the remainder of the present study.

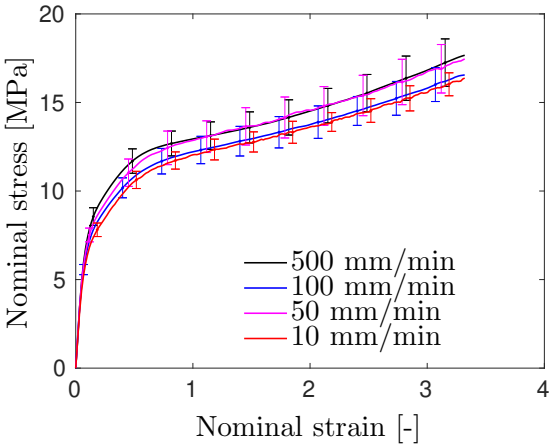

Figure 3: Results from tensile testing of the peel arm material at different deformation rates. The rate dependence is found to be negligible.

2.2 Peel test experiments

A peel test approach similar to a standard "German wheel" setup, for example defined by the DIN 53357 standard, is employed. The present setup is, however, miniaturized and designed to also permit *in-situ* testing with X-ray imaging. As illustrated in Fig. 4a, for each test a strip of the laminate to be tested is attached to an aluminum wheel, of diameter $2R = 20$ mm and thickness 3 mm, using double-sided adhesive tape. The tape was Tesa 64620, with a polypropylene backing, a thickness of 185 μm and a synthetic rubber adhesive. The laminate samples were cut into 2 mm wide strips using a CNC cutter and were mounted with the paperboard side facing the aluminum wheel. The narrow (2 mm) width of the samples was chosen to facilitate a higher resolution during the tomography acquisition. To mount the test specimen in the load rig, cf. Fig. 4b, a part of the polymer film is manually peeled off to provide an initial peel arm that can be clamped by the grip of the load rig. During testing, the grip is actuated by a piezoelectric motor that pulls the peel arm downwards. Since the center of the wheel is held fixed from translating in space, a 90° peel angle is maintained throughout the test. The setup is convenient for *in-situ* imaging of the peel process, as the peel front remains at approximately the same location in space throughout a test. Further, the small dimensions of the test device allows the X-ray source and detector to be placed very close to the sample and the clear PMMA tube housing allows the X-rays to freely pass through the laminate sample being peeled, cf. Fig. 4b. Note that in Fig. 4b, the source and detector are much further apart than in the actual experiments, to provide a clearer view of the setup. During testing, the displacement is measured by the position sensor, an optical encoder with a displacement resolution of 1.25 μm and an accuracy of ± 3 μm, on the piezoelectric LL06 motor manufactured by PiezoMotor. The peel force is obtained from an LCDF-1KG load cell manufactured by Omega Engineering Inc. The load cell is calibrated to a maximum force of 9.8 N with an accuracy of $\pm 0.15\%$ of full scale output.

The *in-situ* peel tests were performed in a Zeiss Xradia XRM 520 Versa at the 4D Imaging Lab at Lund University, using 80 kV X-rays at 7 W power. As shown in Fig. 4b,

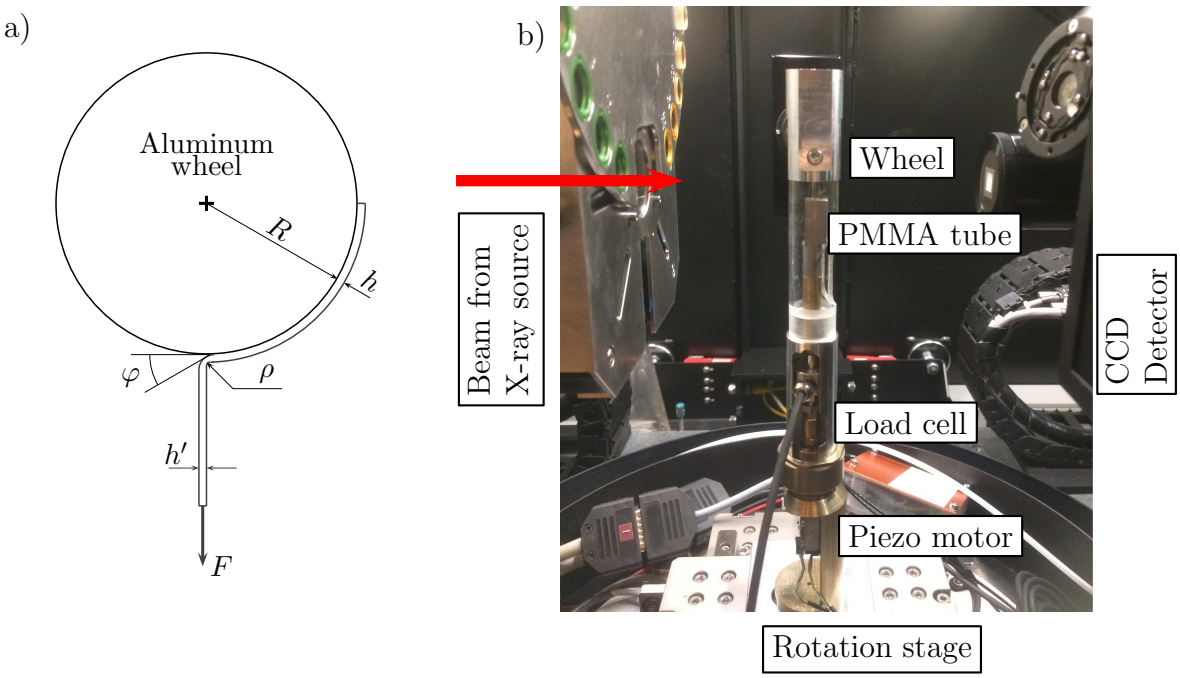

Figure 4: a) Geometrical parameters defining the peel test. The polymer film has a width b (normal to the paper) and a thickness $h \ll b$. The film is attached to a wheel of radius R. The film is peeled of vertically downwards by a peel force F and the peel arm obtains a reduced thickness $h' < h$. At the peel front, the film forms an angle φ with the wheel and the free peel arm has a local radius of curvature ρ. b) The peel test device developed for the present study with main components marked. The X-ray source is to the left, and the CCD detector to the right of the test specimen. Note that during the experiment, the source and detector are brought much closer to the device, to increase resolution. The diameter of the PMMA tube is 20 mm.

the peel test specimen is placed between the X-ray source and the CCD detector. The peel test rig can be freely rotated around its vertical axis, allowing X-ray radiographs to be acquired at different rotation angles. Many such radiographs from a full 360° rotation can then be used for 3D reconstruction to provide a 3D image of the test specimen. During acquisition of each X-ray tomography, the displacement of the peel arm was stopped and held constant. The total acquisition time was about 1h 7 mins during which 1601 images are obtained with an exposure time of 2.5 s. The final 3D images had cubic voxels of dimension 3.2 μm.

During the tomography acquisitions, it was noted that relaxation occurred in the test specimen, as shown by the drops in force seen in Fig. 5a. To investigate the severity of relaxation during image acquisition, continuous peel tests were conducted to provide uninterrupted peel force versus displacement data. For calibration of the numerical simulation model, a test series of 10 continuous peel tests was conducted *ex-situ*, i.e. outside the X-ray tomograph. These results were also compared to the *in-situ* curves. The average of the curves and the standard deviation is shown in Fig. 5b. The average force at the plateau was 0.385 N, with a standard deviation of 0.03-0.06 N. These results are compared with the *in-situ* force-displacement response, with stops for image acquisition, shown in Fig. 5a. It can be noted that the plateau force level appears relatively unaffected by the relaxation during the acquisition. It is emphasized that while Fig. 5a shows data from a single peel test, Fig. 5b shows data averaged from a number of tests. For both the *in-situ* and *ex-situ* tests, the displacement rate was 0.5 mm/min. Pure relaxation tests were also performed by loading peel test specimens and then keeping the displacement fixed. The registered force as function of relaxation time is shown in Fig. 5c. The force was increased to 0.4 N before commencing relaxation and after 1h, the relevant time scale for the scans, the force was below 0.2 N. The relaxation test was run for a longer time than shown in Fig. 5c. Relaxation, although small, was observed also after 60+ hours.

A remedy to reduce the relaxation effects is to increase the acquisition rate, for example by performing the *in-situ* peel tests at a synchrotron X-ray facility. This is part of ongoing work.

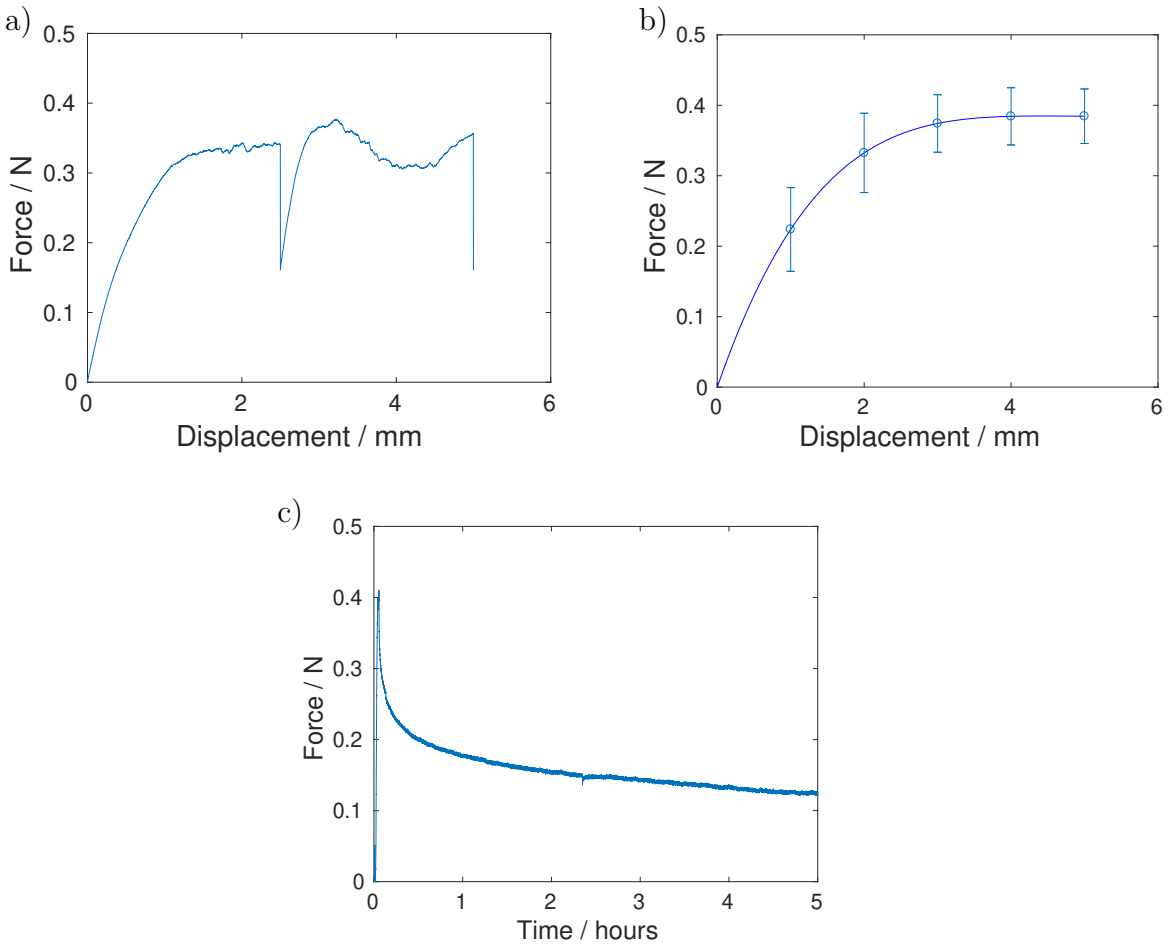

Figure 5: a) Force-displacement curve registered during an *in-situ* peel test. The force drops at approximately 2.5 and 5 mm displacement correspond to the relaxation that takes place in the peel arm and laminate during acquisition of the X-ray image. b) Force-displacement curves registered during continuous peeling. The solid line is an average of 10 tests and the spread in the data is indicated by the error bars. c) Force-time response during a relaxation test in the peel test load rig. The force is first increased to 0.4 N, after which the relaxation test commences.

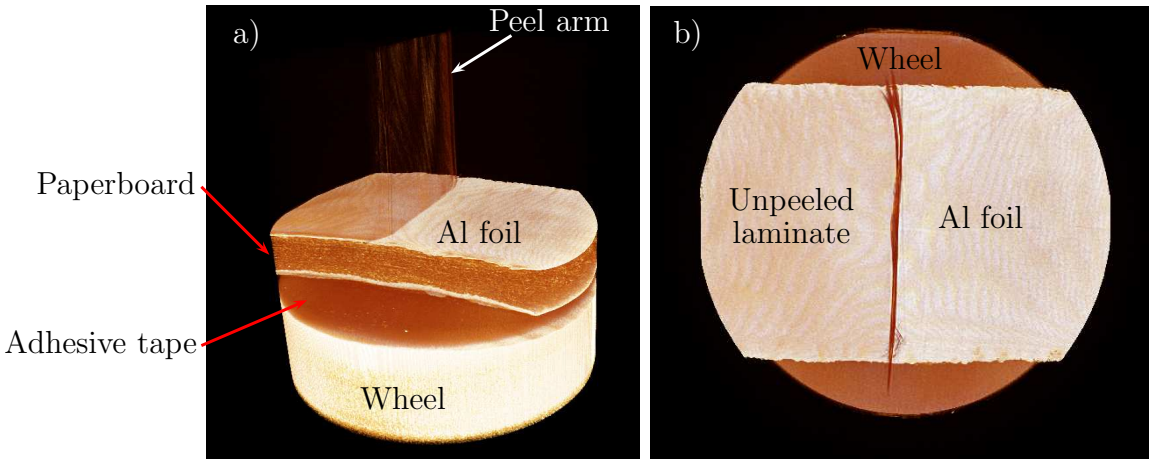

Figure 6: Example images from *in-situ* peel testing using the methods and equipment described in this section. a) Laminate seen from an angle. b) Laminate seen from above, down along the peel arm.

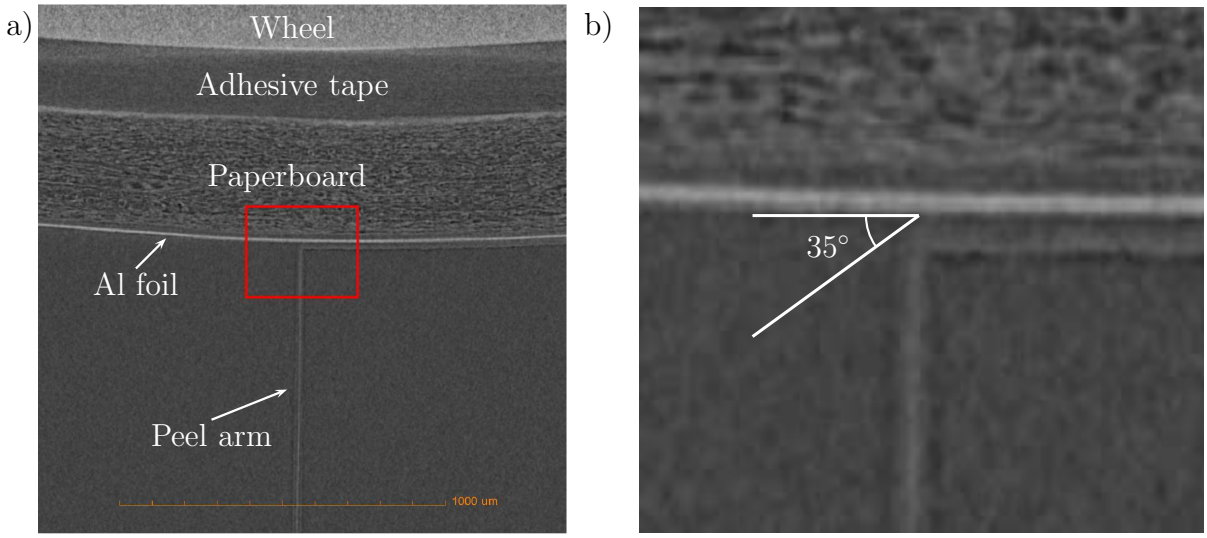

Figure 7: 2D image from the side of in-situ peel test. Same experiment as in Fig. 6. The 2D view is from the middle section. a) Overview. b) Zoom-in of the peel zone, as indicated by the red frame in figure a). An estimate of the opening angle ϕ is indicated in figure b).

The images in Fig. 6 are obtained at 5 mm displacement, cf. Fig. 5a. From the images in Fig. 6, some details about the delamination can be observed. It can be seen that the delamination progresses in the shape of a thumbnail, i.e. the edges of the peel arm delaminate prior to the center region. This appearance is consistent throughout the tests and is mainly due to the transverse contraction of the peel arm and edge effects. Furthermore, most likely, the integrity of the edges will be compromised by local damage and pinching during cutting of the samples. Despite the continuous deformation caused by relaxation during image acquisition, the image in Fig. 7a appears quite sharp, suggesting that the motion was minor.

From the 2D side-view image in Fig. 7a, it can be seen that a nearly right angle is maintained at the peel front, at least when viewed from a distance. Looking at the

zoomed-in image in Fig. 7b, the opening angle φ, cf. Fig. 4a, is estimated to 35°. The zoomed-in image in Fig. 7b corresponds to the region marked by a red box in Fig. 7a. It is also seen that the fracture remains adhesive between the peel arm and the aluminum foil (appearing in white). This is consistent with observations made in other studies, noting that the fracture mechanism can vary from interlaminar (adhesive) to translaminar (cohesive) as the peel angle increases from 90° to 180° [15]. Further, as seen in Fig. 7, the thickness of the stretched peel arm has been reduced to about 15 μm, from the initial thickness of 20 μm. This thinning of the peel arm, as well as the transverse contraction of the peel arm seen in Fig. 6, indicate the substantial peel arm deformation that is involved during the present peel test.

In Fig. 8, it appears that the peel arm separated, which is a phenomenon observed in some of the tests, with strands of adhesive sticking to the substrate. This seems to be due to the peel arm splitting, which may happen since the peel arm is made of two materials (EAA+mPE), cf. Fig. 2. In general, the peel force seems to reach a lower plateau in the tests where the peel arm was split, which would indicate that the mode of failure has been altered. Such observations are of interest as they indicate the uncertainties involved in performing standardized macroscopic peel tests to assess adhesion properties. Depending on the microstructural damage processes, quite different results are obtained. Fig. 6 also reveals a wavy pattern on the interface between the aluminum foil and the peel arm. This is one cause of the peel force oscillations seen in Fig. 5a and can be related to the non-homogeneous adhesion properties reported in [20]. Oscillations of the peel force can also be expected due to a stick-slip behavior, as noted in [4, 18].

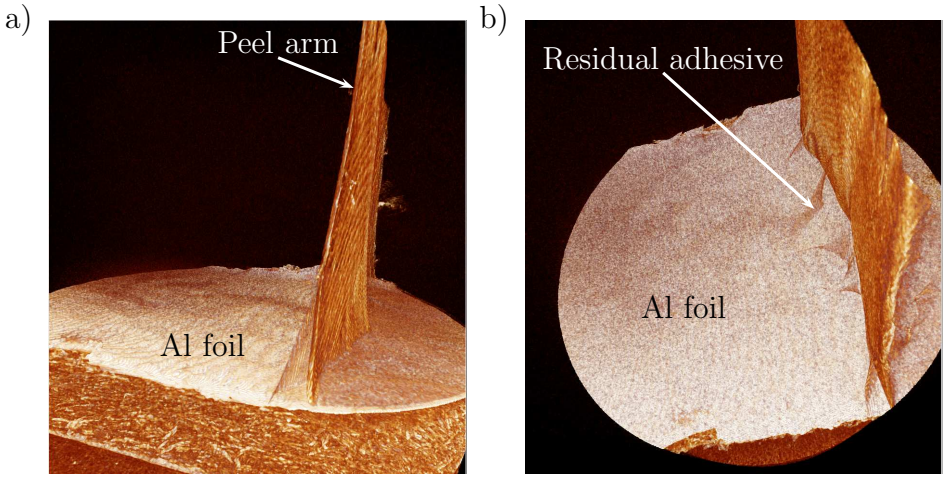

Figure 8: Example images from *in-situ* peel testing a) Laminate seen from the side. b) Peeling seen from above

3 Numerical simulation model

A numerical 3D simulation model is built using the commercial finite element software Abaqus to recreate the peel test experiments. In the model, a sector of the wheel is represented by a rigid analytic surface. The sector is spanned by the angle $\varphi_1 + \varphi_2 = 15°$, as illustrated in Fig. 9a. The cohesive zone is spanned by the angle $\varphi_2 = 10°$. The wheel surface is rigidly connected to the wheel center, at which the translational degrees of

freedom are held fixed. To prevent numerical issues associated with rigid body rotation, a small rotational stiffness, of 10^{-4} Nm/rad is added to the wheel center. The peel arm is discretized using C3D20H 20-node brick elements with a hybrid formulation, to avoid the element locking, which is a likely issue when considering (nearly) incompressible materials. A total of 2, 24 and 108 elements are used through the thickness, across the width and along the wheel perimeter, respectively. The aluminum foil is assumed to be rigidly attached to the wheel, i.e. the aluminum foil and the paperboard are not explicitly described in the model, they are only represented in terms of an offset in the radial position of the peel arm material. The adhesive fracture region between the peel arm and the substrate is modeled using a cohesive surface model. A bi-linear traction-separation law, shown in Fig. 10 is employed. This model is defined by three parameters: the fracture energy G_c, the peak traction t_0 and the separation at full cohesive failure, δ_0. However, due to the bilinear formulation, only two of these parameters need to be calibrated to fully define the traction-separation behavior. In the present case, G_c and t_0 are used for calibration against the experimental results. It can be noted that bilinear traction-separation laws have been used for similar purposes in, for example, [2, 3, 14]. A penalty-based contact condition is prescribed between the peel arm and the wheel to avoid nonphysical penetration of the polymer through the aluminum foil/wheel surface. Peeling is achieved by prescribing a vertical displacement u of the free end of the peel arm, as illustrated by the sequence of pictures in Fig. 9. After a couple of time steps, cf. Fig. 9b, the peel arm attains a 90° angle with respect to the wheel and the actual peel test simulation can commence by prescribing further vertical displacement of the free end of the peel arm, cf. Fig.9c. This method of peel force application is similar to the approach used in the 2D peel test model used in [19].

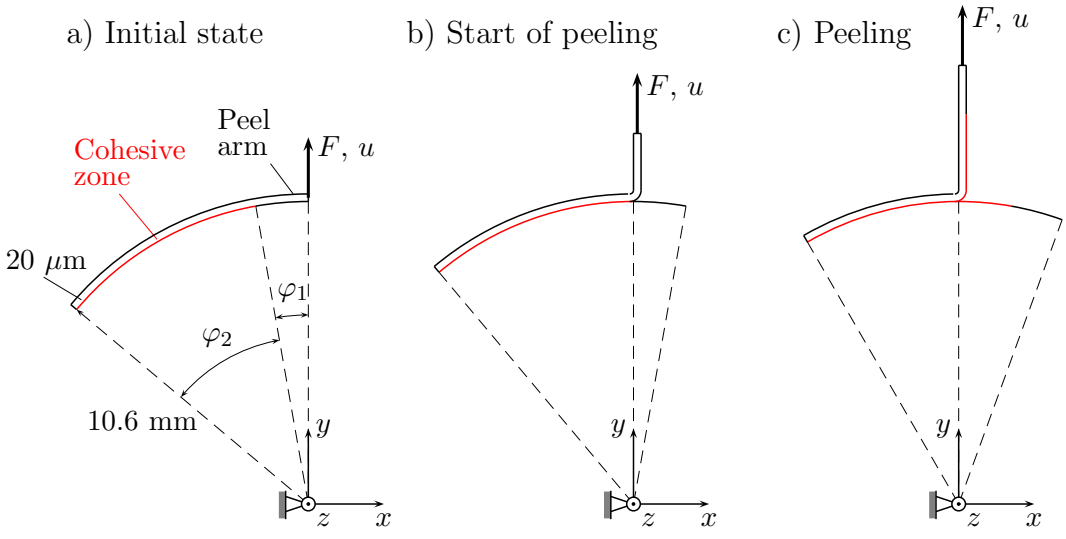

Figure 9: Schematic side view of three consecutive stages (a-c) of the 3D finite element peel test model used for the simulations in the present study (not drawn to scale).

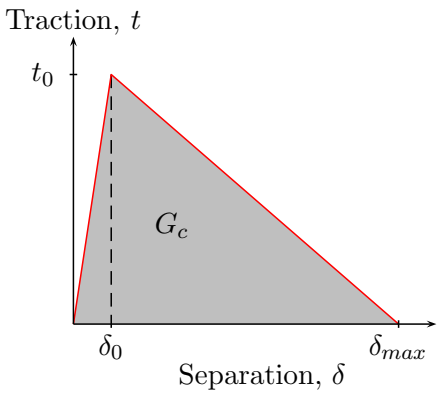

Figure 10: Bilinear traction-separation law for mode I loading.

In line with [12, 13], a Van der Waals hyperelastic model is adopted for the peel arm material. Assuming incompressibility, the strain energy potential function for this model has the format

$$\tilde{U}\left(I_2\right) = \mu \left\{ -\left(\lambda_m^2 - 3\right)\left[\ln\left(1-\eta\right)+\eta\right] - \frac{2}{3}a\left(\frac{I_2-3}{2}\right)^{3/2} \right\}, \quad \eta = \sqrt{\frac{I_2-3}{\lambda_m^2-3}} \tag{1}$$

where $I_2 = \lambda^{-2} + 2\lambda$ is the second invariant of the left Cauchy-Green tensor and λ is the stretch. Under uniaxial loading, the nominal strain ε provides the stretch $\lambda = 1 + \varepsilon$ and Eq. (1) yields the nominal stress as

$$\sigma(\lambda) = \frac{\partial \tilde{U}}{\partial \lambda} = \mu(1-\lambda^{-3})\left(\tfrac{1}{1-\eta} - a\sqrt{\tfrac{I_2-3}{2}}\right) \tag{2}$$

The constitutive model for the peel arm material is fitted, using a least-squares fitting procedure, to the average of the tensile test data shown in Fig. 3. From the calibration procedure, the locking stretch $\lambda_m = 5.28$, the interaction parameter $a = 0.53$ and the shear modulus $\mu = 16.8$ MPa were identified. The calibrated model response is shown together with the experimental data in Fig. 11.

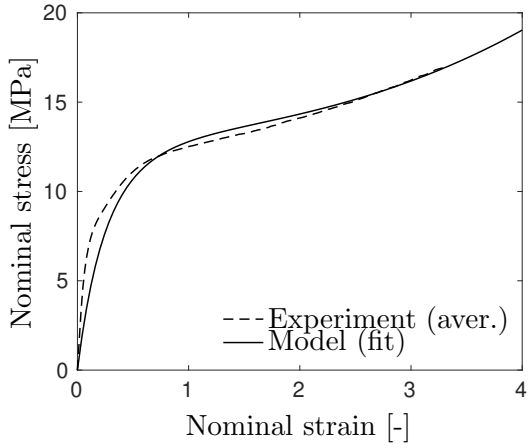

Figure 11: Uniaxial tensile response of the Van der Waals hyperelastic model (solid line), fitted to the averaged tensile test data from Fig. 3 in Section 2.1 (dashed line).

4 Evaluation of experimental data and simulations

The aim of establishing the numerical model is to evaluate the forces, deformations and energies involved during continuous peeling. Fig. 12a shows the peel force versus peel arm displacement obtained in the simulations and Fig. 12b shows the force-displacement response obtained in the peel test experiments, cf. Section 2.2.

Compared to the experiment, the model is significantly stiffer, as evident from the slope of the curve in Fig. 12a. This is mainly due to the fact that the substrate is modeled as a rigid surface. Experimentally, there is some compliance in the substrate, especially since the paperboard is weakest in the out-of-plane direction. The adhesive tape used to attach the laminate to the wheel also adds some compliance. However, the present focus lies on the continuous peeling, i.e. the force plateau, which is well captured by the model, rather than the initial stage of peel arm formation and deformation. The model calibration was achieved using a fracture energy $G_c = 210$ J/m^2 and a peak traction $t_0 = 7.5$ MPa.

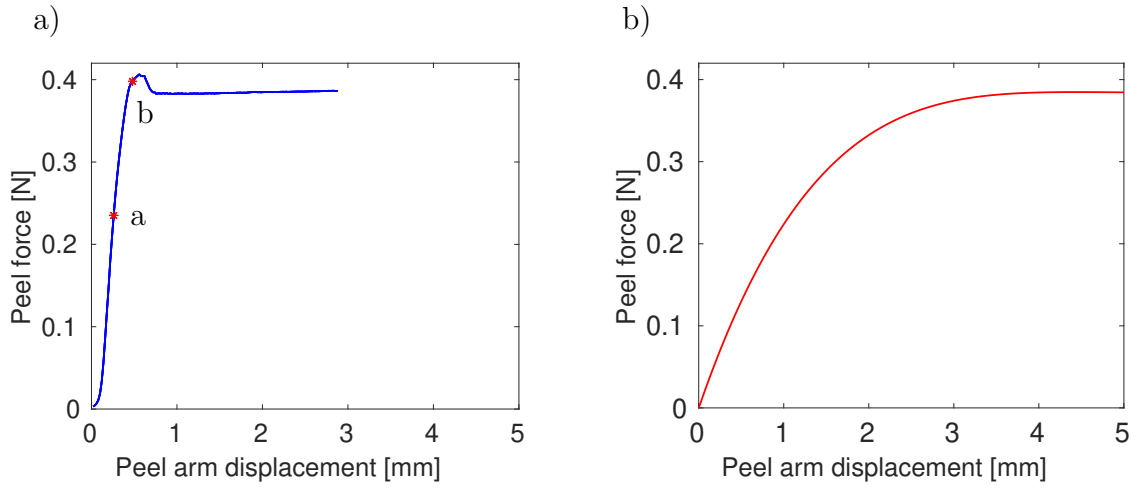

Figure 12: a) Force-displacement response of calibrated cohesive zone model. b) Force-displacement response of experiments, cf. Fig. 5b.

In Fig. 13, different energy quantities are extracted from the simulated peel test and the partition of the external work into peel arm strain energy and fracture energy can be seen. In the force-displacement data from the simulations, Fig. 12, a small bump in the force can be noticed after about 0.5 mm. A close comparison with the energies in Fig. 13 reveals that the strain energy is also lowered at around the same displacement, while the damage energy increases more steeply than before. This also seems to correspond to a number of elements simultaneously detaching from the substrate. Hence, it seems that during the first delamination, some of the stored elastic energy is dissipated in damage initiation. After that, the system reaches a steady-state with a more stable peak load, but with small fluctuations due to stick-slip behavior.

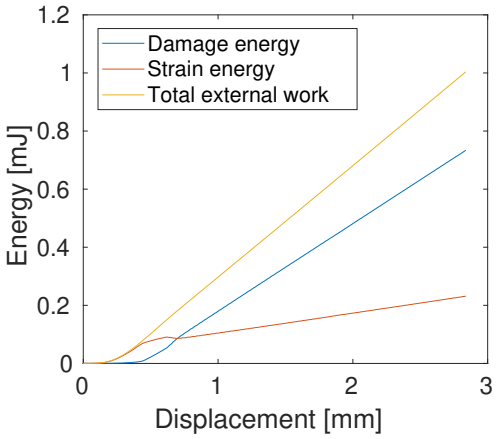

Figure 13: Energy distribution between strain energy and damage energy, as part of total supplied work in cohesive zone model.

It can be seen in Fig. 13b that, after less than 1 mm, the damage energy surpasses the strain energy. This is due to the fact that a greater number of the elements have delaminated, since the energy is summed up for the whole model, but it is also seen that the damage energy increases more quickly than the strain energy. In the early stages of loading, most of the supplied energy goes into strain energy (except small damping energies) with no damage dissipation, until damage becomes dominant.

In addition to calibration of the simulated peel force plateau level, the geometry of the peel arm is also of interest for model calibration. Fig. 14 shows an overlay of the simulated peel arm geometry, represented by red lines, onto the geometry observed by X-ray tomography. A reasonable agreement is obtained. The opening angle for the numerical model is estimated to 53°. This is more than the 35° measured experimentally, but there is a qualitative agreement between the shapes and an exact determination of the opening angle is hard to achieve, in simulation output and tomography images alike. The thickness of the peel arm is reduced from 20 μm to about 17-18 μm, indicating that the thickness reduction is somewhat underestimated compared to the experiment.

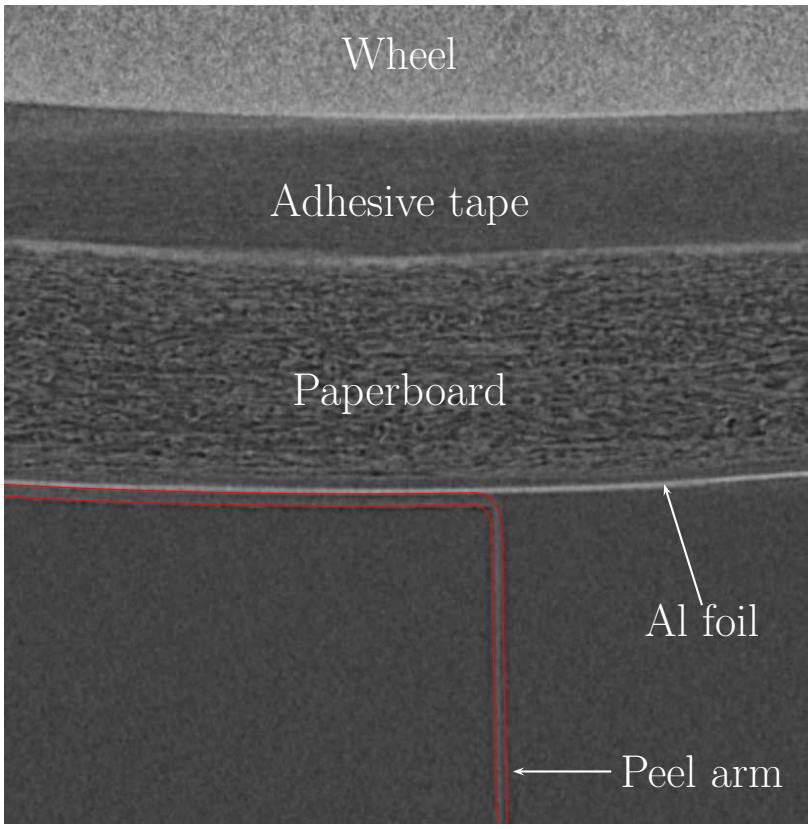

Figure 14: Side view of the peel test. The red lines represent the simulated peel arm geometry, overlaid on top of the experimental X-ray image.

A close-up of the simulated peel front is shown in Fig. 15, where the peel arm has been peeled downwards in the vertical direction. The wheel is indicated for visualization purposes. It is seen that the crack front is curved, with the edges damaged further ahead from the peel front than the center of the peel arm. This agrees with the peel front shape that can be seen in the tomography image in Fig. 6.

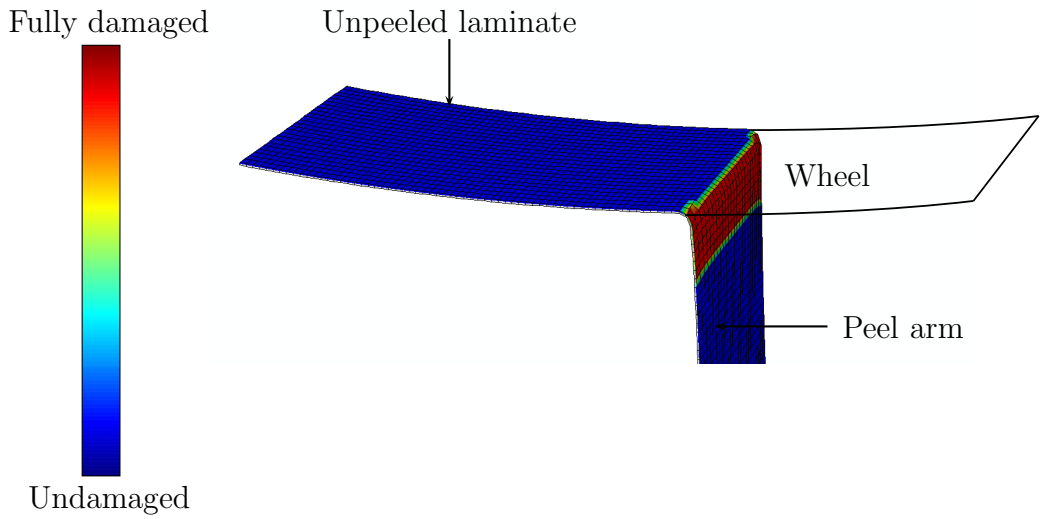

Figure 15: View of the peel front. The peel arm is pulled downwards. The colors indicate the damage in the cohesive zone, with red elements having failed and blue or green elements having a lower degree of damage.

The damage variable (Abaqus output CSDMG) and axial stress (in the peeling direction) are measured across a set of nodes spanning the width of the sample. The nodes are chosen along a line close to the initial peel front. A damage value of CSDMG = 0 means the interface is undamaged while a value of CSDMG = 1 means the adhesion is completely lost. The quantities are measured at two points in time during the simulation, indicated by red marks in Fig. 12a. The first point in time (point a in Fig. 12a) corresponds to when damage has just initiated at some of the nodes and the second time (point b in Fig. 12a) is when the system has reached a steady state and all of the nodes in the traced set have failed (CSDMG = 1).

The damage variable CSDMG and the axial stress across the width of the sample are shown in Fig. 16. It is again seen that the edges are damaged first. A somewhat surprising finding is the higher stress and corresponding damage in the center compared to the material between the center and the edges in Fig. 16a and b. This is likely due to the uneven deformation (transverse contraction) of the peel arm. When the damage is fully developed, which is shown by the damage variable being 1 across the whole width in Fig. 16c, the stress profile is parabolic with a peak in the middle. Hence, as peeling initiates, the edges are damaged first due to higher stresses in these regions. Due to being damaged first, the edges subsequently delaminate first, leading to a lower stress along the specimen edges.

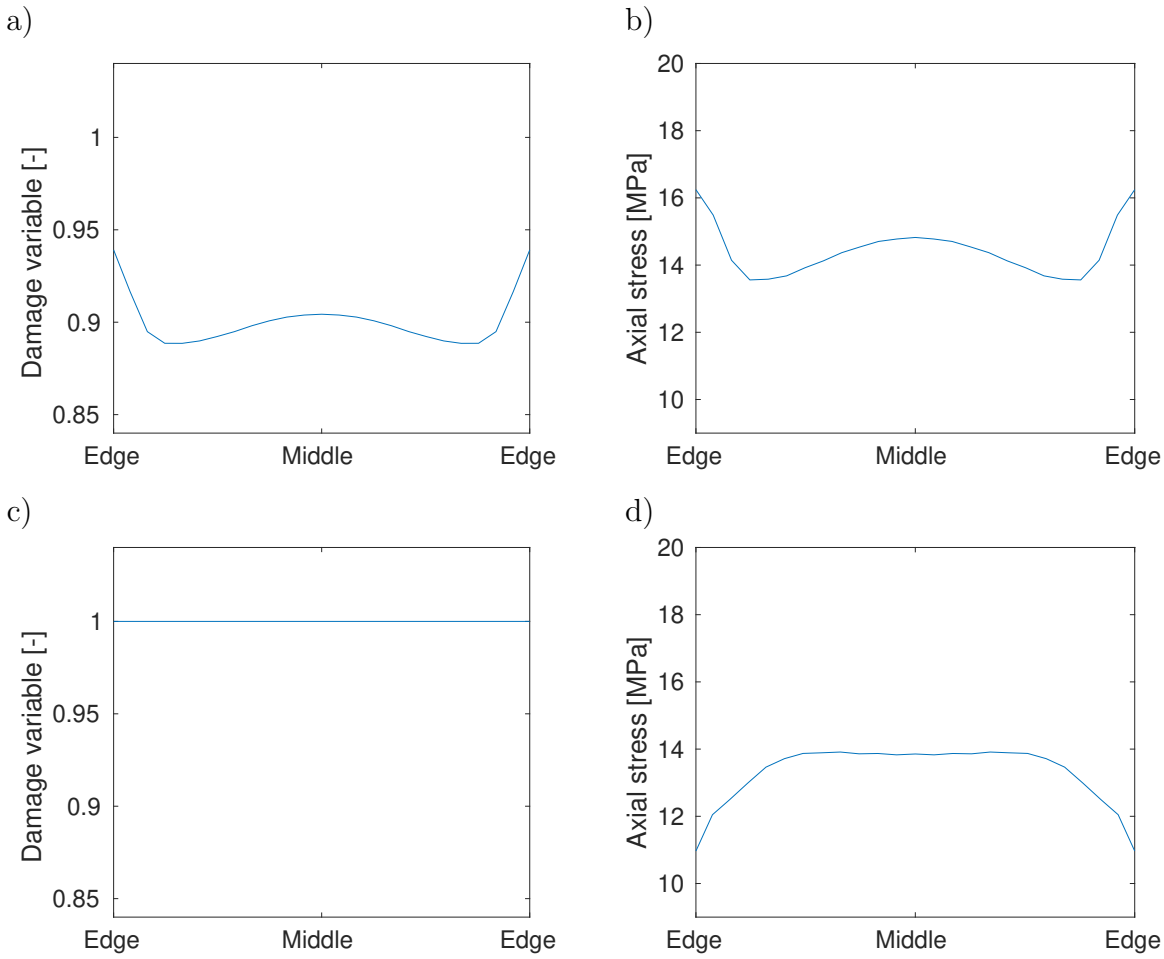

Figure 16: a) Damage variable as function of position along width when damage starts. b) Stress in the vertical direction as function of position along width, at the same state as in figure a). c) Damage when the force has reached a plateau corresponding to point b in Fig. 12a. d) Stress in the vertical direction at the same state as in figure c).

4.1 The macroscopic view on adhesive fracture energy

To complement the numerical simulations, an analytical model of the peel test process is established in this section. In a typical peel test, a strip of width b and thickness $h \ll b$ is peeled off from a rigid substrate as illustrated in Fig. 17. The length of the peel arm and the length of the adhesive fracture zone is here denoted by l and a, respectively, and the film is peeled at an angle θ from the substrate. When the peel angle θ is increased from $\theta = 0°$ to $\theta = 90°$, the fracture mode changes from pure mode II (in-plane shear) to pure mode I (tensile). Following the arguments in [9], it can be noted that a mixed mode analysis for $0 < \theta < 90°$ is usually not called for and consideration of only mode I loading usually suffices. This is also the viewpoint adopted in several studies on peeling of thin polymer films, for example in [15].

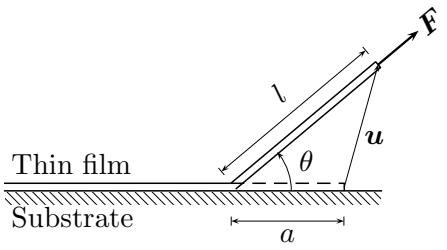

Figure 17: Schematic illustration of peeling of a thin film from a rigid substrate. The film, of width b and thickness $h \ll b$, is peeled of by a force (vector) $\boldsymbol{F}$ at an angle θ from the substrate, which is assumed to be rigid. The displacement of the end of the peel arm is denoted by the vector $\boldsymbol{u}$. The length of the adhesive fracture zone and the length of the stretched peel arm is denoted by denoted by a and l, respectively.

To identify the adhesive fracture energy release rate G_c, an energy balance can be established as

$$G_c \, b\dot{a} = \dot{W} - \dot{U} - \dot{\mathcal{D}} \tag{3}$$

where W is the external work done by the peel force $\boldsymbol{F}$ with magnitude F, U is the strain energy stored in the peel arm and $\mathcal{D} \geq 0$ is the energy dissipation. A superposed dot denotes differentiation with respect to time. The external work power can be evaluated from the vector product between the peel force and the rate of displacement, to provide

$$\dot{W} = \boldsymbol{F} \cdot \dot{\boldsymbol{u}} = F \left(\dot{l} - \dot{a} \cos\theta \right) \tag{4}$$

where l is the length of the peeled-off strip and θ the peel angle. Combining eqs. (3) and (4) yields

$$\dot{U} + G_c \, b\dot{a} = F \left(\dot{l} - \dot{a} \cos\theta \right) - \dot{\mathcal{D}} \tag{5}$$

Next, a finite strain setting is assumed and the polymer film constituting the peel arm is in the present case modeled using a constitutive model assuming an isotropic, hyperelastic and incompressible material behavior, as discussed in [5]. Under uniaxial tensile loading of the film, the stretch ratio $\lambda = l/a$ can be identified and the elastic strain energy density can, quite generally, be expressed as $\tilde{U} = \tilde{U}(I_1, I_2)$, in terms of $I_1 = \lambda^2 + 2\lambda^{-1}$ and $I_2 = 2\lambda + \lambda^{-2}$, being the first and second invariants of the left Cauchy-Green strain tensor. At this stage, the stored energy can be evaluated as

$$U = bh \int_0^a \tilde{U}(\lambda) ds \tag{6}$$

This strain energy can now be inserted into the energy balance in eq. (5) to provide

$$abh \frac{d\tilde{U}}{d\lambda} \dot{\lambda} + bh\tilde{U}\dot{a} + G_c \, b\dot{a} = F \left(\dot{l} - \dot{a} \cos\theta \right) - \dot{\mathcal{D}} \tag{7}$$

With $\lambda = l/a$, eq. (7) can be further recast into

$$bh \frac{d\tilde{U}}{d\lambda} \dot{l} - bh \frac{d\tilde{U}}{d\lambda} \lambda \dot{a} + bh\tilde{U}\dot{a} + G_c \, b\dot{a} = F \left(\dot{l} - \dot{a} \cos\theta \right) - \dot{\mathcal{D}} \tag{8}$$

Noting that the nominal uniaxial stress in the peel arm is provided by

$$\sigma(\lambda) = \frac{d\tilde{U}}{d\lambda} = \frac{F}{bh} \tag{9}$$

the energy balance in eq. (8) can be stated as

$$\left[bh\tilde{U} + F\left(\cos\theta - \lambda\right) + G_c\, b\right] \dot{a} = -\dot{\mathcal{D}} \leq 0 \tag{10}$$

For $\dot{a} \geq 0$, a positive dissipation is ensured by

$$G_c = \frac{F}{b}\left(\lambda - \cos\theta\right) - h\tilde{U}(\lambda) \tag{11}$$

The resulting adhesive fracture energy release rate obtained in eq. (11) is a general format, also applicable to dissipative materials. It can be noted that if the stretch $\lambda = 1$ throughout the peeling, then $\tilde{U} = 0$. This corresponds to the situation of a rigid peel arm material as considered in the classical Rivlin model [17], which appears as

$$G_c^{Rivlin} = \frac{F}{b}\left(1 - \cos\theta\right) \tag{12}$$

In addition, if small elastic strains $\epsilon \ll 1$ in the peel arm are assumed, then $\lambda = 1 + \epsilon$ and the strain energy density appears as

$$\tilde{U} = \frac{1}{2}\sigma\epsilon = \frac{1}{2}\frac{F^2}{E(bh)^2} \tag{13}$$

where E is the elastic Young's modulus of the peel arm material. Using eq. (13) in eq. (11) results in the often used Kendall model [7], having the format

$$G_c^{Kendall} = \frac{1}{2}\frac{F^2}{Eb^2h} + \frac{F}{b}\left(1 - \cos\theta\right) \tag{14}$$

Obviously, for an infinitely stiff peel arm, $E \to \infty$ and the first term on the right-hand side of eq. (14) vanishes and the Rivlin model in eq. (12) is again recovered.

As shown in [5], the different models of the adhesive fracture energy release rate are related as

$$G_c^{Rivlin} \leq G_c^{Kendall} \leq G_c \tag{15}$$

According to eq. (15), the Rivlin model can be expected to provide a lower-bound estimate of the adhesive energy release rate.

It can also be noted that the energy balance provided by eq. (3) corresponds to the one used by Kinloch *et al.* in [9], with the dissipation $\mathcal{D}$ containing contributions from plastic bending close to the peel front. It is, however, shown in the peel experiments on thin low-density polyethylene (LDPE) films conducted in [15], that the energy dissipated in the bending deformation is two orders of magnitude smaller than the peel energy, also for an extreme peel angle of $\theta = 180°$. A similar conclusion is arrived at in [12] where the combined plastic dissipation from bending and stretching of the peel arm is calculated to be about one order of magnitude lower than the fracture energy. The conclusion drawn

in [15] is that the energy dissipation due to bending during peeling of a thin polymer film can be neglected. The same viewpoint is adopted also in the present work and the plastic dissipation will not be distinguished as a separate component.

Using eq. (11) and rewriting the hyperelastic potential in terms of the stretch λ, the fracture energy for this model at a peel angle $\theta = 90°$ becomes

$$G_c = \frac{F\lambda}{b} + h\mu \left\{ (\lambda_m^2 - 3)(\ln(1 - \sqrt{\frac{2\lambda+\lambda^{-2}-3}{\lambda_m^2-3}}) + \sqrt{\frac{2\lambda+\lambda^{-2}-3}{\lambda_m^2-3}}) + \frac{2a(\lambda+\frac{1}{2\lambda^2}-\frac{3}{2})^{3/2}}{6} \right\} \quad (16)$$

A comparison of the different fracture energies (Rivlin, Kendall and the calibrated van der Waals model) for the range of stretches $1 \leq \lambda \leq 2$ is shown in Fig. 18. The calculations are based on the experimental average force $F = 0.385$ N and a peel arm width of 2 mm.

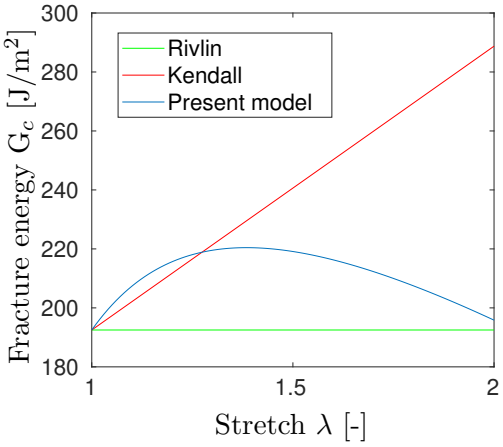

Figure 18: Fracture energy according to Rivlin (green), Kendall (red) and van der Waals (blue) model, respectively.

The maximum strain in the pulling direction just before fracture initiates is around 12.05% and when the first nodes reach total failure, around 43.68 %. Using the first value $\lambda = 1.1204$, G_c is estimated to 209.5 J/m^2 from eq. (16) (van der Waals), 204.1 J/m^2 from eq. (14) (Kendall) and 192.5 J/m^2 from eq. (12) (Rivlin). The fracture energy G_c was thus reasonably well estimated by these macroscopic models. Since the value used in the finite element model is 210 J/m^2, all of the expressions for the fracture energy give good approximations, to the right order of magnitude. The Rivlin model somewhat underestimates G_c, while the Kendall and van der Waals equations are in closer agreement. Thus it seems that the fracture energy can be predicted analytically and that the van der Waals model in eq. 16 gives the best prediction.

5 Concluding remarks

Peel testing of a packaging material laminate has been performed using a newly developed peel test load frame. The experimental setup makes it possible to perform 90° peel tests under *in-situ* loading in a laboratory X-ray tomograph. The laminate considered in the

present study consists of paperboard, an aluminum foil, an adhesive layer and a thin mPE film that constitutes the peel arm. The experimental results are analyzed and compared to analytic models as well as to 3D finite element simulations, based on a cohesive zone model of the adhesive fracture region.

Relaxation occurs during X-ray scanning, but it is still possible to obtain images of the peeled state. It is found that the delamination progresses in a thumbnail fashion, where the edges delaminate slightly earlier than the middle, a pattern which is maintained in the steady state peeling. This is confirmed experimentally by several *in-situ* peel tests and is likely due to transverse contraction, and to a minor extent due to artifacts from the sample preparation. This result is also seen when running numerical simulations with a cohesive zone model of the interface and a hyperelastic, almost incompressible, model for the peel arm material. The demonstrated experimental setup can be used for further *in-situ* studies, e.g. investigating the effect of different peeling rates, not just for macroscopic effects, but also to investigate and better understand the microscale mechanisms of peeling.

The tomography images provide new 3D insights, into the evolution of the deformation zone during peel testing. As examples, non-homogeneous adhesion behavior as well as occurrence of adhesive as well as cohesive damage is indicated. This motivates further detailed studies to link macroscopically measured adhesion data to actual microscale damage mechanisms. The experimental, numerical and analytical tools proposed in this study provide the tools to pursue such studies. The experiments can also be used for calibration of a numerical model, with both the force and geometry acting as benchmarks. Thus the experiments can aid modeling efforts with more data than traditional macroscopic peel tests.

The analytical models can give a first estimate of the fracture energy to be used for the numerical model. In this work, the strain just before fracture was estimated from results obtained with the numerical model, but a future study could use experiments to estimate this strain. An interesting approach to estimate the strain in the peel arm experimentally is to use Digital Volume Correlation (DVC) for the peel arm material. The fracture energy can then be estimated with the analytical models based on the measured strain at the peel front just before fracture. The strain field obtained from DVC could potentially also be used as a calibration target. An investigation into the possibility of using DVC for the peel arm material is part of ongoing work.

6 Acknowledgment

Project funding from Tetra Pak Packaging Solutions AB is gratefully acknowledged by the authors.

References

[1] P.I. Anderson, W. Grellmann, and S. Seidler. *Polymer testing*. Carl Hanser Verlag GmbH Co KG, 2013.

[2] Tirthankar Bhattacharjee, Manish Barlingay, Hummad Tasneem, Esra Roan, and Kumar Vemaganti. Cohesive zone modeling of mode i tearing in thin soft materials. *Journal of the mechanical behavior of biomedical materials*, 28:37–46, 2013.

[3] R.D.S.G. Campilho, M.D. Banea, J.A.B.P. Neto, and L.F.M. da Silva. Modelling adhesive joints with cohesive zone models: effect of the cohesive law shape of the adhesive layer. *Int. J. Adhes. Adhes.*, 44:48–56, 2013.

[4] Marie-Julie Dalbe, Pierre-Philippe Cortet, Matteo Ciccotti, Loïc Vanel, and Stéphane Santucci. Multiscale stick-slip dynamics of adhesive tape peeling. *Physical review letters*, 115(12):128301, 2015.

[5] V.A. Eremeyev and K. Naumenko. A relationship between effective work of adhesion and peel force for thin hyperelastic films undergoing large deformation. *J. Mech. Phys. Solids*, 69:24–26, 2015.

[6] L.F. Kawashita, A.J. Kinloch, D.R. Moore, and J.G. Williams. A critical investigation of the use of a mandrel peel method for the determination of adhesive fracture toughness of metal-polymer laminates. *Eng. Fract. Mech.*, 73(16):2304–2323, 2006.

[7] K. Kendall. Thin-film peeling - the elastic term. *J. Phys. D: Appl. Phys.*, 8:1449–1452, 1975.

[8] A.J. Kinloch. *Adhesion and adhesives: science and technology*. Springer Science & Business Media, 2012.

[9] A.J. Kinloch, C.C. Lau, and J.G. Williams. The peeling of flexible laminates. *International Journal of Fracture*, 66:45–70, 1994.

[10] S. Marzi, A. Biel, and O. Hesebeck. 3D optical displacement measurements on dynamically loaded adhesively bonded T-peel specimens. *Int. J. Adhes. Adhes.*, 56:41–45, 2015.

[11] Z. Miyagi, M. Koike, Y. Urahama, and K. Yamamoto. Study of peeling properties of pressure-sensitive adhesives using a newly developed image processing system. *Int. J. Adhes. Adhes.*, 14(1):39–45, 1994.

[12] I.K. Mohammed, M.N. Charalambides, and A.J. Kinloch. Modelling the interfacial peeling of pressure-sensitive adhesives. *Journal of Non-Newtonian Fluid Mechanics*, 222:141–150, 2015.

[13] I.K. Mohammed, A.J. Kinloch, and M.N. Charalambides. Modelling the peeling behavior of soft adhesives. In *Procedia Structural Integrity*, volume 2, pages 326–333. Proceedings of the 21st European Conference on Fracture, ECF21, Catania, Italy, June 2016.

[14] Bikramjit Mukherjee, David A Dillard, Robert B Moore, and Romesh C Batra. Debonding of confined elastomeric layer using cohesive zone model. *International Journal of Adhesion and Adhesives*, 66:114–127, 2016.

[15] M. Nase, B. Langer, and W. Grellmann. Fracture mechanics on polyethylene/polybutene-1 peel films. *Polymer Testing*, 27:1017–1025, 2008.

[16] M. Nase, M. Rennert, K. Naumenko, and V.A. Eremeyev. Identifying traction-separation behavior of self-adhesive polymeric films from in situ digital images under T-peeling. *J. Mech. Phys. Solids*, 91:40–55, 2016.

[17] R.S. Rivlin. The effective work of adhesion. *Paint Technol.*, 9:215–216, 1944.

[18] Sigurdur T Thoroddsen, HD Nguyen, K Takehara, and TG Etoh. Stick-slip substructure in rapid tape peeling. *Physical Review E*, 82(4):046107, 2010.

[19] M.D. Thouless and Q.D. Yang. A parametric study of the peel test. *Int. J. Adhes. Adhes.*, 28:176–184, 2008.

[20] SM Xia, Laurent Ponson, Guruswami Ravichandran, and Kaushik Bhattacharya. Adhesion of heterogeneous thin films ii: Adhesive heterogeneity. *Journal of the Mechanics and Physics of Solids*, 83:88–103, 2015.